Compressive Mechanical Properties and Collagen Fiber Orientation and Dispersion in the Cervix of Non-Pregnant and Pregnant Women

Wang Yao

Submitted in partial fulfillment of the
requirements for the degree
of Doctor of Philosophy
in the Graduate School of Arts and Sciences

COLUMBIA UNIVERSITY

2017

ABSTRACT

Compressive Mechanical Properties and Collagen Fiber Orientation and Dispersion in the Cervix of Non-Pregnant and Pregnant Women

Wang Yao

The cervix serves as the passage for the fetus during birth. The mechanical function of the cervix is crucial for a healthy term pregnancy: 1) prior to term it must remain closed and resist the increasing mechanical load from the growing pregnancy and 2) at time of parturition it must soften, deform and dilate to allow for delivery of the fetus. After delivery, the cervix must repair and close. The timing and characteristics of this remodeling behavior is currently an active research focus because it is hypothesized that premature remodeling in pregnancy can lead to preterm birth, a leading cause of neonatal death or significant neonatal morbidity. The research goal was to measure and characterize anisotropic material properties because they contribute to keeping cervix shut.

In this thesis, the collagen fiber network orientation and dispersion of non-pregnant and pregnant human cervical tissue samples were analyzed using optical coherence tomography, and the samples were tested using mechanical indentation and digital image correlation techniques. Human cervices were acquired from non-pregnant and pregnant consented patients that went through hysterectomy. Axial cervical slices were imaged using optical coherence tomography and fiber orientation and dispersion data was analyzed using a new pixel-wise fiber orientation algorithm and was compared among four anatomical quadrants and among patients with different obstetric backgrounds. Two radial zones with different fiber orientations were found. The posterior and anterior quadrants of the outer zone were found to have distinct fiber dispersion features and their fiber dispersion shifted most dramatically from non-pregnant to pregnant. In an effort to characterize the compressive mechanical behavior of human cervical tissue, we present a novel indentation test with digital correlation imaging to visualize the real-time deformation of cervical slice during indentation and measure the compressive mechanical properties through coupled finite element analysis with collagen

fiber orientation and dispersion information informed by OCT of non-pregnant and term pregnant cervical tissue. Heterogeneity within the same cervix and difference between non-pregnant and pregnant cervices were found. The upper cervix was found to have a stronger ground substance. The anterior and posterior quadrants were less compressible than the left and right quadrants for non-pregnant specimens. The upper cervix of non-pregnant patients had a stronger ground substance than that of pregnant patients.

A workflow of optical, mechanical, and chemical experiments on the same piece of specimen with most fibers intact was also proposed in this thesis and these experiments would validate and inform each other.

Table of Contents

List of Figures

List of Tables

Acknowledgements

First, I would like to thank my advisor, Dr. Kristin Myers. I was so fortunate to be her student and get her guidance to research and life. She cares about her students and I always enjoyed working with her.

I also want to thank other members in my committee, Drs. Gerard Ateshian, Jeffrey Kysar, Christine Hendon, and Karen Kasza. Dr. Ateshian provided many helpful insights for me when I encountered obstacles.

I would like to thank my collaborators. Dr. Yu Gan from Dr. Hendon's lab who had been working with me closely and provided great contributions to my research. We are also good friends outside research. Ryan Harris and Jia Hao from Dr. Eve Donnelly's lab also provided helpful insights to my research.

I had a great time throughout the years with my lab mates Dr. Michael Fernandez, Dr. Kyoko Yoshida, Andrea Westervelt, Eugene McKee, Lily Zhao, Lei Shi, Dr. Charles Jayyosi, and Nicole Lee. Lei, Eugene, and Lily had helped me brainstorming ways to deal with obstacles in data processing and I really appreciate their help.

Special thanks to my parents, grandparents, and my girlfriend Ye Miao. They have been supportive to me along my journey and my accomplishments would not have been possible without them.

1 Introduction

1.1 Anatomy of the human uterine cervix

The cervix is the cylindrical caudal part of the uterus. It protrudes and opens through the upper anterior vaginal wall into the vagina. The caudal part of the cervix that protrudes into the vagina is called the portio vaginalis, which is about 3 cm long and 2.5 cm in diameter[1]. The opening into the vagina is the external os. The cephalic part of the cervix, or the portio supravaginalis, lies above the vagina's attachment to the cervix. Cardinal ligaments attach this portion laterally. Bladder lies in the anterior direction and is separated from this portion by loose connective tissue. The internal os is the opening at the cephalic end of the cervix, which is connected with the uterine body. The internal os is connected to the external os by a passage in the center of the cylinder called the endocervical canal.

1.2 Cervical remodeling in pregnancy

The cervix serves as the passage for the fetus during birth. Prior to term, the cervix must remain closed and resist the increasing mechanical load from the growing pregnancy. The inner canal is collapsed, fusiform, and firm, with the consistency of nasal cartilage. During pregnancy, the cervix gradually elongates. For multiparous women, the diameter of the inner canal at the external os is often 1-2 cm. At time of parturition the cervix must be soft to deform and dilate to 10 cm in diameter to allow for delivery of the fetus.

After delivery, the cervix must return to a state close enough to the original state. During pregnancy and delivery, the cervix goes through four overlapped phases: softening, ripening, dilation, and postpartum repair [2]. Initial evidence supports that softening starts in the first trimester for human pregnancy and it is a slow process taken place in a progesterone-rich environment for the cervix to gradually lose strength [2]. Significant difference in strength was found between NP and first trimester, as well as between first and second trimester [3]. Following softening is the ripening phase, in which cervix goes through a much more dramatic changes in a shorter period of time. It happens days or weeks before delivery for human. It features maximal loss of tissue compliance and integrity [2].

Ripening was followed by dilation such that a term fetus can pass the ripened cervix. A study [4] found for human cervical tissue, the mechanical strength can be one to four magnitude weaker for cervix at dilation phase than NP. In the postpartum repair phase, the cervix recovers its integrity and mechanical strength. The strength of the postpartum cervix is significantly stronger than it of third trimester although it is weaker than a NP state [3].

The cervical remodeling process has significant clinical importance. An obstetrician use vaginal examination to determine the state of the cervix thus the suitability of elective induction. The well-known standard is called Bishop score, a pre-labor scoring system for elective induction evaluation and spontaneous preterm labor odds assessment. The Bishop score system take five factors (dilatation, effacement, consistency, and position of the cervix, and the station of the presenting part) into account and each factor is assigned a score of 0 to 2 or 0 to 3. The sum of five scores over 9 indicates that elective induction may be successful [5]. In addition, a higher-than-normal Bishop score at certain gestation date forewarn the possibility of premature labor while a lower-than-normal score indicates postmaturity or wrong delivery date calculation [5]. In another quantitative study [6], Bishop score was found to be significantly associated with spontaneous preterm delivery in a logistic regression analysis.

1.3 Clinical motivation: cervical pathologies in pregnancy

1.3.1 Spontaneous Preterm Birth (sPTB)

The WHO defines preterm birth as any birth before 37 completed weeks of gestation, which is further subdivided by gestational age: extremely preterm (<28 weeks), very preterm (28–32 weeks), and moderate or late preterm (32–37 completed weeks of gestation. The more premature a birth is, the higher mortality, disability, and costs are associated [7].

Preterm birth is can be broadly classified into two groups: (1) spontaneous preterm birth (sPTB) and (2) provider-initiated preterm birth. A strong risk factor for sPTB is individual or family history of sPTB, while other risk factors are maternal age, short inter-pregnancy intervals, low maternal

body-mass index (BMI), multiple pregnancy, pre-existing non-communicable disease, hypertensive disease of pregnancy, and infections [7].

The global average PTB rate is 11.1%, affecting around 15 million newborns every year worldwide. PTB rate varies by country and it can be as low as 5% and as high as 18%. Higher-income countries generally have lower PTB rates but some high-income countries including USA (12.0%) have relatively high PTB rates. PTB rates in most countries have been increasing since 1990 [7].

PTB is the leading cause for deaths in newborns, responsible for around 1 million neonatal deaths every year. PTB is also the second-leading cause of death in children under 5 years. For babies who survive, they face a much higher chance of lifetime disabilities including neurodevelopmental functioning and chronic disease in adulthood [8]. However, the cause of PTB is unidentified for many cases [9]. This urges the research of PTB and a better understanding of the mechanical role of the cervix during pregnancy.

1.4 Extracellular Matrix

It has been suggested that CI results from alterations in cervical tissue extracellular matrix (ECM; [10]). During pregnancy, the content and ultrastructure of cervical ECM shift drastically to facilitate cervix to soften and dilate. Cellular component is typically around 20% per volume and two dominant types of cells are fibroblasts and smooth muscle cells. Cervical ECM, consisted of cross-linked, fiber-forming collagens that are embedded in a viscous ground substance of negatively charged proteoglycans (PGs) and glycosaminoglycans (GAGs), supports these cervical cells and provides strength and rigiditiy to resist mechanical loading. See Table 1.1 for the percentage of each constituent [11].

The premature change in mechanical properties of the cervix induced by alterations of cervical tissue ECM content and ultrastructure is thought to contribute to cervical failure leading to preterm birth. Cervical collagen exists as fibers in a hierarchical network embedded in a viscous ground substance of negatively charged glycosaminoglycans (GAGs) and other proteins [12].

<table>
<tr><td>Water</td><td colspan="6">80%</td></tr>
<tr><td rowspan="3">Dry Tissue</td><td colspan="6">20%</td></tr>
<tr><td colspan="2">Collagen ~70%</td><td colspan="3">GAGs ~0.2%</td><td rowspan="2">Elastin ~2%</td></tr>
<tr><td>Type I ~70%</td><td>Type III ~30%</td><td>Dermatan sulfate 76%</td><td>Heparan sulfate 13%</td><td>Hyaluronic acid 11%</td></tr>
</table>

Table 1.1. Main constituents of human cervical tissue in non-pregnant women [11]

1.5 Previous collagen fiber studies of the cervix

The collagen (types I and III) makes up 34 to 77% of the dry weight [13, 14], with evidence from human tissue studies showing that this dry weight content remains constant during gestation[15]. Collagen exists in 20 different forms and it is the most common protein in humans but the forms and content are tissue and function specific. In cervix, type I and type III fibrils take 70% and 30% per mass for all collagen content. Collagen molecules aggregate into collagen fibrils which further aggregate into collagen fibers. The cervical collagen fiber ultrastructure has been studied using X-ray diffraction [16, 17], magnetic resonance diffusion tensor imaging (MR DTI) [18], second harmonic generation imaging (SHG) [19, 20] and optical coherence tomography [21, 22]. In general, the collagen fiber network is reported to be anisotropic with different preferred orientations in distinct anatomical regions within the cervix. X-ray diffraction studies [17] found three radial zones of preferentially aligned collagen fibers, where collagen fibers along the outer edge and next to the inner canal predominately run parallel to the canal and collagen fibers in the mid-stromal area run circumferentially around the canal. The dispersion of these fibers was found to be aligned in a narrow range of 50 to 70 degrees within each zone. MR DTI [18] confirmed the inner and middle zones but the outer zone was not resolved. More recent preliminary SHG data from Feltovich *et al*. [23] and OCT studies from our group [22] reveal a large band of circumferential fibers extending to the outer edge of the tissue. To date, it is unclear how this ultrastructure evolves with pregnancy. Studies by Danforth [24-26] reported that fiber network broke down and became disorganized during its maturation.

Whether collagen content decreases during cervical softening at term is highly controversial. However, it is suggested by most studies that cervical softening is directly caused by the remodeling and degradation of the collagen network. When cervix softens, it is actually the collagen fibers become no longer tight and organized as before and the length, alignment, and organization of collagen fibers have all altered.

The ground substance is composed of interstitial fluid, proteoglycans (PGs), and glycosaminoglycans (GAGs). PGs and GAGs generate high osmotic pressure to maintain tissue hydration and allow the tissue to resist compressive forces [11]. They also regulate collagen fibril formation and spacing. This suggests that collagen fiber network and the ground substance should be modeled separately.

1.6 Previous Mechanical Tests Summary

Mechanically characterizing the human cervix in real-time during gestation is challenging. People have used various mechanical tools, including ex-vivo tools (compression [27, 28] [29], tension [27], indentation [29], permeability [30], etc.) and in-vivo tools (aspiration [3] [31], endoflip [32, 33], etc.), to study the human cervix. The mechanical response to loading was found to be nonlinear, anisotropic, and time-dependent. Pregnant tissue was found to be orders of magnitude softer than non-pregnant tissue.

1.7 Optical Coherence Tomography

OCT is an optical imaging technique that can perform noninvasive cross-sectional imaging of internal structures of biological tissues [34]. It was first demonstrated for cross-sectional imaging in 1991. Since then, it has become a clinically useful diagnostic technique. It is undergoing rapid improvement and well positioned for wide adoption in various clinical and research applications now [35]. Two kinds of light, both low-coherence light and ultrashort laser pulses, can be used to measure internal structure in biological systems. OCT has been used for measuring retina, eye, skin, turbid [34], cardiac tissue, malignancies, musculoskeletal tissues, dental structures [35].

The microstructure of biological tissue is scanned by an optical signal transmitted through or reflected from the tissue. The signal contains time-of-flight information, which yields the spatial information about tissue microstructure [34]. Axial scan or A-scan is a single axial measurement of echo time delay of backscattered light. Multiple A-scan can generate a cross-sectional image, which represents the optical backscattering in a cross-sectional plane through the tissue and this image is called a B-scan. Cross-sectional image can be displayed in false color or grey scale to visualize tissue pathology. By acquiring sequential B-scans, volumetric data sets and be generated. The three-dimensional OCT data contain comprehensive volumetric structural information.

The optical sectioning capability of OCT and confocal microscopic systems are comparable but, unlike confocal microscopy, OCT's longitudinal resolution does not depend on available numerical aperture. This is why OCT can maintain high depth resolution even when the aperture is small. This feature facilitates measurement for deep tissues like measuring posterior eye and endoscopic imaging. The resolutions of OCT are in the range of 1-15μm which is one to two orders of magnitude finer than conventional ultrasound [36]. Microscopy and confocal microscopy are imaging techniques that have extremely high resolutions, approaching 1μm. However, although having coarser resolution, OCT has the advantage of imaging higher depth in biological tissue because its image signal and contrast degrade less significantly by optical scattering. While microscopy and confocal microscopy can perform imaging to the depth of only a few hundred micrometers, OCT's imaging depth is 2-3mm. Depth could notbe higher because light is highly scattered by most tissues. However, OCT can integrate with other instruments such as endoscopes, catheters, laparoscopes, or needles to enable internal body imaging. On the other hand, since OCT uses light which travels at approximately 3x108m/s comparing with that of sound at ~1,500m/s, the detection of echo time delays requires much higher time resolution. An OCT imaging equipment with 10μm resolution requires a time resolution of ~30fs ($30x10^{-15}$s), which makes direct electronic detection impossible so high-speed optical gating, optical correlation, or interferometry, must be used [36]. See Figure 1.1 for Comparison of resolution and imaging depth for ultrasound, OCT and confocal microscopy.

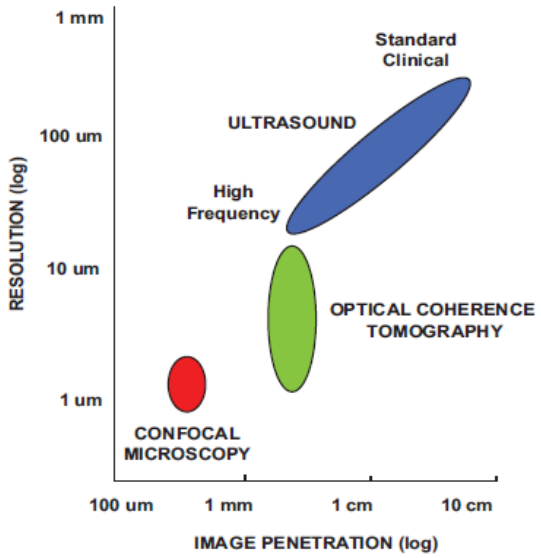

Figure 1.1. Comparison of resolution and imaging depth for ultrasound, OCT and confocal microscopy [36]

1.8 Conclusion: a need for a fiber-incorporated material model to characterize cervical mechanical properties and their deviations

Our research group is building full finite element models of pelvic region during pregnancy to study the deformation and strain distribution with simulated physiologic loading conditions. We hope to illuminate how changes in cervical material properties contribute to clinical cervical shortening. We want to understand the compressive material behavior with the collagen fiber network intact.

In Chapter 2, we reported preliminary mechanical indentation test findings of human cervical tissue. Viscoelasticity responses were studied. In Chapter 3, we use OCT and statistical tools to examine the collagen fiber network and found regions with distinct fiber orientation and dispersion characteristics. In Chapter 4, we use more complicated mechanical indentation experiments with digital image correlation to verify the finding from Chapter 3 and to solve for material parameters using optimization. In Chapter 5, preliminary tensile test results were discussed.

2 Initial Indentation Test and Analysis of Viscoelasticity

2.1 Introduction

During pregnancy, the cervix is a mechanical barrier which must remain firm and closed while the fetus develops. At term the cervix must drastically remodel, soften and dilate to allow the baby to pass. In a normal term pregnancy, this dilation is facilitated by progressive tissue remodeling where a shift in cervical extracellular matrix (ECM) content and ultrastructure cause material property changes. Cervical ECM consists of cross-linked, fiber-forming collagens that are embedded in a viscous ground substance of negatively charged proteoglycans and glycosaminoglycans [14, 15, 37-40]. These ECM components provide both compressive and tensile mechanical stiffness to the tissue and they contribute to the time-dependent nature of the cervical material response to loading. This time-dependent behavior was evident in previous uniaxial confined and unconfined compression tests of 8mm cylindrical biopsy and 5mm cube tissue samples [11, 27]. In these earlier tests, cervical tissue displayed a force- and stress-relaxation response to a ramp-hold in compressive deformation. This relaxation response was attributed to the time-dependent deformation mechanisms of the ECM, including the fluid-independent (i.e viscoelastic) unraveling of the collagen crosslink network and the fluid-dependent (i.e. poroelastic) draining of pressurized interstitial fluid [11, 41].

Cervical insufficiency (CI) is a significant obstetric dilemma which is characterized by painless shortening and dilation of the cervix leading to repeated second trimester losses or preterm birth. It is hypothesized that an insufficient cervix remodels prematurely or is too compliant at baseline to withstand the external loading conditions present during pregnancy [10, 42]. Although the true pathophysiology of CI remains unclear, it has been suggested that CI results from alterations in cervical tissue ECM, particularly the cross-linked, fiber-forming collagens and glycosaminoglycans content which leads to alterations in the mechanical properties of the tissue. To date, diagnostic tools to quantify cervical mechanical properties during pregnancy and accurately identify which patients have insufficient cervix remain under development [3, 19].

To aid in the development of an indentation-type of in-vivo tool, this study uses an established

analytical solution [43, 44] and develops an inverse finite element analysis (IFEA) to interpret the time-dependent material response of ex-vivo cervical tissue to spherical indentation. The main objectives here are 1) to use an indentation method to measure the compressive time-dependent material characteristics of intact cervical tissue slices of various thicknesses from nonpregnant (NP) and pregnant (PG) human cervical tissue samples obtained at the time of hysterectomy and 2) to validate these measurements with previously published material properties measured from uni-axial compression tests [11, 27].

In this study, cervical tissue is interpreted within a small deformation, linear viscoelastic framework because of the length scale of the deformation caused by indentation and based on previous results from a direct permeability test [30]. Spherical indentation is motivated by the potential of implementing indentation as an in-vivo mechanical testing tool to clinically monitor cervical remodeling and softening during pregnancy. The benefits of indentation methodology versus uniaxial tests are the relative ease of specimen preparation and the ability to scan various regions of the cervix to map heterogeneous properties. However, interpreting the stress-strain relationship of the tissue from indentation force-displacement data is not as straightforward as traditional uniaxial tests because of the nonuniform stress field induced by the indenter tip. Therefore, this study details an IFEA, coupled with an analytical solution [43, 44], to quantify the viscoelastic material parameters from indentation force-displacement data and to assess the compressive behavior of cervical tissues from women with various obstetric backgrounds.

2.2 Materials and Methods

2.2.1 Tissue Collection

Whole cervix specimens were acquired from consented hysterectomy patients immediately after surgical removal using an Institutional Review Board (IRB) approved protocol at the Columbia University Medical Center (obstetric histories reported in Table 2.1). For pregnant patients, indication for hysterectomy was suspected abnormal placentation (accreta/increta/percreta) and cesarean hysterectomies were performed prior to the onset of labor. A total of 18 cervical slices from 8 NP

patients and 9 cervical slices from 4 PG patients were tested. To obtain these slices the cervix was cut from the uterus and then sectioned perpendicular to the inner canal into axial slices using a custom-built cervical slicer (details of slicer device are given in [11]). Due to limited availability of hysterectomy tissue, tissue slices were cut such that multiple histological and biochemical tests can be conducted (data presented elsewhere). For this study, the majority of axial slice were between 2.2 and 5.0mm in thickness and 4 slices were thicker than 5.0mm.} Each slice was labeled according to position from the internal os, where Slice 1 was closest to the internal os. Slices were stored flat at -80 C until testing.

Patient	Age	G	TPAL parity	Obstetric history	Surgical indication	Weeks gestation	n_{sl}	Ref. ID*
NP1	41	4	2022	2 FT CS, 1 VTOP, 1 SAB	UF	-	2	NP2
NP2	44	2	2002	1 FT VD, 2 FT CS	UF	-	3	NP4
NP3	40	2	2002	2 FT VD	Prolapse	-	4	-
NP4	46	2	1011	1 FT**	UF	-	4	NP5
NP5	36	0	0000	No prior pregnancies	E	-	2	NP1
NP6	43	5	3113	3 FT VD	UF	-	1	-
NP7	40	2	0020	1 VTOP, 1 SAB	UF	-	1	-
NP8	49	1	0101	SPTD	UF	-	1	-
PG1	24	6	4014	4 FT CS, 1 SAB	SA	23	1	PG1
PG2	38	3	2002	2 FT CS	SA	35 4/7	1	PG5
PG3	35	3	2002	1 FT VD, 1 FT CS	accrete	36	4	-
PG4	30	1	1011	1 FT CS, 1 VTOP	accrete	34 4/7	3	PG2

* Corresponding patient ID in Fernandez (2013)

** Patient NP4's records were ambiguous. There was one full term birth (not known if vaginal or cesarean) and one abortion (not known if voluntary or spontaneous).

Table 2.1. Specimen information. G stands for gravida, equivalent to the total number of pregnancies. TPAL stands for term, preterm, aborted, and living deliveries, corresponding respectively to each of the 4 digits. CS = cesarean section, VTOP = voluntary termination, SAB = spontaneous abortion (miscarriage), VD = vaginal delivery, FT = full term, SPTD = spontaneous preterm delivery <37 weeks gestation. UF = uterine fibroids, E = endometriosis, SA = suspected accreta, n_{sl} = slices tested.

2.2.2 Indentation

Twelve hours before planned mechanical tests, each slice was microtomed and equilibrated in phosphate buffered saline (PBS) at 4C. After equilibration, each slice was then weighed and dimensioned. Before indentation tests, testing locations were marked at evenly spaced spots in the mid-stromal region using a small amount of waterproof ink (Figure 2.1A). Mid-stromal region was defined as the region apart from the fascia at the outer area and the mucosa around the inner canal, and spots were spaced at least 5mm apart. Cervical slices were glued to the bottom of a PBS bath (Figure 2.1B) and placed on the rigid surface of a universal testing machine (Instron Inc., Norwood, MA, Microtester 5948) equipped with a 6mm diameter stainless steel sphere indenter attached to the 5N load cell (Instron Inc., Norwood, MA, 0.25% accuracy of indicated load). The error of the fluid bath is measured by indenting into the fluid in the absence of a specimen. The average buoyant force was 0.43mN which is negligible for NP samples and approximately 10% of the equilibrium force for PG samples.

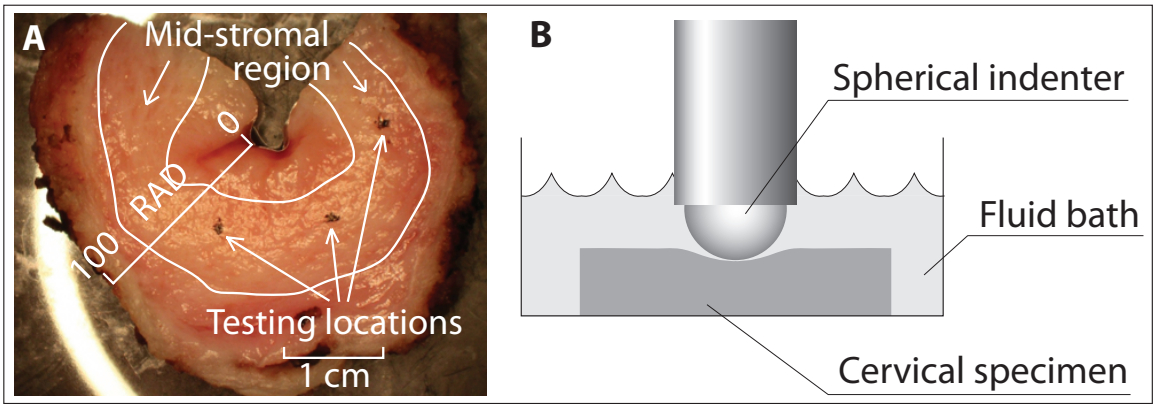

Figure 2.1. (A) An axial cervix slice. The white lines indicate the mid-stromal region, and the black dots are testing locations. Considering some indentation locations were not exactly at the mid-radius, we define radial testing position with the variable RAD. This variable is accounted for in the regression model presented in Section 3.2.4. (B) Schematic layout of indentation test.

Before each indentation test, the zero point for indentation contact was estimated by positioning the indenter tip just above the specimen surface and moving the tip down in 8um increments until a change in load greater than 0.15mN for NP and 0.05mN for PG was observed. The indenter was then raised until it was out of contact with the specimen, and the force was zeroed. After this contact estimation procedure, the sample was allowed to recover for 1 minute.

Once the sample was allowed to recover, and with the indenter tip staring above the sample, a displacement-controlled, ramp-hold indentation test was conducted, with a ramp time of t_{ramp} = 10s, a hold time of t_{hold} = 180s, and an indentation depth of h_{max} = 0.5mm. For each location, one to three ramp-hold indents were conducted at least 30 minutes apart, and load-time [N-s] data were recorded using the material tester software (Blue Hill version 3.11.1209). After indentation testing, the cervical tissue was saved for further mechanical [30] and biochemical analysis.

2.2.3 Inverse Finite Element Analysis

The tissue was modeled as an incompressible viscoelastic material (Poisson's ratio was kept at υ=0.49), using a two-time constant Prony series (Eq. 2.1) with material parameters [E, g_1, g_2, τ_1, τ_2] where $G_\infty=E/3$ is the equilibrium shear modulus (as $t\rightarrow\infty$) and $G_o=E/3(1+g_1+g_2)$ is the instantaneous shear modulus (as t=0). To determine the viscoelastic material parameters for each indentation site, an inverse finite element analysis (IFEA) was conducted for each indentation test and material parameters were averaged for tests repeated at the same site. The IFEA was conducted within the FEBio v1.5.2 framework (http://www.febio.org) by optimizing material parameters such that FE model results matched the force-displacement data. Initial material parameter guesses were obtained from a previously published analytical solution fit [43, 44]. For this analytical solution, the correspondence principle of linear viscoelasticity was employed using the isotropic elastic Hertzian contact solution for spherical indentation. Assuming incompressibility and using the Boltzmann hereditary integral, the force-time behavior was calculated using Eq. 2.2, where P(t) is load, R is tip radius and h is tip displacement}. This solution was fit to the experimental data using the nonlinear least squares optimization routine in Matlab (R2011b). The resulting material parameters were then implemented in the IFEA as initial guesses.

$$G(t) = \frac{E}{3}(1 + g_1 \exp(\frac{-t}{\tau_1}) + g_2 \exp(\frac{-t}{\tau_1})) \quad (2.1)$$

$$P(t) = \frac{8R^{1/2}}{3}\int_0^t G(t-u)\frac{dh^{3/2}(u)}{du}du \quad (2.2)$$

For the FE model, each tissue slice was represented as a quarter-section with the corresponding specimen thickness, and the indenter was represented as one eighth of the 6mm spherical indenter (Figure 2.2). The tissue slice was meshed using a mix of hexahedron and wedge elements with sizes that were biased such that the area in contact with the indenter had finer meshing. In our analysis, the number of elements ranged from 432 to 720, depending on specimen thickness. The size of the elements at the center of the top surface of the specimen was about 7% of the radius of the indenter. The tissue was modeled as a viscoelastic material as described above and the indenter was treated as a rigid shell.

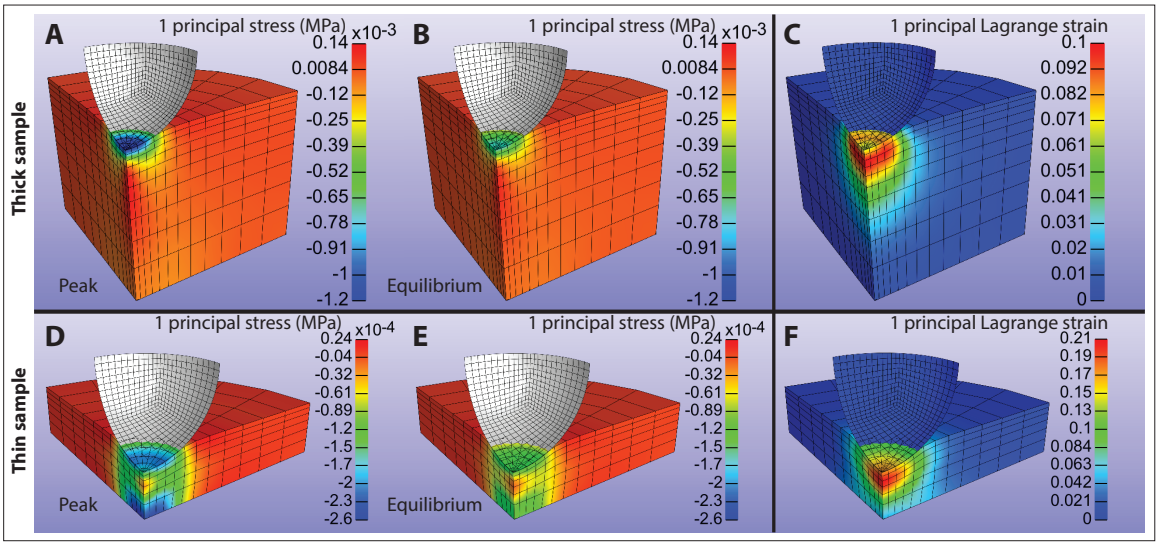

Figure 2.2. Stress and strain maps of one of the thickest samples (7.2mm, sub-figures A, B, C and the thinnest sample (2.2mm, sub-figures D, E, F). Sub-figures A and D show the maximum (peak) first principal stress. Sub-figures B and E show the first principal stress at equilibrium. Sub-figures C and F show the first principal Lagrange strain at the maximum indentation depth of 0.5mm. The maximum first principal strain for the thickest sample and the thinnest sample are 0.1078 and 0.2125,

respectively.

For FE calculations, clamped boundary conditions were placed on the bottom of the tissue slice. Axisymmetric boundary conditions were applied on the y=0 and x=0 planes of the tissue. Lastly, frictionless facet-to-facet sliding contact with auto penalty was prescribed between the tissue and the indenter, with the indenter surface set as the "master" and the top surface of the tissue sample as the "slave". Indenter-tissue friction was assumed to be negligible because the tissue was hydrated and thick [45]. FE calculations and a coupled optimization scheme were performed within FEBio. The optimization scheme used a local search (Levenberg-Marquardt) algorithm to find the best-fit model parameters [E, g_1, g_2, τ_1, τ_2] that minimized the value of the objective function defined by

$$\chi^2 = \sum_{i=1}^{n} [F_i - y(t_i; a)]^2 \tag{2.3}$$

where (F_i,t_i) is the experimentally obtained force-time data, t_i; is the function that describes the model, and **a** is the vector of the unknown material parameters [E, g_1, g_2, τ_1, τ_2]. The load data was sampled and averaged for every 3s interval so each indentation (10s ramp and 180s hold) would produce 63 data points (i.e. i=63 in Eq. 2.3). The convergence tolerance of the objective function was $1\text{x}10^{-6}$. The upper and lower bounds for each material parameter are shown in Table 2.2.

Parameter	E(MPa)	g_1	g_2	τ_1	τ_2
Range	[0.000,1]	[0,2]	[0,2]	[1,100]	[1,500]

Table 2.2. Upper and lower bounds for each material parameter.

2.2.4 Statistical Analysis

A general linear regression model was fit to the material parameter data (Y=G_o and Y=G_∞). Given the repeated cervical samples within a subject, the statistical assumption of independence is violated. Failure to account for this non-independence will lead to biased estimation of the variance

parameters. To account for these repeated measurements within each subject, the regression models were estimated based on the method of generalized estimating equations (Eq. 2.4) , [46, 47]. The GEE method accounts for varying cluster sizes within each subject. Data was organized according to indentation site and labeled with patient sample ID (Table 2.1). The relative influence of pregnancy status (PGS), age of patient (AGE), number of previous vaginal deliveries (PVD), axial location (i.e. slice number, SL), and radial location (RAD) (Table 2.3) on the results was determined using the GEE method and reflected in the β_i coefficients. A p-value is associated with each β_i, where a low p-value indicates a strong correlation between a given parameter and the expected response.

$$Y = \beta_0 + \beta_1 PGS + \beta_2 PVD + \beta_3 SL + \beta_4 AGE + \beta_5 RAD \tag{2.4}$$

Input variable	Description	Data range
PGS	Pregnancy status	1 for pregnant and 0 for non-pregnant
AGE	Age of patient	24-49 in our sample
PVD	Number of previous vaginal deliveries	0-4 in our sample
SL	Slice number	1-4
RAD	Radial location	18-65 where 0 is at the inner canal [a]
[a] Reference Fig. 1A for how RAD was measured		

Table 2.3. Input variable description and data range.

2.3 Results

Nonpregnant (NP) and pregnant (PG) human cervical tissue exhibit a time-dependent force response to a ramp-hold in spherical indentation. Representative indentation stress, strain and force-relaxation responses are given in Figures 4.2 and 4.3. The maximum compressive Lagrange strains for one of the thickest (7.2mm) and thinnest (2.2mm) sample are 0.102 and 0.218, respectively, with maximum compressive equilibrium strain located directly under the indenter tip (Figure 2.2C and F). For our thick samples over 5mm, this strain result matches well with the indentation strain, which

represents an averaged strain value for the infinite half-space assumption. Indentation strain is calculated by $0.2(h/R)^{1/2}$ [48], and for the test parameters used here it is equal to 0.082.

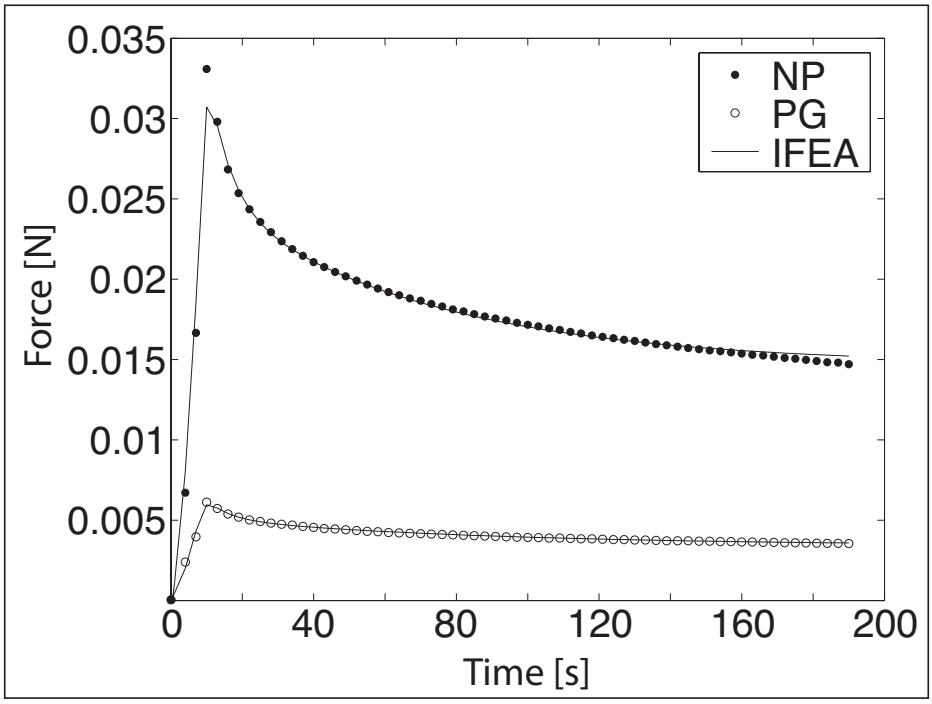

Figure 2.3. Representative force-relaxation response to indentation and corresponding IFEA fit for an indentation in the mid-stroma region for an NP and a PG cervical slice. The NP curve represents an indentation on slice 3 of patient NP3. The PG curve represents an indentation on slice 1 of patient PG3. The final value of the objective functions of both optimizations are $8.1\text{x}10^{-7}$ and $3.3\text{x}10^{-8}$, respectively.

To quantify viscoelastic material parameters from the force - time - indentation data, the analytical viscoelastic indentation solution was fit to each force-relaxation curve. This analytical solution provided reasonable initial guesses for the IFEA, with the FE solutions converging with at most 20 major iterations and 106 minor iterations. The average of the final objective function value was $7.8\text{x}10^{-7}$ with a maximum value of $1.9\text{x}10^{-5}$ for all fits. The quality of the fit can be seen in Figure 2.3. To measure the repeatability of indentations on the same site, the coefficient of variation (c_v) is

calculated by,

$$c_v = \frac{\sigma}{\mu} \tag{2.5}$$

where sigma is the standard deviation a material parameters at a single indentation location and μ is the mean. The mean value of c_v for G_os and G_∞s on the same site are 10% and 8%, respectively.

The instantaneous shear moduli G_o and equilibrium shear moduli G_∞, averaged for indention sites across individual cervical slices, are reported in Figure 2.4 where slice locations within each cervix are indicated. For some cervices there is a difference in instantaneous and equilibrium moduli between the different axial slices within each cervix. For NP tissue, cervical tissue that is closer to the internal os for patients NP1 and NP4 are statistically stiffer when compared to other axial slices from each cervix (Student's t-test, $p<0.05$). In other words, axial slice 1 from these cervices had a higher instantaneous G_∞ and equilibrium G_o shear moduli. This axial heterogeneity was not found for tissue taken from patients NP2, NP3, and NP5, and a conclusion cannot be made for patients NP6, NP7, and NP8 because one slice was tested. For PG tissue, the axial slice closer to the internal os for PG4 is stiffer when compared to axial slices closer to the external os (Student's t-test, $p<0.05$). This trend was not the case for PG3, and other PG tissue did not have multiple slices tested.

The viscoelastic material parameters for NP and PG cervices, averaged across all specimens, are reported in Table 2.4. NP tissue had a statistically larger G_o and G_∞ when compared to PG tissue ($p < 0.05$ and 0.01, respectively) while relaxation ratios (G_∞/G_o) and relaxation time constants (τ_1 and τ_2) remained similar ($p > 0.05$).

Nonpregnant (NP)/Pregnant (PG)	g_1 (kPa)	τ_1 (s)	g_2 (kPa)	τ_2 (s)	E (kPa)	G_0 (kPa)	G_∞ (kPa)	G_∞/G_0
NP (n=8)	0.89 ± 0.27	6.8± 2.8	0.54± 0.22	82± 17	5.2± 2.5	5.1± 3.3	1.9± 0.8	0.43 ± 0.07
PG (n=4)	0.70± 0.19	20± 30	0.47± 0.11	112± 97	1.4± 0.7	1.0± 0.6	0.47± 0.24	0.48± 0.05

Table 2.4. Material properties (IFEA results).

2.3.1 Factors Influencing Cervical Material Properties

Pregnancy status (PGS), number of previous vaginal deliveries (PVD), age (AGE), and location relative to the internal os (SL) have a significant influence on G_∞ with different weights where PGS status is the most significant factor (Table 2.5, Figure 2.5) Individual plots of G∞ versus age, PVD, gravida and parity are shown in Figure 2.5A-D. RAD has no significance on G∞. Based on the statistics analysis for the equilibrium shear modulus $G\infty$: (1) PG cervices are softer than NP cervices, (2) women with more previous vaginal deliveries have a stiffer cervix, (3) tissue closer to the internal os is stiffer than tissue closer to the external os, and (4) younger patients have stiffer cervices than older patients. For G_o, the same analysis was conducted but only the PGS variable was statistically significant.

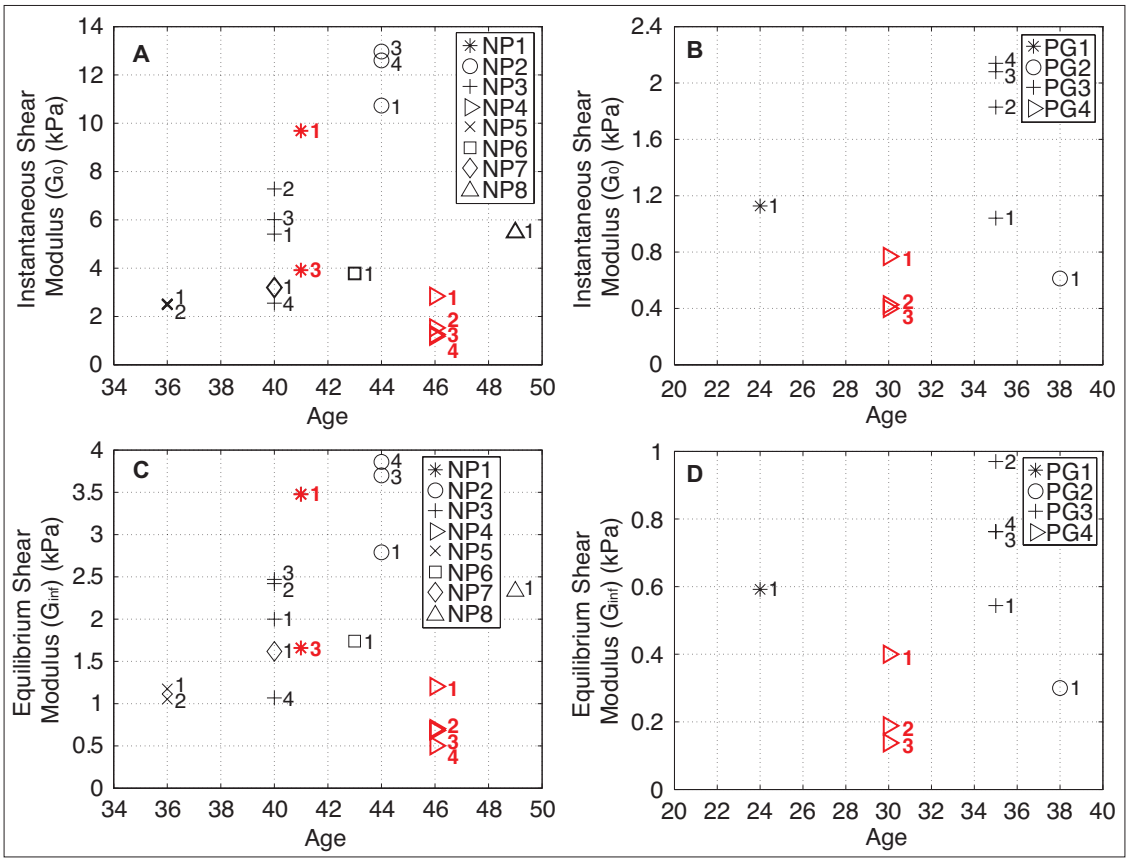

Figure 2.4. (A) Instantaneous shear moduli G_o for NP tissue and (B) PG tissue for each axial cervical slice averaged across all indentation sites. (C) Equilibrium shear modulus G_∞ for NP and (D) PG tissue for each axial cervical slice averaged across all indentation sites. The standard deviations for all slice 1 data, which are representative of the spread for all slices, are reported in Figure 2.5.

Coefficient	Input variable	β Estimate	Standard Error	Significance Code	Input Variable Range Width	Input Weight
β_0	-	3.88	1.29	**	-	-
β_1	PGS	-1.08	0.25	***	1	-1.08
β_2	PVD	0.285	0.095	**	4	1.14
β_3	SL	-0.109	0.053	*	3	-0.33
β_4	AGE	-0.0693	0.0282	*	25	-1.73
β_5	RAD	0.0024	0.0059	-	100	(0.24)

Table 2.5. Statistical results. Significance codes represent p-values, “***” – p∈[0; 0:001], “**” – p∈[0:001; 0:01], “*” – p∈[0:01; 0:05],“.” – p∈[0:05; 0:1], “–” – p∈[0:1; 1]. Input weight is calculated by multiplying estimate by input variable range width

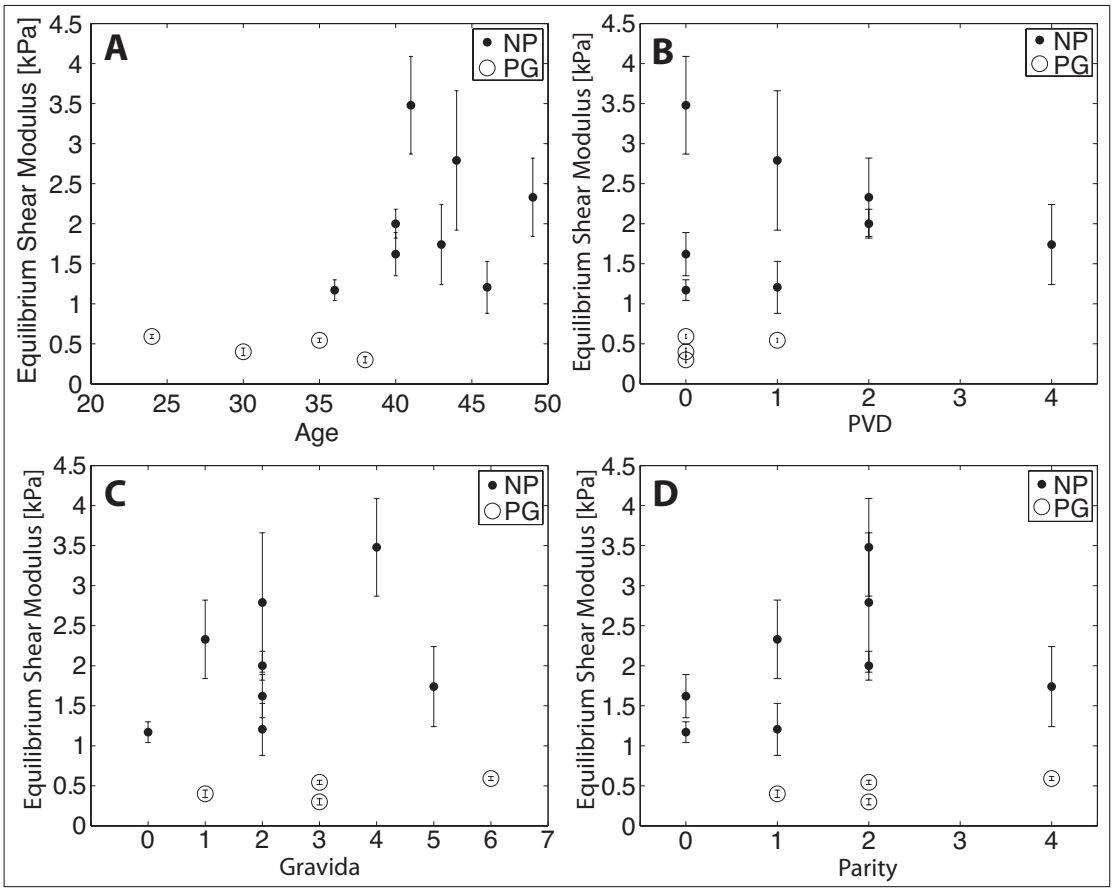

Figure 2.5. Equilibrium shear modulus of slice 1 of each cervix as a function of (A) patient age (AGE), (B) number previous vaginal delivery (PVD), (C) gravida, and (D) parity.

2.4 Discussion

This study reports the compressive time-dependent mechanical behavior of cervical tissue using a spherical indentation technique and viscoelastic material parameters which were quantified through an analytical solution and an inverse finite element method (IFEA). There is a significant difference in the instantaneous G_0 and equilibrium G_∞ stiffness between nonpregnant (NP) and pregnant (PG) tissue, consistent with the findings from our previous mechanical tests on human cervical tissue [11, 49]. Interestingly, there is no difference in the ratio G_∞/G_o when comparing PG and NP specimens, despite the difference in the absolute values of G_0 and G_∞. It was also found that the

obstetric history, indicated by number of previous vaginal deliveries (PVD), and the age (AGE) of the patient are correlated with cervical stiffness. Heterogeneity is found in the axial direction (SL) for some cervices, where axial slices closer to the internal os are stiffer compared to axial slicers closer to the external os. This axial heterogeneity was also found in early studies by Conrad et al., where cervical tissue strips pulled in tension were mechanically stiffer closer to the internal os [50] This difference in material properties is not found in the radial direction (RAD) within the mid-stromal region. However, we do note that since most indentations were clustered in the mid-stroma region, this regression analysis is not ideal to test the RAD variable.

The analytical solution presented here was able to calculate a first estimate of viscoelastic material parameters for the cervical tissue, and the solution provided an initial parameter guess for an IFEA optimization. In the Hertzian contact assumption for the analytical solution, the specimen was modeled as an infinite half-space. This situation is often valid when indentation depth is less than 10% of the thickness of the specimen [51, 52] [43] [44, 53]. In this study, for samples that were more than 5.0mm thick the analytical solution for the equilibrium shear modulus $G\infty$ was 18% greater than the IFEA solution. Since for the majority of our specimens the indentation depth of 0.5mm} was considerable compared with the thicknesses of the samples, we expected a substrate-induced stiffening reflected in larger values for the moduli given by the analytical solution. The majority of our samples ranged from 2.2mm to 5.0mm thick, and for these samples the effect of the rigid substrate was detected by the indenter and the material parameters for the tissue appear to be stiffer in the analytical solution. Comparing the equilibrium values between the analytical and IFEA solution, the shear moduli of the tissue for the analytical solution was 60% and 25% greater than those in IFEA solution for the 2.2mm and the 5.0mm thick samples, respectively.

Axially slices were used in this indentation study to compare and validate our results with previous results from uni-axial compression tests done on cored biopsy plugs. These biopsy plugs were tested in compression where the axis of loading matched the indentation loading axis such that loading was done parallel to the inner canal. Similar to these results, the PG tissue was softer than the NP tissue [11, 27]. However, the equilibrium shear modulus $G\infty$ measured using indentation (Table

2.4) was slightly higher than the modulus that was measured using uni-axial compression tests of 8mm cylindrical biopsy plugs from the mid-stromal region. The equilibrium shear moduli $G\infty$ measured at 1% compressive strain for these biopsy plugs were on average 1 and 0.3kPa for NP and PG tissue, respectively. The reasons for the slight difference are most likely the swelling and softening effect caused by cutting the biopsy from the larger bulk tissue. In indentation, we avoid this effect by testing intact cervical tissue specimens that preserve the collagen fibers that are located perpendicular to the axis loading.

The general linear model based on the method of GEE was able to distinguish the relative influence of pregnancy status, age, gravida, parity, number of previous vaginal deliveries, slice number, radial location on the material parameters of human cervical tissue. For the statistical model input variables (X_i), the general rule is to include as many important factors while excluding those which are correlated. In our case, PGS, PVD, SL, AGE and RAD were the most important factors included in the model, with parity and gravida, being highly correlated with PVD. While correct specification of the covariance structure remains integral for modeling the marginal mean parameters, the GEE method is robust to misspecification of the covariance structure. The parameters in our GEE-based model were population-averaged in that the interpretation of model parameters carry the same interpretation as a standard logistic regression model.

2.4.1 Limitations and Future Work

The framework for interpreting the indentation results presented here offer a straight-forward approach to analyzing the time-dependent material response of the tissue to deformation caused by spherical indentation, with evidence to support the use of a quick and reliable analytical solution to obtain material parameters for specimens 10 times thicker than the maximum indentation depth. The indentation methodology presented here for the measurement of cervical material properties has limitations and improvements to this method are the basis of our current and future work.

First, the material model used is phenomenological and cannot account for the large deformation tensile behavior of the tissue. Here we assume that the time-dependent deformation mechanisms of the tissue are caused by the viscoleastic rearrangement of the collagen network. Due

to hydrated nature of biological tissues, it is also possible that the poroelastic effects of the fluid being squeezed out of the tissue under pressure contributes to the time dependent behavior. In addition, the compressive material properties measured here are limited to a small strain analysis. Our previous compression and tension tests on human cervical samples showed that in compression the equilibrium response of the tissue remains linear until approximately 25% compressive strain [11, 27]. In tension, the tissue becomes nonlinear at a much lower strain level. Therefore, the material parameters reported here can only be used in a compressive and small strain regime. In a physiologic setting during pregnancy the cervix may undergo large deformation, with a mix of tensile and compressive modes of deformation. Therefore, further work is being done to determine the appropriate combination of hyperelastic, viscoelastic, and poroelastic models that can best predict the material behavior of human cervical tissue. Regardless of these model limitations, meaningful comparisons of cervical material properties can be made between tissue taken from women of different obstetric backgrounds and ages as demonstrated by the regression analysis. In addition, spherical indentation allowed us to more carefully measure the small strain material response of the tissue because the swelling artifact from specimen preparation is drastically reduced with these larger specimens when compared to the traditionally smaller cut biopsy specimens.

The second limitation of this study was that} anisotropy was not included in this first analysis of the indentation response of human cervical tissue. There is evidence to suggest that cervical stroma has three seamless zones of preferentially aligned collagen fibers, where collagen fibers in the middle zone preferentially align in circumferential direction and collagen fibers in the outermost and innermost zones preferentially align in the longitudinal direction [17, 18]. Here, isotropic assumptions are made because this was our first attempt at interpreting the indentation data and the deformation was kept within a small-strain regime which can be verified by the maximum first principle strains in Figure 2.2. In addition, our previous uni-axial compression tests on cube cervical specimens showed that in equilibrium there was a limited anisotropy effect on the material behavior of the tissue. In the future, we plan to account for potential tissue anisotropy by including fiber directionality in our material model and by testing the tissue with various geometries and directions of the indenter tip [54]. Although an

axisymmetric FE model would have been faster for this IFEA analysis, the quarter wedge geometry used here and implemented in FEBio offers the flexibility for implementation of fiber directionality for future analysis.

Lastly, the pregnant specimens tested are from patients with accretas. These cervical specimens may be affected by this pathologic condition of the placenta. Currently it is unclear how these pregnant cervical specimens are different from normal pregnancy, and further histological analysis comparing normal and accreta specimens and adding pathological conditions as input parameters in the statistic analysis are needed. In addition, we assume that the pregnant samples used in this study represent tissue that has undergone remodeling. Evidence supporting this assumption include mechanical tests done on ex-vivo mouse cervical tissue. These tests have shown that the cervix progressively remodels throughout pregnancy, with accelerated ripening happening before dilation [2, 55-58]. Most recently, an in-vivo mechanical test on human cervix using an aspiration tool gave evidence that the cervix softens by the third trimester and before labor [3]. Again, future histological analysis of the pregnant tissue samples will be needed to confirm our hypothesis.

2.5 Conclusion

This chapter reports the compressive viscoelastic material parameters of human cervical tissue taken from hysterectomy patients with various obstetric histories. Spherical indentation method was developed to quantify these time-dependent material parameters on ex-vivo human tissue. Since we understand that anisotropy and collagen fiber network is key to keeping cervix shut, the next step of the research will be to understand the collagen fiber network's properties and a good method would be to use a non-invasive optical imaging tool to study the ultrastructure of the collagen fiber network.

3 Collagen Fiber Orientation and Dispersion in the Upper Cervix of Non-Pregnant and Pregnant Women

3.1 Introduction

In this study, we use OCT [59], a non-invasive imaging technique based on the principle of low coherence interferometry, to image and characterize the cervical fiber ultrastructure. Using OCT, the sample morphological information in depth is obtained by interfering backscattered photons from a sample irradiated with a broadband low coherence source with a reference beam. A typical OCT system can achieve a high axial resolution at the micron level, a penetration depth up to 2 mm, and video rate data acquisition, and thus emerges as a promising image modality to image a variety of organ systems[35, 60, 61]. In particular, efforts have been made to image cervical tissues for cancer detection [62-64] by analyzing the layered structure of the epithelium, the basement membrane, and the stroma. In addition to cancerous structure, OCT can be also used to image the collagen fiber network. Our previous work has demonstrated the feasibility of imaging entire axial cervical slices [22] . This was enabled by an image-stitching algorithm to increase the field of view, encompassing entire axial slices (~3 cm × 3 cm), which allowed for assessment of collagen fiber orientation trends and for identification of unique anatomical regions. Our previous methods for fiber orientation estimation [65, 66] targeted extracting dominant fiber orientation in a subregion, however it could not provide detailed information about non-dominant orientations, resulting inaccuracy in the evaluation of fiber dispersion.

Building on our previous OCT investigation of the human cervix and the work of others, we report collagen fiber orientation maps of whole, unfixed, axial cross-section slices of non-pregnant and pregnant human cervical tissue to visualize anatomically-relevant trends. Due to the complex structural environment of the cervix, we hypothesize that the fiber orientation and local dispersion is heterogeneous with regions determined by anatomic location. We postulate that the homogeneity of fiber orientation and local dispersion will depend on four anatomic quadrants of the cervix (posterior, anterior, left and right) and will depend on the radial location from the inner canal. In this paper, we

present the methodology of OCT imaging on human cervical tissue, and describe the fiber orientation maps and collagen fiber orientation distribution and dispersion across four quadrants and different radial distances from the inner canal.

3.2 Methods

3.2.1 Sample collection and preparation

Thirteen human cervices were collected from consented hysterectomy patients by an IRB approved protocol at Columbia University Medical Center (Table 3.1). Among the cervices, 11 were from non-pregnant (NP) patients undergoing hysterectomy for benign indications and 2 were from pregnant (PG) patients undergoing cesarean hysterectomy due to abnormal placentation. Patient age ranges from 36 to 49 and parity number from 0 to 5. The cervices were sliced perpendicular to the inner canal immediately after hysterectomy using a custom-built slicer. The thickness of each slice was 3-5 mm. Axial slices within the upper half of cervix were excised. In this study, we particularly analyzed the slice that is closest to uterus for each sample. All samples were kept on dry ice and then stored at -80^{o}C for later imaging. A more detailed protocol used for sample collection and preparation is described in our earlier work [29].

Specimen Number	Age	Pregnancy Status	Gravidity / Parity	Obstetric History
1	42	NP	5/1041	1 VD, 3 VTOP
2	41	NP	6/4024	4 FT VD, 1 VTOP, 1 SAB
3	46	NP	0/0000	
4	40	NP	2/0020	VTOP, SAB
5	43	NP	1/1001	VD
6	49	NP	1/1001	VD
7	46	NP	4/1031	VD, 3 VTOP
8	40	NP	3/3003	3 VD
9	48	NP	9/5045	5 FT VD, 4 VTOP
10	36	NP	4/4004	4 CS
11	46	NP	3/3003	VD, CS, VBAC
12	30	PG	5/1031	CS, 3 SAB
13	42	PG	5/2022	Lack info

Table 3.1. Patient demographics of specimens used for this study. Gravidity is equivalent to the total number of pregnancies. Parity data is presented in TPAL recording system. TPAL stands for term, preterm, aborted, and living deliveries, corresponding respectively to each of the 4 digits. VD = vaginal delivery, VTOP = voluntary termination, FT = full term, SAB = spontaneous abortion (miscarriage), CS = cesarean section, VBAC = vaginal birth after cesarean.

3.2.2 OCT scan and fiber recognition algorithm

Before OCT imaging, cervical slices were thawed in phosphate buffered saline (PBS) overnight at 4°C, and the surface closer to the internal os was microtomed. During the imaging procedure, the cervical slice was laid on top of a gauze soaked in PBS to keep the tissue hydrated. Samples were imaged using a commercial OCT system, Telesto I (Thorlab GmbH, Germany). The

system is an InGaAs based system with its source centered at 1325 nm and a bandwidth of 150 nm. The axial and lateral resolutions are 6.5 μm and 15 μm in air, respectively. In our experiments, each volume consisted of 900 × 900 × 512 voxels, corresponding to a tissue volume of 4.5 mm × 4.5 mm × 2.51 mm (in air). Samples were placed in a linear translation stage underneath the objective. For each sample, we obtained multiple volumes. There was an overlap proportion of at least 10% between two adjacent volumes. A white light camera obtained an image of the sample corresponding to the OCT field of view (FOV). The camera images and OCT images were calibrated by the default factory setting.

Volumetric data was stitched based on the shift invariant feature in camera image within the *en face* plane and surface information of the OCT data in the axial direction[22]. Upon generating the three dimensional data, parallel *en face* images were obtained 245 μm beneath the surface to perform 2D fiber directionality and dispersion analysis [22]. Fiber orientations were extracted for each pixel (5 μm × 5 μm) by optimizing a pixel-wise fiber orientation method [67, 68] for OCT image datasets. In each *en face* image, the collagen fiber region was masked based on the signal to noise ratio. Then, the image was enhanced through histogram stretching. The image was sharpened by second order Butterworth high pass filter and subsequently denoised by a median filter. A weighted summation scheme was utilized to determine the fiber orientation at each pixel over the entire region. For a pixel of interest, p_0, there were multiple candidate directions α_j towards its neighboring pixels, p_1 and p_2. A weight was assigned to each candidate direction as following:

$$w_j = w_i \times w_d \tag{3.1}$$

$$w_i = \frac{1}{3} - std(p_1, p_0, p_2) \tag{3.2}$$

$$w_d = \frac{1}{dist(p_0, p_2 \text{ or } p_1)} \tag{3.3}$$

The weight was determined by two factors, w_i and w_d. The first factor, w_i, was the intensity variations between the pixel of interest (p_0) and its neighboring pixels (p_1 and p_2) along a particular direction. The second factor, w_d, was the corresponding distance between the pixel of interest (p_0) and

the neighboring pixel (p_1 or p_2). The direction, α, of target pixel p_0 is determined by the weighted circular mean of all direction candidates as described in equation 3.4:

$$\alpha = \arg\left(\sum_{j=1}^{N} w_j \times \exp\left(i\alpha_j\right)\right) \tag{3.4}$$

where N is the number of direction candidates around pixel p_0. Given the direction information of each pixel, we generate the directionality map of the whole OCT image.

Based on the pixel-wise orientation information, we obtained the directionality map of collagen fibers within the *en face* image. The directionality map was further divided into sub-regions of 400 μm × 400 μm along the radial direction in the four anatomical quadrants from inner canal to outer edge. In each 400 μm × 400 μm subregion, a 2D von-Mises probability density function,

$$P(x) = \frac{e^{b\cos(x-\theta)}}{2\pi I_0(b)} \tag{3.5}$$

was fit to the pixel-wise orientation data to determine the fiber direction θ and the concentration parameter b using a least squares methods (MATLAB (MathWorks, R2014b) function fit). $I_0(b)$ is a modified Bessel function of the first kind of order 0. Here, $\theta \in [0,2\pi)$ is the dominant fiber direction and $b > 0$ is the concentration parameter [69]. The concentration parameter b describes the dispersion level of Von Mises distribution. When b approaches 0, the distribution gets closer to isotropic (circular in 2D case), and as b increases to infinity the distribution gets closer to perfectly aligned fibers. In other words, b is inversely related to fiber dispersion where a low b describes a high fiber dispersion and a high b describes a low fiber dispersion.

3.2.3 Statistical analysis

Rather than t-test on pairwise comparison, a group of analysis of variance (ANOVA) tests were performed in MATLAB using one-way ANOVA function (anova1) and multiple comparison function (multcompare) to compare the von-Mises fiber ultrastructure parameters (b and θ) between NP and PG specimens and among NP specimens with different parity. The data normality was verified by Kolmogorov–Smirnov test in MATLAB (kstest function) before ANOVA. The homogeneity of these fiber ultrastructural parameters within individual sample slices were assessed by comparing results

between circumferential quadrants, inner and outer radial zones, and the 400 μm × 400 μm radial subregions in the outer zone.

In the circumferential direction, the cervical slice was divided into four anatomical quadrants. In the radial direction, the cervical slice was divided into inner and outer zones. The border between the inner and outer radial zones was manually determined by differentiating the distinct patterns of fiber orientation of the two zones. The radial direction was also subdivided into 400 μm × 400 μm subregions as described by the pixel-wise fiber tracking method above. Parity is the number of times that a woman has given birth. We divided our patients into three parity groups: nulliparous patients (n = 2) who have never given birth, primiparous patients (n = 4) who have given birth once, and multiparous patients (n = 5) who have given birth two or more times.

When b and θ were compared between different samples, averages were taken of the results from all 400 μm × 400 μm subregion within the quadrant and radial zone. When b and θ were compared within a specimen, the variance of b and θ along radial direction within each quadrant and zone were measured by calculating the standard deviation. All ANOVA tests were performed in MATLAB using the anova1 function where a p-value of 0.05 was considered statistically significant.

3.3 RESULTS

3.3.1 OCT *en face* images and fiber orientation maps

The regional collagen fiber architecture of the upper half of the human cervix is depicted in 2D image a fixed axial distance below the surface in Fig. 2 using the method in [65, 70]. In 9 NP tissue samples out of the 11 NP samples imaged, two radially zones are found with distinct fiber orientation characteristics (Figure 3.1). In these tissue slices there is an inner zone with collagen fibers preferentially aligned in the radial direction and an outer zone with collagen fibers preferentially aligned in the circumferential direction. The shape of the inner zone and the fiber orientations in this zone are highly affected by the shape of the inner canal. The inner zone can be relatively wide or narrow, where Figure 3.1AB shows the widest inner zone which is around 30% of the slice radius and Figure 3.1C-D shows a narrower inner zone. In the 4 remaining slices, including both pregnant

samples, there is no inner zone and the whole slice is dominated by circumferentially aligned fibers (Figure 3.1EF). For many slices (Figure 3.1CD), the inner canal opening aligns from left to right. Others have the inner canal opening aligning from anterior to posterior, or the inner canal is round or has an irregular shape. Based on the samples we examined, there is no clear relationship between the inner zone size and patient parity.

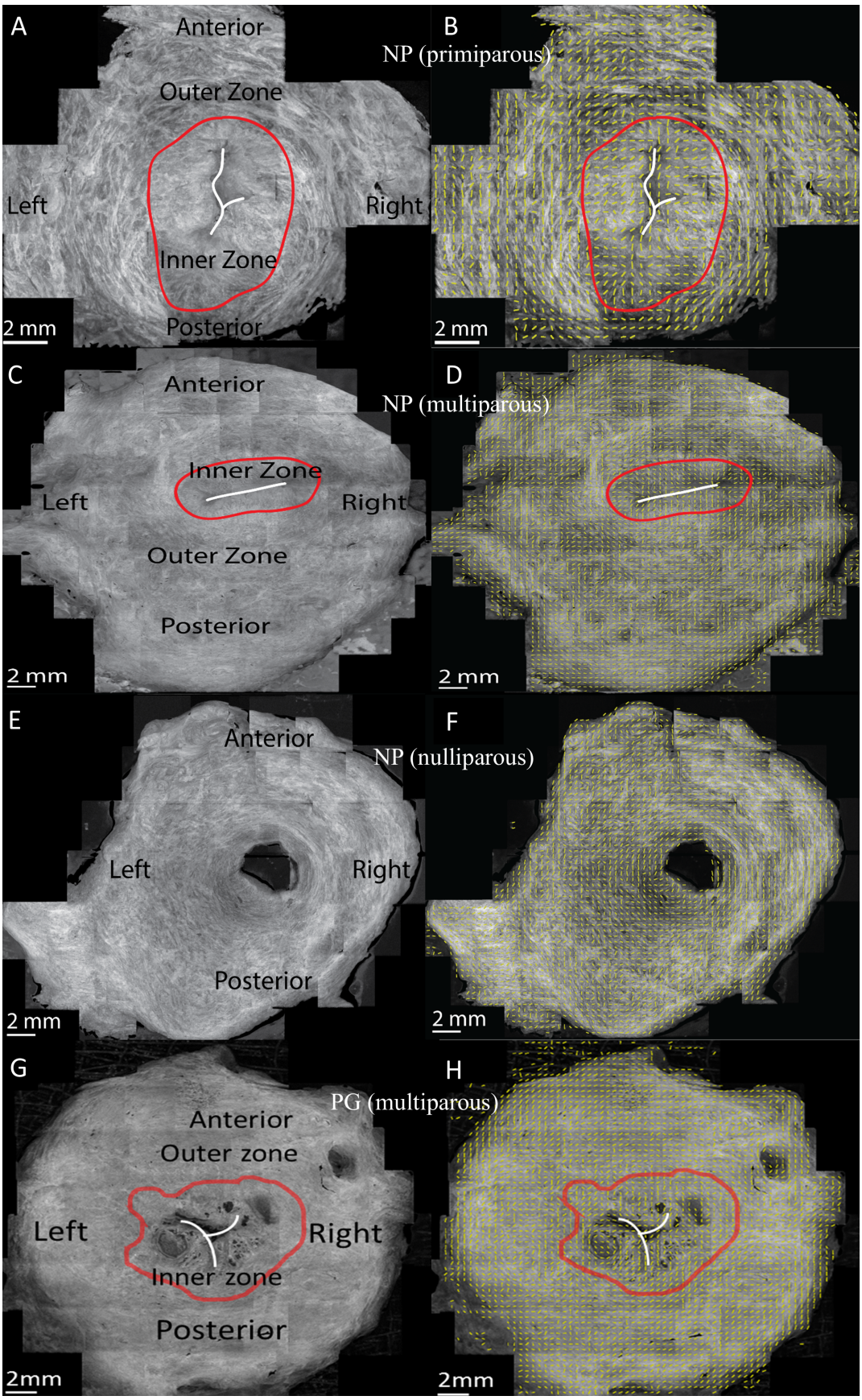
A
Anterior
Outer Zone
Left
Right
Inner Zone
Posterior
2 mm
B
NP (primiparous)
2 mm
C
Anterior
Inner Zone
Left
Right
Outer Zone
Posterior
2 mm
D
NP (multiparous)
2 mm
E
Anterior
Left
Right
Posterior
2 mm
F
NP (nulliparous)
2 mm
G
Anterior
Outer zone
Left
Right
Inner zone
Posterior
2mm
H
PG (multiparous)
2mm

Figure 3.1. (A), (C), (E), (G) OCT *en face* image taken 245 μm beneath the cut surface and (B), (D), (F), (H) overlaid fiber orientation map. The white line sketches the inner canal. The red contour delineates the inner radial zone according to local fiber orientation. Among NP specimens, (A) has a wide inner radial zone, (C) has a narrow inner radial zone, and (E) has no inner radial zone. The yellow bars in (B), (D), (F), and (H) show local dominant fiber orientation in each 400 × 400 μm sub-region. (A)-(B), (C)-(D), (E)-(F), (G)-(H) are Speicemen 1, Speciemen 2, Speciemen 3, and Speciemen 13 in Table 1 respectively.

We validated our pixel-wise fiber recognition algorithm on synthetic data in Figure 3.2, where our algorithm accurately estimates the directionality of segments oriented at various orientations (A-B) and circular shape (C-D). The new pixel-wise fiber recognition algorithm is superior to the gradient-based method because the pixel-wise method is able to capture the existence of distinct fiber families at different orientations, especially non-dominant orientations. A directionality map using the pixel-wise fiber orientation algorithm of a cervical sample is shown in Figure 3.2(F), in comparison with the OCT *en face* image in Figure 3.2(E). The fiber distribution obtained from three subregions using the pixel-wise method and the gradient-based method in [65, 66] were compared in Figure 3.2(G). In general, the estimated dominant direction using two methods approximate each other within each subregion. However, the gradient method is unable to capture the actual fiber distribution of the probability of fiber existence at each angle.

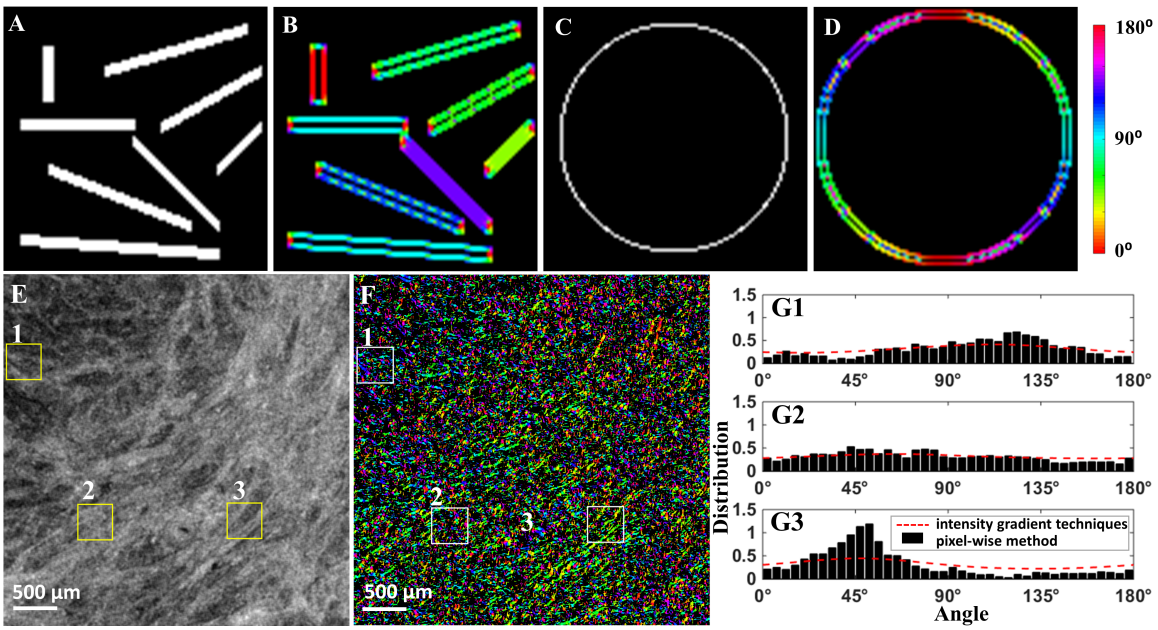

Figure 3.2. (A), (C) Synthetic data for algorithm validation; (B), (D) processed data with pixel-wise fiber orientation. (E) Original OCT image from an *en face* plane (Specimen 8 in Table 1); (F) pixel-wise directionality map; (G1)-(G3) Histogram of orientation obtained from pixel-wise fiber orientation method in sub-regions from 1 to 3. Distribution of fiber orientation in the three regions using pixel-wise fiber orientation method and intensity gradient techniques [14, 15]. Each box is 400 μm × 400 μm.

A typical example of the pixel-wise method on a stitched OCT cervix image comprised of 24 OCT volumes is shown in Figure 3.3. The original OCT image is an *en face* image 245 μm parallel to the cut surface as shown in Figure 3.1(A). From the pixel-wise directionality map, such as Figure 3.3(A), we observe a circumferential trend of fiber in the outer zone. From a zoom-in box in Figure 3.3(B) and Figure 3.3(C) corresponding to a 4 × 4mm region, it shows fiber directions can vary dramatically within a small region. Similar circumferential trends and direction variation patterns are observed in all other cervical samples.

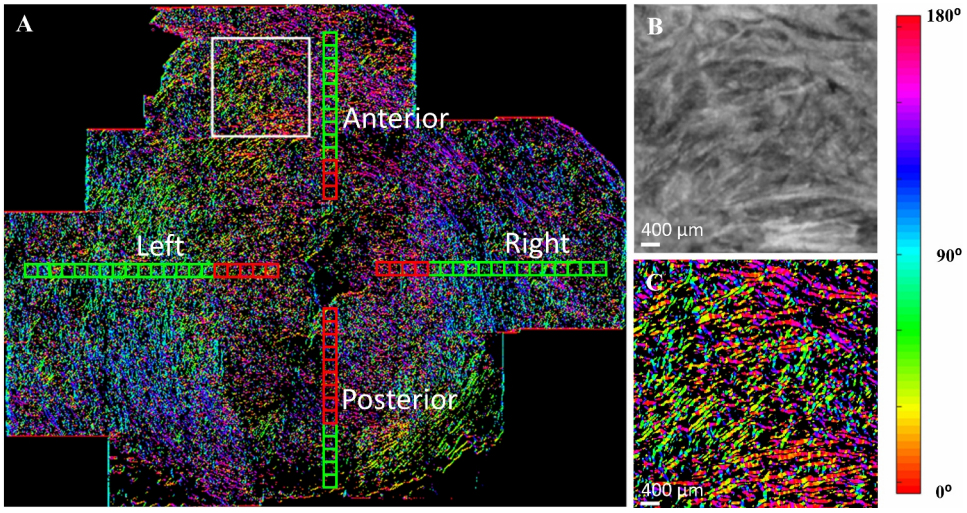

Figure 3.3. A pixel-wise directionality map on an *en face* image parallel from and 245 μm beneath the cut surface (Specimen 1 in Table 1). (A) directionality map with locations of 400 μm × 400 μm subregions corresponding to 80 pixels × 80 pixels.; (B) OCT image within the white box in (A); (C) directionality map within the white box in (B). Pixels with no fiber information are coded in black. Each 400 μm × 400 μm subregion represents a location for the fiber orientation and dispersion analysis in the A (anterior), P (posterior), L (left), and R (right) quadrants. Along the radial direction, the boxes are divided into inner region (red) and outer region (green).

2D von-Mises distribution provides a close fit to the raw fiber dispersion data. Concentration parameter *b* can be as high as 0.820 and as low as 0.010 as shown in Figure 3.4(A)(B). For certain subregions, more than one family of fibers can be observed where the current 2D von-Mises analysis cannot capture these distinct fiber families (Figure 3.4(C)(D)). The fitting for multiple families of fibers will be discussed in discussion.

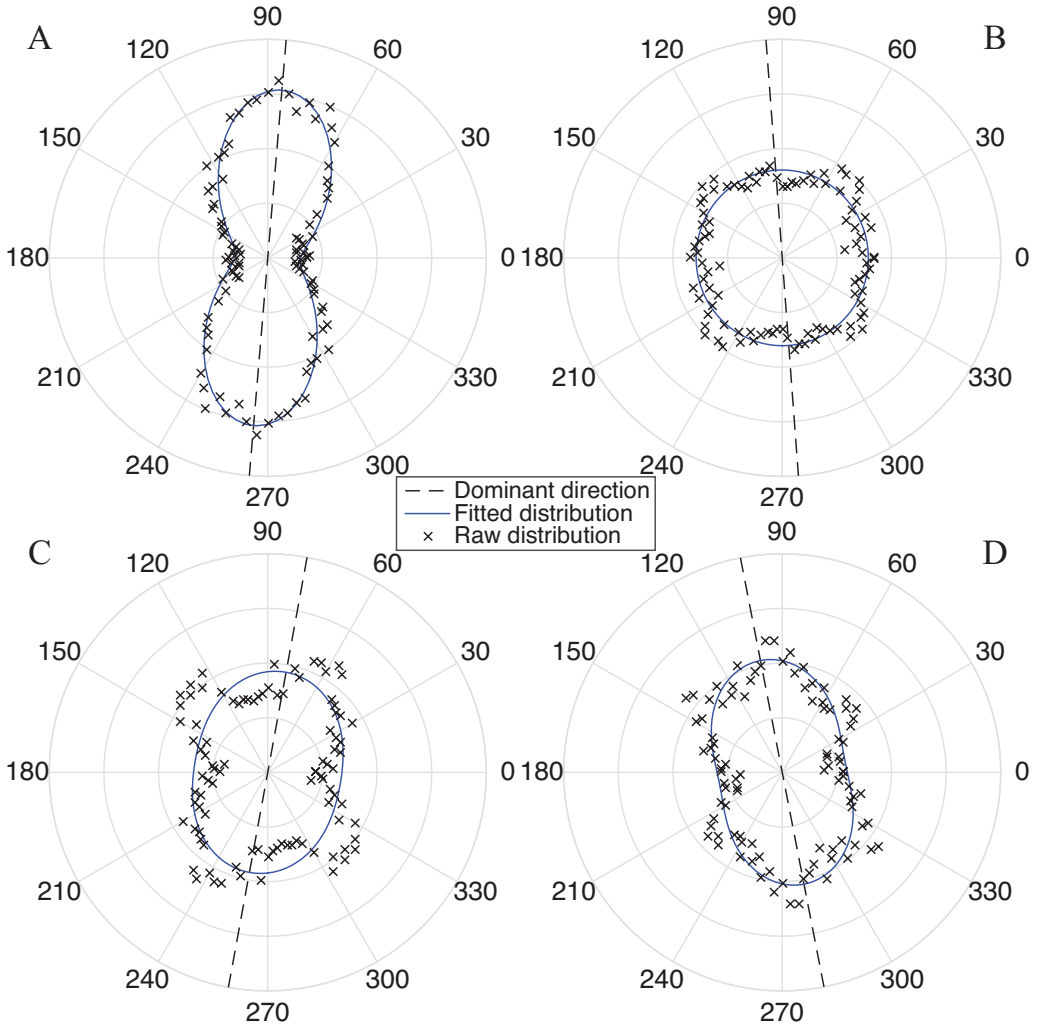

Figure 3.4. Representative fiber distributions found in the upper cervix and corresponding 2D von-Mises fits. The dominant direction θ is shown by dotted line. All four subregions are taken from the outer radial zone of the same NP sample (Specimen 5 in Table 1). A subregion with (A) a single family of fibers that have the most alignment (b = 0.820) and (B) highly dispersed fibers that are randomly oriented in the plane. A subregion with (C) two fiber families and (D) three fiber families. (Note: current distribution fitting methodology cannot distinguish the multiple fiber families.)

3.3.2 The posterior and anterior cervix contains regions of preferentially-aligned collagen fibers

The upper half of the cervix contains zones of preferentially-aligned collagen with distinct fiber directionality and dispersion properties in the posterior, anterior, left, and right quadrants (Figure 3.5). The dominant fiber directionality data θ for each of the 13 specimens averaged across radial subregions in the outer radial zone within each anatomical quadrant are represented in Figure 3.5. For all 13 specimens, including NP and PG, the dominant fiber directionality in the posterior and anterior quadrants of the cervix is in the circumferential direction, with fibers circling around the inner canal. When comparing these anterior and posterior quadrants between specimens, the averaged directions θ are within a small range (≈35°) with one exception of the anterior of one PG sample. In the left and right quadrants, although the average dominant direction for all specimens is circumferential, dominant directions themselves are scattered within a larger range (≈140°), which indicates a higher variability between specimens in the left and right quadrants.

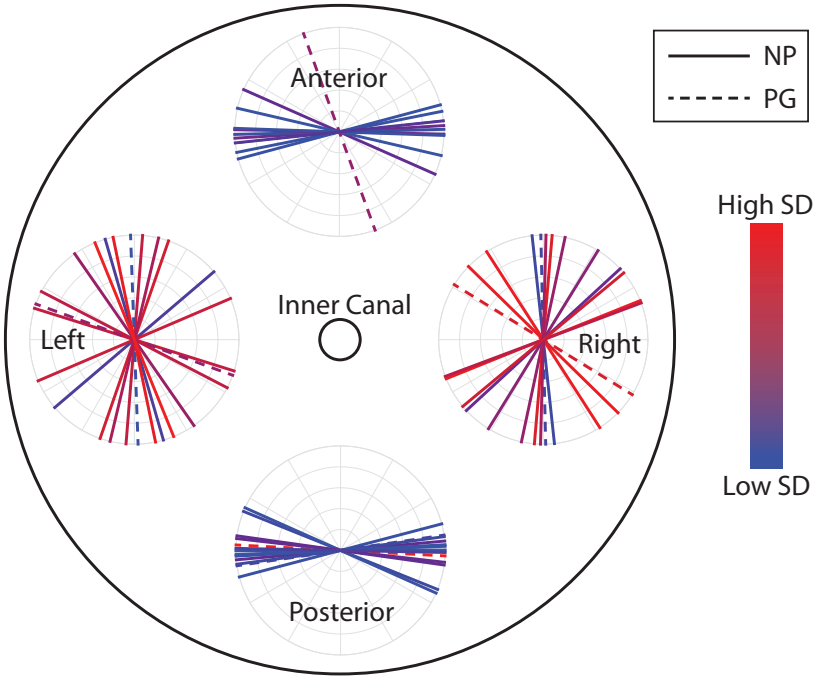

Figure 3.5. The dominant fiber direction θ in the outer radial zone in four quadrants for all specimens imaged. Each circle represents the dominant fiber directions in one quadrant. Each line represents one cervical sample averaged across all 400 μm × 400 μm radial subregions, with the line color representing the standard deviation (SD) between the radial subregions. Red represents higher SD and blue represents lower SD. Posterior and anterior quadrants both have more uniform dominant directions among samples (lines having a narrower spread) and within a single specimen there is lower SD between the radial subregions (lines having a bluish color). Left and right quadrants have a wider spread of the dominant fiber direction between samples, and within an individual sample fiber directions also change more dramatically along radial direction.

The data normality is verified in every radial quadrant and inner/outer regions since Kolmogorov-Smirnov test results accept the null hypothesis (lowest p=0.28). When comparing 400 μm × 400 μm radial subregions within a single slice in the outer zone for NP specimens, the standard deviation (SD) of the dominant direction θ is higher in the left and right quadrants comparing to that in posterior and anterior quadrants (Figure 3.6). This higher SD means fiber changes orientation more

dramatically along radial direction and the tissue is more heterogeneous. This difference is very significant in the outer zone ($p < 0.001$) but not significant in the inner zone ($p > 0.983$). The SD of θ in the outer zone of posterior and anterior quadrants of NP samples is different than the rest regions in NP samples as well as all regions in PG samples. If we group them this way, the difference is very significant ($p = 3.4\times10^{-6}$).

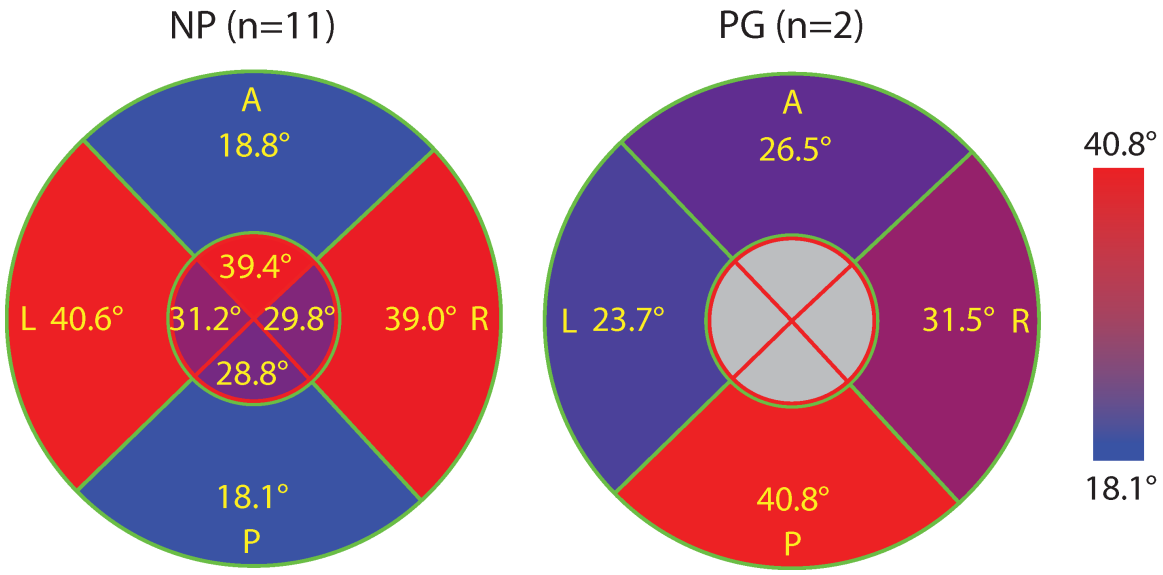

Figure 3.6. The average of the SD of dominant fiber direction θ between radial subregions for NP and PG specimens. Values are shown in eight regions that include the inner and outer radial zones of four quadrants. Each region is color-coded such that red represents higher SD (more heterogeneous θ between radial subregions) and blue represents lower SD (more homogeneous θ between radial subregions). The anterior and posterior quadrants of the NP cervical tissue samples have more homogeneous circumferential fibers compared to its left and right quadrants.

3.3.3 The posterior and anterior of the outer radial zone of NP specimens have the lowest collagen dispersion

The posterior and anterior quadrants of the outer zone in NP specimens have the lowest fiber dispersion in the 400 μm × 400 μm subregions (i.e. highest concentration parameter b, Figure 3.7) compared to other quadrants in NP samples and to all quadrants in the PG samples. The left and right

quadrants of the NP samples have similar fiber dispersion properties compared to all quadrants of the PG specimens (Figure 3.7). Similar to the SD of θ, if we group the outer zone of posterior and anterior of NP samples together and group the remaining regions in NP samples as well all regions in PG samples together, the difference in b is statistically significant ($p = 2.1\times10^{-7}$, see S3 Fig.). Within the PG samples there is no significant difference between quadrants. The variance in fiber dispersion, represented by the SD of concentration parameter b, between 400 μm × 400 μm radial subregions within a single slice are not significantly different (Figure 3.8).

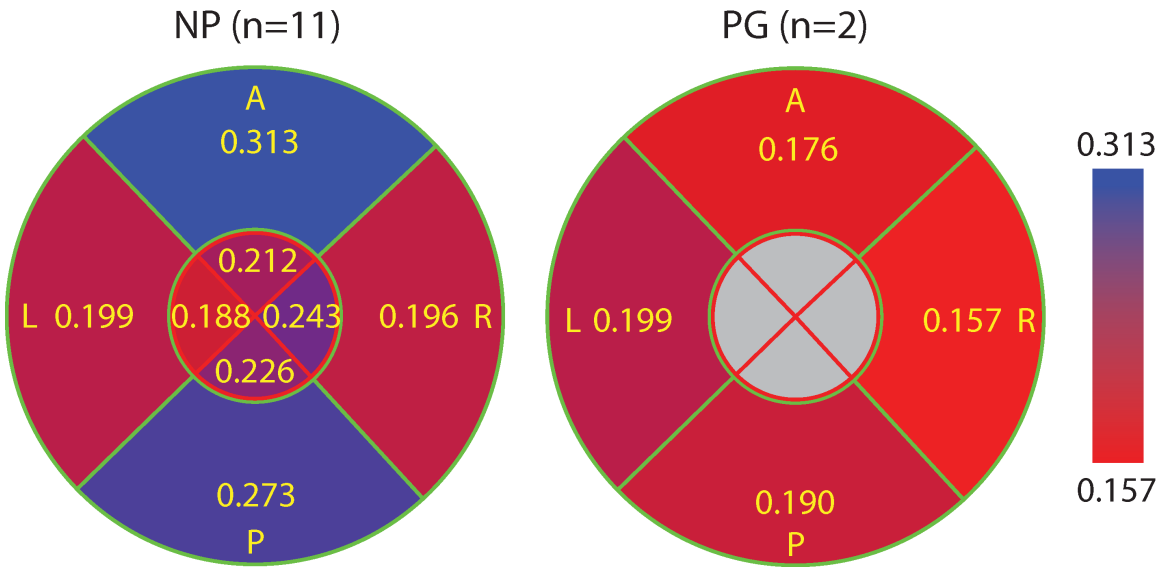

Figure 3.7. The concentration parameter b averaged for all 400 μm × 400 μm radial subregions in each quadrant for all NP and PG specimens. This figure is color-coded such that blue represents higher b (lower dispersion and more aligned fibers) and red represents lower b (more dispersed and randomly oriented fibers). Overall, the collagen fibers of the NP cervices had tighter aligned fibers within the 400 μm × 400 μm subregions compared to the PG samples. Within the NP samples, the A/P quadrants in the outer zone have the most aligned fibers within the 400 μm × 400 μm radial subregions compared to the rest.

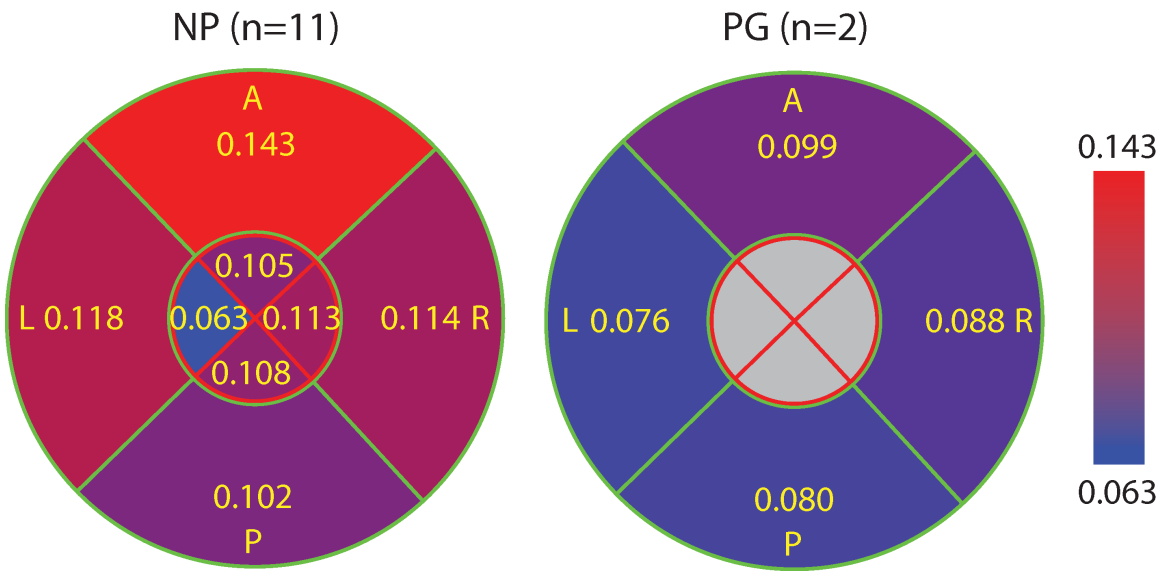

Figure 3.8. The average of SD of the concentration parameter *b* between different radial subregion. This figure is color-coded such that red represents higher SD (relative heterogeneity of *b* along radial direction) and blue represents lower SD (relative homogeneity of *b* along radial direction). The highest value appears in the A quadrant of NP samples and the lower values appear in the L quadrant of NP samples and P/L quadrants of PG samples.

3.3.4 There is difference in dispersion between NP and PG but no difference is found between NP samples with different parity

We found a statistically significant difference in *b* between NP and PG specimens in posterior and anterior in the outer zone (Figure 3.9). In further detail, among four quadrants, *b* of PG specimens has distinctly lower mean values in posterior and anterior than NP specimens, which suggests PG specimens have more dispersed collagen fibers. The difference is significant if we compare the combined posterior and anterior region and combined left and right regions (p between 0.006 and 0.045). Such difference is not found with the variance of θ (Figure 3.10). Among parity groups in NP specimens, there is no difference found for either *b* or θ (Figure 3.9 and Figure 3.10).

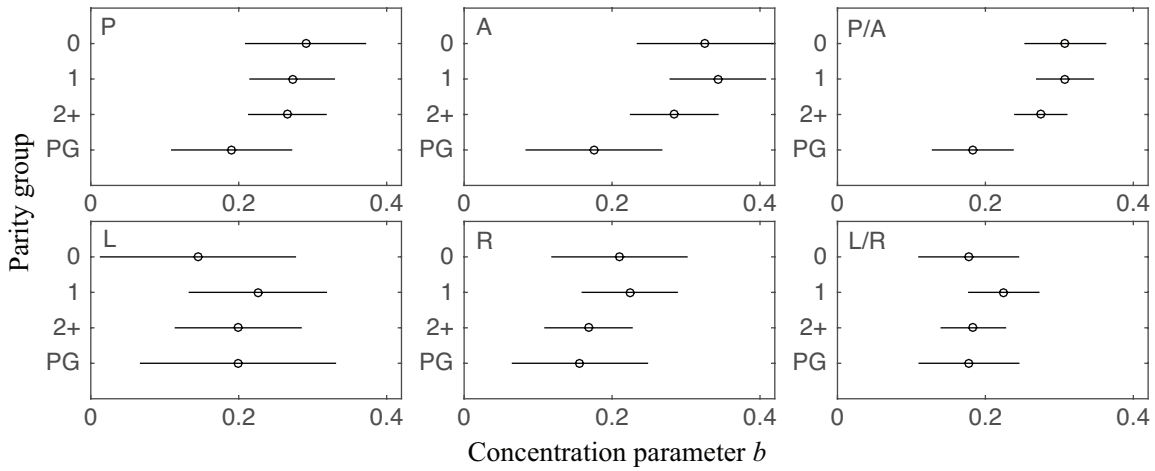

Figure 3.9. Concentration parameter *b* in different parity groups and pregnancy statuses. Four groups are nulliparous NP (group "0", *n* = 2), primiparous NP (group "1", *n* = 4), multiparous NP (group "2+", *n* = 5), and PG (group "PG", *n* = 2). Results from each quadrant in the outer radial zone and some combinations are shown. There is no significant difference between nulliparous NP, primiparous NP, and multiparous NP. In quadrants P/A, PG has a lower *b* than NP groups. This result is significant when we analyze the data from both quadrants combined (*p* between 0.006 and 0.045). No significant difference is found in L/R quadrants.

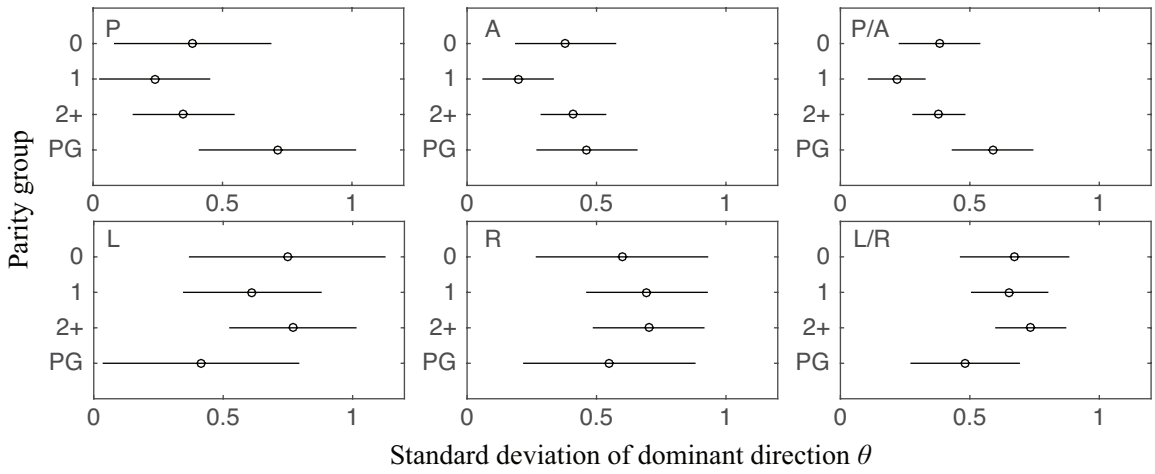

Figure 3.10. SD of dominant direction *θ* in different parity groups and pregnancy statuses. Results from each quadrant in the outer radial zone and some combinations are shown. NP groups do not have significant differences among themselves. Between NP groups and PG, the only significant difference is found between primiparous NP and PG when P/A quadrants are combined (*p*=0.004).

Unlike the analysis for b, nulliparous NP (p = 0.276) and multiparous NP (p = 0.143) do not have a significant difference with PG in the SD of θ. No significant difference is found in L/R quadrants.

3.4 DISCUSSION

In this paper, we present a regional OCT collagen fiber orientation and dispersion analysis of 13 fresh, unfixed human cervical slices. To measure local fiber orientation and dispersion, a new pixel-wise fiber orientation algorithm is developed for cervical tissue analysis. Based on this method, fiber orientation maps are generated to visualize and measure the tissue-level architecture of the upper cervix. In all of the cervical fiber orientation maps, there is a dominant outer radial zone of preferentially aligned collagen fibers circling around the inner canal where the posterior and anterior quadrants are more aligned than left and right quadrants. In 9 out of the 11 non-pregnant samples, there is an additional inner radial zone with fibers preferentially aligned in the radial direction that is perpendicular to inner canal opening direction. In this inner radial zone, though, the trends are difficult to study because this zone also includes mucous glands located around the inner canal opening, which cannot be differentiated from dense collagen fibers.

The NP cervical tissue samples measured in this study have two regions with distinct fiber directionality and dispersion properties. The posterior and anterior of the outer zone is labeled Region 1 and the remaining parts of the cervix (left and right of outer zone and all inner zones) are labeled Region 2 (Figure 3.11). For a NP cervix, Region 1 and Region 2 have different fiber dispersions between Regions and similar dispersions within each Region. However, when a NP cervix becomes a PG cervix, Region 1 will have a shift in the fiber dispersions so that the properties are similar to Region 2 while Region 2's properties do not shift. In other words, Region 1 is more sensitive to pregnancy status and remodels more dramatically than that happened in Region 2 during pregnancy. The arguments above are verified by ANOVA test in Result section by comparing Region 1 in NP with Region 2 in NP and all Regions in PG.

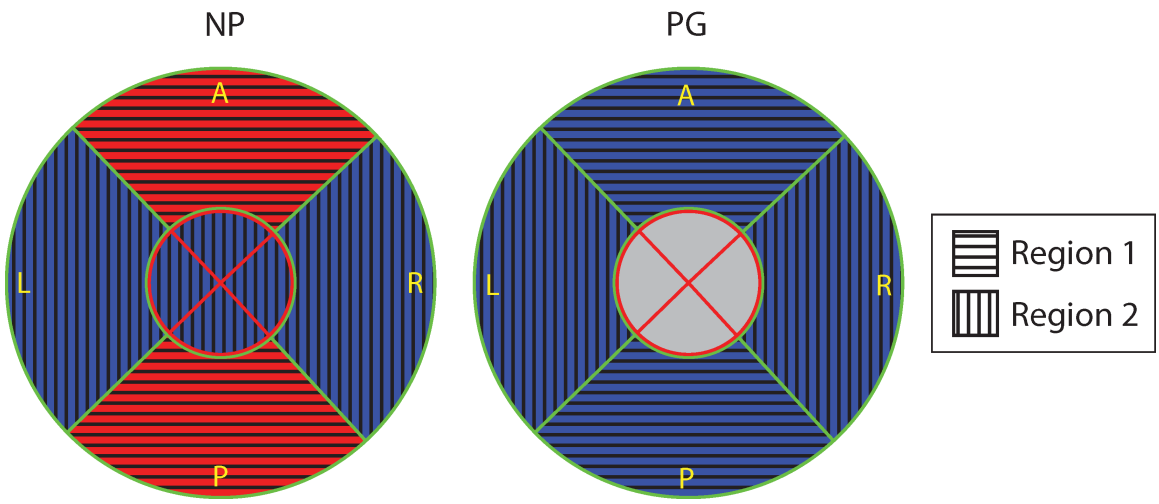

Figure 3.11. Definition of Region 1 and Region 2. The collagen fiber network in cervical tissue is not homogenous and it has two distinct regions: Region 1, the P/A quadrants in the outer radial zone (horizontal stripe), and Region 2, the rest (vertical stripe).

We believe the regional differences in collagen fiber properties within a single sample and between samples is influenced by the anatomical and loading environment of the cervix in the pelvic region. The cervix is the lower portion of uterus. The upper portion of the cervix, or the portio supravaginalis, lies above the vaginal attachment to the cervix. Cardinal ligaments attach this portion laterally (i.e. left and right), and the bladder lies anterior to the cervix separated by loose connective tissue. In pregnancy, the upper cervix is substantially loaded by the growing fetus [71]. The positioning, symmetry, and shape of the uterus and cervix drive the patterns of cervical stress and stretch and can be vastly different for each person [72]. Often in pregnancy the cervical axis is angled posteriorly from the uterine axis. This positioning leads to increased tissue loads and stretching in the anterior and posterior sections of the cervix [71]. The angle of the cervix with the uterus can be a potential cause of the increased anisotropy in Region 1 of the cervix, and the fact anatomical factors vary widely between patients can explain the variability between samples. Related research[4] of finite element analysis of human uterus and cervix also supports the heterogeneity of fiber dispersion we find between quadrants. The FEA analysis demonstrates that the collagen directionality and dispersion

play a role in resisting physiological relevant deformation during pregnancy. Further studies with larger patient populations must be conducted to understand the mechanical loads on the cervix and cervical tissue remodeling behaviors during pregnancy.

Many imaging modalities that have been used to study collagen fiber orientation and dispersion of hydrated soft tissues, with each method suited for different length scales and tissue sample preparations. Our OCT analysis presented here interrogates the tissue within 400 μm × 400 μm subregions across whole, hydrated, and unfixed axial tissue slices. In comparison, second-harmonic generation (SHG) microscopy is a standard method for the characterization of hydrated biological tissue at sub-cellular resolution. The field of view of SHG systems can be tens of microns to hundreds of microns, with a resolution of better than 2μm [73]. With these features, SHG captures information on fibril-level structure and the "crimping" or waviness of fibrils. Small angle light scattering (SALS) uses laser light to image fiber orientation and dispersion [74]. Collagen fibers can be distinguished from striated muscle, smooth muscle, and elastic fibers from the resulting angular distribution of scattered light because striated muscle, smooth muscle, and elastic fibers have different birefringence properties [75-77]. Each reading covers ~ 4 × 4 μm area which is the size of a single or small group of collagen fibers. In the future, functional extensions of OCT can also allow for interrogating the anisotropy and birefringence properties of cervical samples using polarization sensitive OCT [64].

We carefully compared our conclusion with a similar paper, [17], which used x-ray diffraction to study the collagen ultrastructure in human cervix. The study presents detailed cervical collagen orientation and dispersion data from NP human 1 mm^3 cube samples that have been scanned in three orthogonal directions. There are similarities and differences between this X-ray diffraction study and our OCT study. First, they found that near the internal os there are three zones of preferentially aligned collagen fibers - the inner zone, the middle zone, and the outer zone. The X-ray data found that the both inner and outer zone have longitudinally aligned fibers while the middle zone has circumferentially aligned fibers. Our study indicates a similar inner zone, but since we cut and scan axial slices it is not possible to see longitudinal fibers in our OCT images. It may be possible that the

radially aligned fibers seen in the OCT data are skewed longitudinal fibers that not perfectly aligned with the inner canal. The middle zone indicated in the X-ray study is similar to our outer radial zone of circumferential fibers. However, our OCT images show these circumferential fibers extend to the outer edge of the sample. They also measured the thickness of each zone, the inner and outer zones are 3-5 mm and the middle zone is 5-12 mm. The inner zone in our study ranges from 0 mm to 6 mm and the middle zone ranges from 6 mm to 14 mm, which is comparable to the results presented by them. Second, the fiber dispersion in [17] is much tighter than that in our study. In [17]'s finding, almost all the fiber are aligned within 90° while in our study there are always fibers throughout 180°. We believe reason for the difference lies in the difference of method including sample preparation (our samples were not fixed) and fiber recognition.

This research presented in this paper has the following limitations. First, as discussed earlier, the collagen fiber network is three-dimensional but fiber orientation and dispersion was only studied in two dimensions. Longitudinal fibers cannot be verified in this research because OCT images were stitched in the plane that is perpendicular to the inner canal. Second, only the available slice that is closest to the internal os had been studied. We selected the first slice to start our research because the internal os is the location of premature funneling [4] and maximum stress [71] during pregnancy. The premature funneling is often followed by opening up from the rest of the cervical inner canal and preterm birth. As we found in different quadrants, it is highly possible that the cervix is heterogeneous in the longitudinal direction since the percentage and type of biological and chemical components have been found to be different along longitudinal direction [13] and the inner zone was found to disappear as we approach to the external os [17]. Third, due to the limited number of consented patients, we have a smaller database comparing to research that uses animal tissue. Currently, our preliminary study on pregnant samples is based on 2 specimens. We plan to collect more specimens and draw a more conclusive comparison in our future study. Also, we will keep increasing the number within nulliparous, primiparous, and multiparous groups. Fourth, PG slices were not necessarily at the upper cervix because both of our PG samples were from patients with accreta and it is difficult to distinguish the location of the internal os. In order to avoid tissue with accreta, cervical slices of PG

patients were obtained at the most proximal location available so the slices could be from mid-cervix. Fifth, although our pixel-wise analysis can capture the patterns of multiple fiber families, the von-Mises based distribution fitting is not efficient for subregions with two dominant families. Since the only case (two families) that cannot be efficiently captured by von-Mises distribution accounts for about 5% of all subregions, von-Mises is a good distribution model overall. In the future, we will improve our method and develop a more generalized method for all fiber family patterns.

3.5 Conclusions

In this chapter, we measured the heterogeneity of local fiber orientation and dispersion in human tissue slices from the upper cervix using an OCT pixel-wise fiber orientation algorithm. We found that human cervical tissue has a distinct collagen fiber ultrastructure where collagen fiber orientation and dispersion vary according to anatomical quadrants. We found that in non-pregnant tissue, the anterior and posterior quadrants have highly aligned circumferential collagen fibers that are less dispersed than the left and right quadrant. Overall, we found that the non-pregnant samples examined here had more aligned and less dispersed collagen fibers than pregnant tissue, and that there was no difference in collagen properties between non-pregnant samples of different parity. The OCT imaging and tracking algorithm presented here is suited for our application because it offers tissue fiber ultrastructure characteristics at a length scale appropriate for implementation into a previously developed fiber-based continuum material model for human cervical tissue [4]. Additionally, the whole sample fiber maps inform the implementation of tissue architecture into large-scale finite element models of pregnancy. Lastly, OCT is a nondestructive technique, which allows for ultrastructural, biochemical, and mechanical analysis to be conducted on a single sample. In future work, multiple slices from internal os to external os will be analyzed to look for trend of fiber dispersion along longitudinal direction, mechanical tests will be conducted to determine corresponding material behavior, and the structural importance of the regional ultrastructural properties of the cervix will be explored in finite element models of human pregnancy. With the fiber orientation and dispersion information, we want to further perform mechanical tests on the same slices and see if the behavior

under mechanical loading can be predicted by using the fiber information and by fitting for other material parameters.

4 Anisotropic Material Characterization of Human Cervical Tissue using Optical Coherence Tomography and Mechanical Indentation

4.1 Introduction

The cervix is a dense fibrous tissue that is located at the lowest part of the uterus. It is cylindrical in shape with average dimensions of 3cm long and 2.5cm in diameter[1]. The mechanical function of the cervix is crucial for a healthy term pregnancy (defined as a pregnancy that extends beyond 37 weeks of gestation). Cervical mechanical function has two roles: 1) prior to term it must remain closed and resist the increasing mechanical load from the growing pregnancy and 2) at time of parturition it must soften, deform and dilate to 10cm to allow for delivery of the fetus. To accommodate this drastic dilation of the cervix at time of delivery, the extracellular matrix (ECM) of the tissue must drastically remodel, reorganize, and soften during gestation. The timing and characteristics of this remodeling behavior is currently an active research focus because it is hypothesized that premature remodeling in pregnancy can lead to a preterm birth [12], a leading cause of neonatal death or significant neonatal morbidity [78]. In an effort to characterize the compressive mechanical behavior of human cervical tissue, we present a novel indentation test with digital correlation imaging to visualize the real-time deformation of cervical slice during indentation and measure the compressive mechanical properties through coupled finite element analysis with collagen fiber orientation and dispersion information informed by OCT of non-pregnant and term pregnant cervical tissue.

The premature change in mechanical properties of the cervix induced by alterations of cervical tissue ECM content and ultrastructure is thought to contribute to cervical failure leading to preterm birth. Cervical collagen exists as fibers in a hierarchical network embedded in a viscous ground substance of negatively charged glycosaminoglycans (GAGs) and other proteins [12]. The collagen (types I and III) makes up 34 to 77% of the dry weight [13, 14], with evidence from human tissue studies showing that this dry weight content remains constant during gestation [15]. In general, the

collagen fiber network is reported to be anisotropic with different preferred orientations in distinct anatomical regions within the cervix [79].

The goal of performing a mechanical indentation test on the specimen that had been imaged by OCT is to solve for other material parameters of human cervical tissue with known fiber orientation and dispersion. This is motivated by a sensitivity test of material parameters in which the force was very sensitive to the Young's modulus and strains were very sensitive to Poisson's ratio and fiber concentration. Cervical slice has anisotropic material properties due to preferentially-aligned fibers but classic indentation can only record force versus time and displacement data. To gather information about anisotropy, a camera was set up to capture images of the speckled bottom surface of cervical slices throughout the indentation test. Here we report the anisotropic material properties for cervix using mechanical indentation test coupled with digital image correlation.

4.2 Methods

4.2.1 Sample preparation

Five human cervices were collected from consented hysterectomy patients by an IRB approved protocol at Columbia University Medical Center (Table 4.1, Figure 4.1). Among the cervices, 4 were from non-pregnant (NP) patients undergoing hysterectomy for benign indications and 1 were from pregnant (PG) patients undergoing cesarean hysterectomy due to abnormal placentation. Patient age ranges from 42 to 49 and parity number from 0 to 5. The cervices were sliced perpendicular to the inner canal immediately after hysterectomy using a custom-built slicer. The thickness of each slice was 2.60-5.97 mm. For some cervices we were able to test two slices and for other only one slice was available for mechanical test. The anatomical directionality was preserved by marking the anterior quadrant with dye right after cutting the cervix.

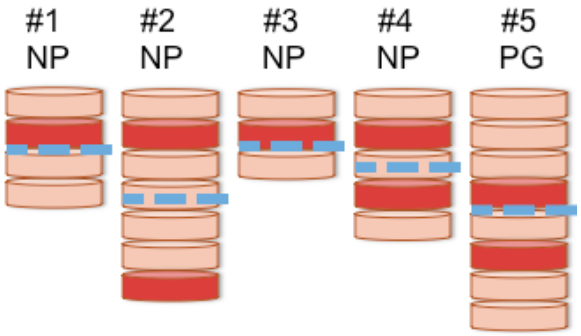

Figure 4.1. Number of slices of each cervix and slice(s) used for mechanical indentation test. Red slices were slices used for mechanical indentation and blue dash lines separate the upper cervix with the lower cervix.

Twelve hours before planned mechanical tests, each cervical slice was microtomed and equilibrated in phosphate buffered saline (PBS) at 4C. After equilibration, each slice was then weighed and measured. The bottom surface of the cervical slice specimen was dried by KimWipes and speckled by Verhoeff's elastic stain (VEG) by an air brusher (Harder & Steenbeck) with 0.2 mm tip (Figure 4.2).

In this study, we analyzed slices that are in different locations in the cervix. Slice is numbered from the one that was closest to the internal os. Slice 1 is the closest slice to the internal os. Depending on the dimension and integrity of each cervix, 3 to 8 slices were excised. For this study, all slice 2's were considered in the upper cervix since they are the closest slice we have access to and since for most cervices have more than 3 slices. Cervix 5's slice 4 was also considered from the upper cervix because Cervix 5 had 8 slices in total. All other slices, including slice 7 from Cervix 2, slice 4 from Cervix 4, and slice 6 from Cervix 5, were considered from lower cervix since they were from the lower 50% of the cervix. The distance of a specific slice to the internal os could be estimated by the slice thickness times the slice number. A more detailed protocol used for sample collection and preparation was described in our earlier work[79].

Specimen Number	Age	Pregnancy Status	Gravidity / Parity	Obstetric History	Total Slice Number	Slice Used	OCT Paper Reference
1	49	NP	0	n/a	4	2	
2	49	NP	1/1001	vd x1	7	2, 7	6
3	46	NP	3/3003	vd x1, c/s x1, vbac x1	3	2	11
4	42	NP	5/1041	vd x1, vtop x3	5	2, 4	1*
5	42	PG & CI	5/2022	lack information	8	4, 6	13**

Table 4.1. Patient demographics of specimens used for this study. CI = cervical insufficiency. Gravidity is equivalent to the total number of pregnancies. Parity data is presented in TPAL recording system. TPAL stands for term, preterm, aborted, and living deliveries, corresponding respectively to each of the 4 digits. vd = vaginal delivery, vtop= voluntary termination, c/s = cesarean section, vbac = vaginal birth after cesarean. The last column relates cervices with the specimen number in [79]. * Slice 1 was used in [79] which was not available for this study, ** Slice 2 was used in [79] which was not available for this study.

4.2.2 Mechanical indentation test

After speckling, each specimen was placed in a petri dish with glue applied to the outer boundary of the specimen to ensure specimen does not float (Figure 4.2A). The bath was put on the rig with an open glass window on the top to let light go through. The petri dish was then filled with Phosphate-buffered saline (PBS) and the specimen was equilibrated for at least half an hour at room temperature. The PBS bath was placed on the rigid surface of a universal testing machine (Microtester 5948, Instron Inc., Norwood, MA) equipped with a 6mm diameter stainless steel sphere indenter attached to the 5N load cell (Instron Inc., Norwood, MA, 0.25% accuracy of indicated load).

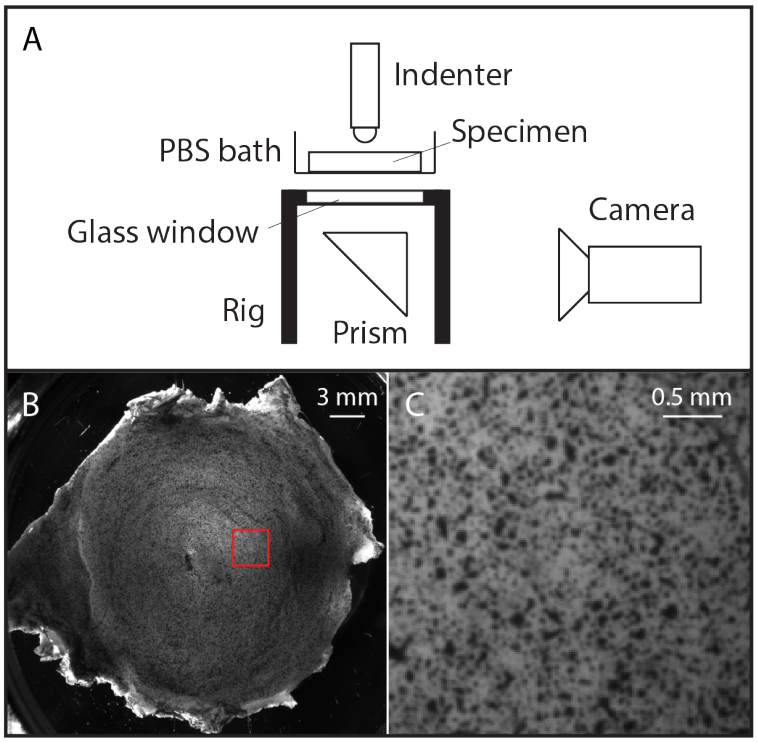

Figure 4.2. (A) Schematic illustration of indentation test with prism and camera setup (B) Representative bottom surface image and speckle pattern and (C) closer look at speckle patterns from the red box in (B)

Before each indentation test, the zero point for indentation contact was estimated by positioning the indenter tip just above the specimen surface and moving the tip down in 8μm increments until a change in load greater than 0.15mN for NP and 0.05mN for PG was observed. The indenter was then raised until it was out of contact with the specimen, and the force was zeroed. After this contact estimation procedure, the sample was allowed to recover for 1 minute.

Once the sample was allowed to recover, and with the indenter tip starting above the sample, a displacement-controlled, multi-level ramp-hold indentation test was conducted. There were a total of four ramp-hold levels with indentation depths determined by percentages of the specimen thickness at the indentation location. For thickness less than 5mm, the indentation depths were 15%, 30%, 45%, and 60% of the thickness, respectively. For thickness more than 5 mm, the indentation depths were

12.5%, 25%, 37.5%, and 50% of the thickness, respectively. The ramping rate was always 1% thickness per second. The hold times of were 480s, 600s, 720s, 960s for the four levels, respectively. Load–time (N-s) data were recorded using the material tester software (Blue Hill version 3.11.1209).

One indentation test was performed in the mid-stroma area (Figure 2.1) in the center of each quadrant (posterior, anterior, left, and right). The mid-stromal region was defined as the region apart from the fascia at the outer area and the mucosa around the inner canal.

4.2.3 Digital imaging correlation

To capture real-time deformation data of the specimen during indentation test, the bottom surface of the specimen was photographed (Figure 4.2) by a CCD camera (Point Grey, GRAS-50S5M-C) using the software Vic-Snap (Correlated Solutions, v2010). The lowest possible aperture that could produce high contrast images was used to maximize depth of view. The PBS bath was placed on a rig with a transparent window. Light was cast by a fiber optic illuminator (Cole-Parmer, Model 41500-50) from the top of the rig. A 90-degree prism was fixed below the window to image the bottom surface of the specimen from the front (Figure 4.2A). During ramps (as well as 2 seconds before and after), the acquisition rate was two images per second. During holds, the acquisition rate was one image per 10 seconds.

The images were processed for DIC by Vic-2D (Correlated Solutions, v2009.1.0) with incremental algorithm. In incremental correlation, each image is correlated with the previous image. The Area of Interest (AOI) was selected around the center of indentation. A subset size was selected for each specimen, between 29 and 59 pixels, depending on the speckle pattern such that, within each subset, there were enough unique features for correlation. Step size, which controls the spacing of points that are analyzed during correlation, was set to one quarter of the subset size as suggested by the software manual. A starting point was selected in area without much deformation so that the speckle pattern had been preserved throughout the experiments. After DIC, Lagrange strains in horizontal (e_x) and vertical (e_y) directions and shear strain (γ_{xy}) were extracted for the computer finite element model to fit.

4.2.4 Finite element geometry and meshing generation

Inverse Finite Element Analysis (IFEA) was used to find best-fit material parameters. For the Finite Element (FE) model, each specimen was represented as a half-disc with the corresponding specimen dimensions, and the indenter was represented as one-quarter of the 6mm sphere (Figure 4.3). The shape and dimensions of the specimen were simplified in the following way. The effective diameter of the inner canal was measured as *C* (Figure 4.4A). The closest distance from the indentation center (which was determined by the highest first principal strain in DIC color maps) and the inner canal boundary was measured as I. The closest distance from the indentation center and the effective outer boundary of the slice was measured as *O*. The FE reconstruction was based on the measurements of *C*, *I*, and *O* by assuming they were collinear (Figure 4.4B). The thickness of the indentation location was measured during indentation test using the indenter by measuring the distance between the bottom of the petri dish and the top surface of the specimen.

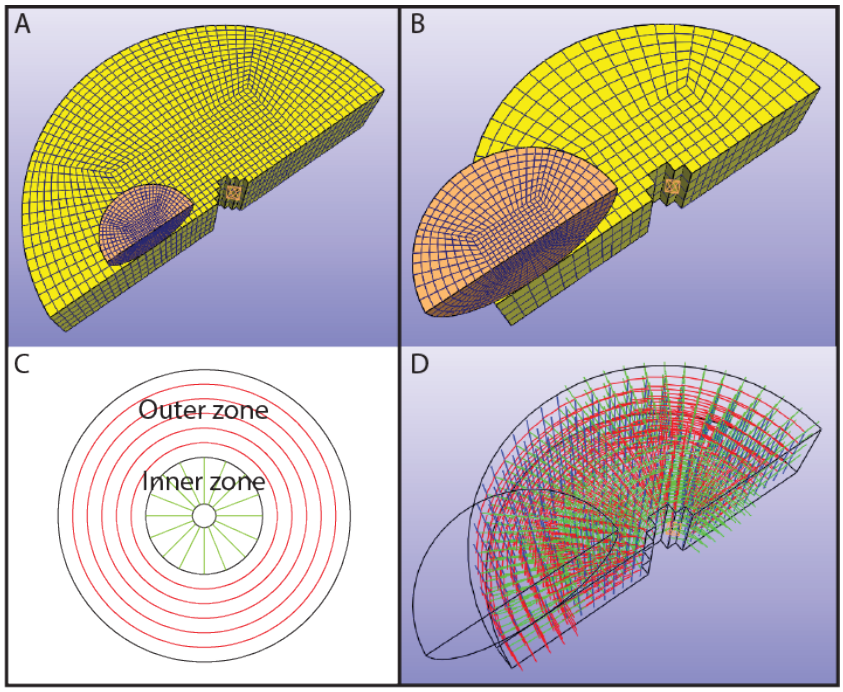

Figure 4.3. Meshes of the largest slice (A) and smallest slice (B). The local fibers are shown in (C) with red lines.

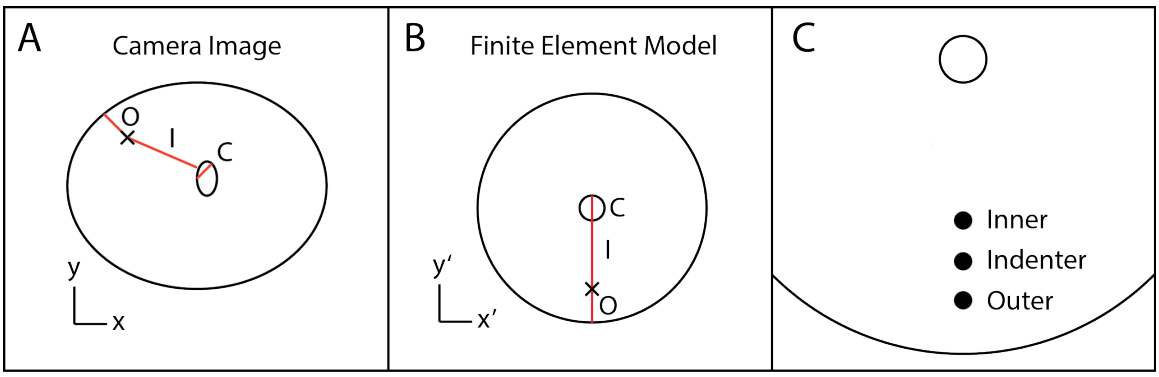

Figure 4.4. Finite element model simplification, coordinate system conversion, and parameter optimization locations. (A) *CIO* measurements in DIC coordinate system (B) simplified FE model from *CIO* measurements in the FE coordinate system (C) Locations selected for separate material parameter optimization.

The tissue slice was meshed in PreView (v1.18.2, www.febio.org) using hexahedron elements with butterfly center (Figure 4.3). In our analysis, the number of elements ranged from 1,146 to 8,028 depending on specimen dimensions. The size of the elements at the center of the top surface of the specimen was about 17% of the radius of the indenter.

4.2.5 Indenter location determination

To locate the indenter in camera images needed estimation. There are two methods used to locate the indenter in our study. The first method is to use the highest first principal strain. This is true with the assumption of indentation on an infinite half space but this can be inaccurate if the indenter is close to any glued boundary since the highest first principal strain can occur at the inner side of indentation because the glued tissue cannot deform (Figure 4.5). The second method is to use the outer boundary of the indenter rod to find the location of indentation. For some indentations, especially when the indenter was close to the glued region, the outer boundary of the indenter rod can be seen from the camera image (Figure 4.6), so the center of boundary circle can be defined as the location of indentation. For indentations, which did not have indentation rod outer boundaries, they were mainly indentations on larger cervical slice so the first methods can be used to accurately locate the indenter.

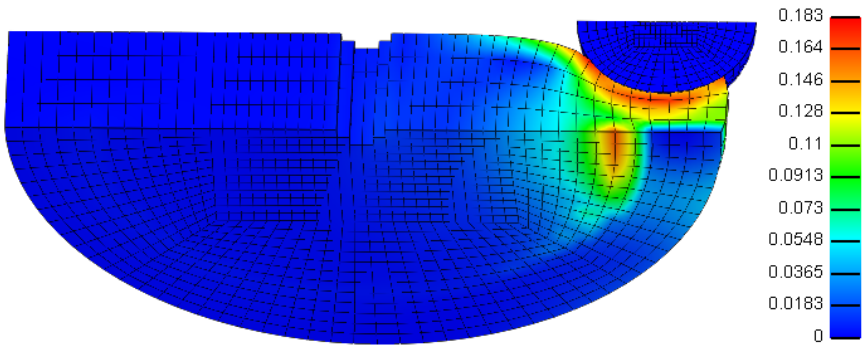

Figure 4.5. Highest first principal strain and indentation location mismatch when indentation location is on or close to glued boundary. On this illustrative FE model, the indenter was on glued region. The actually highest first principal strain is on the inner side of the indentation location. Note that no glued region was actually prescribed in any FE models.

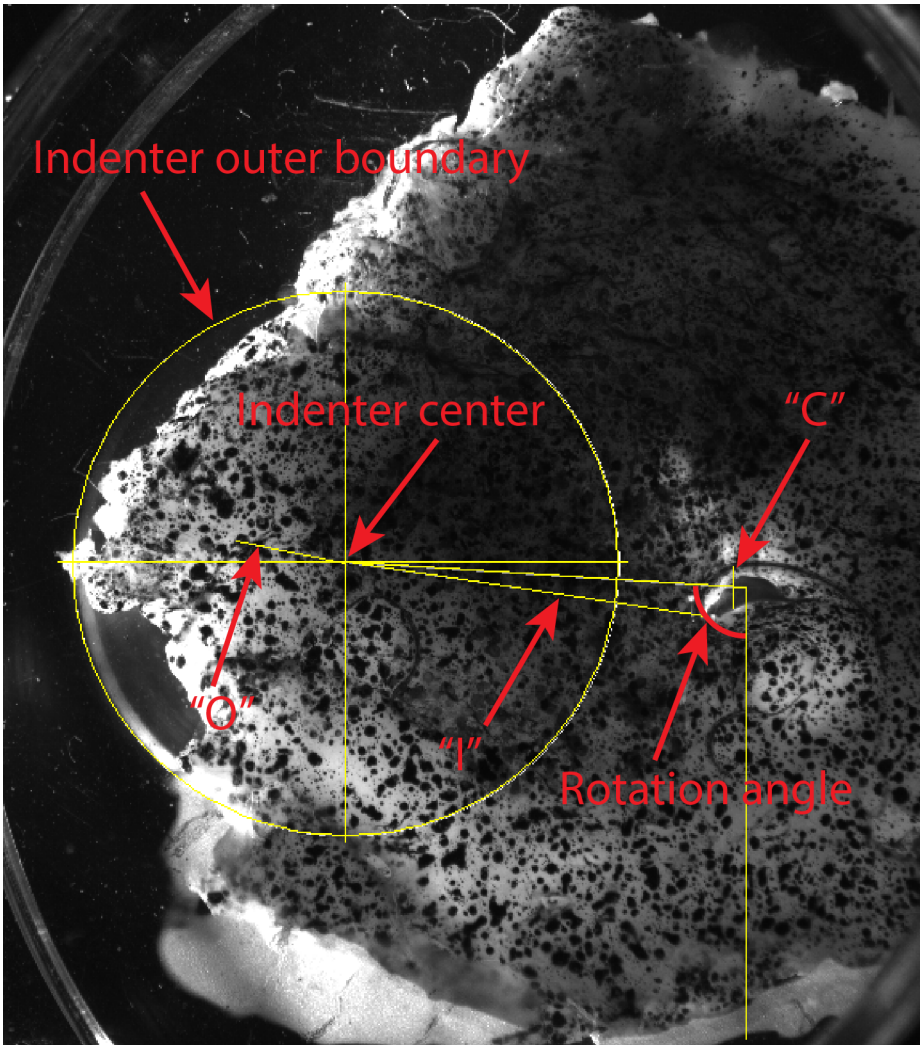

Figure 4.6. The indentation at the left quadrant of slice 4 of Cervix 5 is used for illustration of locating indenter through the outer boundary and *CIO* measurements with rotation angle measurement.

4.2.6 Constitutive model for cervical tissue

According to the components and arrangement of ECM, the fibers are distinct of others because they are tangled and they form a fiber network which could sustain stress. Other components including proteoglycan, elastin and ground substance are modeled together as a compressible matrix. Therefore, the total Helmholtz free energy density Ψ^{TOT} is the additive contribution from the fibrous

collagen network Ψ^{COL} and the neo-Hookean ground substance Ψ^{GS} of non-collagenous ECM components:

$$\Psi^{TOT}(\boldsymbol{F}, \widehat{\boldsymbol{a}}_o, b) = \Psi^{GS}(\boldsymbol{F}) + \Psi^{COL}(\boldsymbol{F}, \widehat{\boldsymbol{a}}_o, b) \tag{4.1}$$

Neo-Hookean ground substance

The strain energy function Ψ_{GS} is

$$\Psi_{GS} = \frac{\mu}{2}(I_1 - 3) - \mu \ln J + \frac{\lambda}{2}(\ln J)^2 \tag{4.2}$$

where μ and λ are the Lamé parameters, I_1 is the first invariant of left Cauchy-Green deformation tensor $\mathbf{B} = \mathbf{F} \cdot \mathbf{F}^{\mathrm{T}}$, and $J = \det \mathbf{F}$ is the relative volume.

According to standard relations of finite elasticity, Cauchy stress tensor is related to a strain energy density function having the form of $\psi(\mathrm{I}_1, \mathrm{I}_2, J)$ via

$$\mathbf{T}_{\mathrm{NH}} = \frac{2}{\mathrm{J}}\left[\left(\frac{\partial \Psi}{\partial \mathrm{I}_1} + \mathrm{I}_1 \frac{\partial \Psi}{\partial \mathrm{I}_2}\right)\mathbf{B} - \frac{\partial \Psi}{\partial \mathrm{I}_2}\mathbf{B}^2\right] + \frac{\partial \Psi}{\partial \mathrm{J}}\mathbf{I} \tag{4.3}$$

So the Cauchy stress tensor having strain energy function (ref3) is

$$\boldsymbol{T}_{NH} = \frac{\mu}{J}\boldsymbol{B} + \frac{1}{J}(\lambda \, ln \, J - \mu)\boldsymbol{I} \tag{4.4}$$

Fiber Network

The fiber network was modeled by power law material and 3D von-Mises fiber distribution. In this model, fibers can only support tensile loading. The radius of the inner zone was measured from the OCT image. The fiber direction was defined in radial direction within the inner zone radius and in circumferential direction outside the inner zone.

The von-Mises fiber distribution was described in Chapter 3.

The strain density function of a single fiber which obeys the power law is

$$\Psi_n^{COL}(I_n) = \frac{\xi}{\beta}(I_n - 1)^{\beta} \tag{4.5}$$

where ξ>0 and β≥2.

The free energy density of the solid collagen network Ψ^{COL} is an orientation average of the free energy density of a single collagen fiber Ψ^{COL} weighted by a 3D von-Mises distribution $D(n_o,b)$ and is given by

$$\Psi^{COL}(\boldsymbol{F}, \hat{\boldsymbol{a}}_o, b) = \int_0^{2\pi} \int_0^{\pi} H(I_n - 1)\, \Psi_n^{COL}(I_n) D(\boldsymbol{n}_o, b) sin\phi d\phi d\theta \quad (4.6)$$

Within the fiber part of the material, ξ is fitted, β=3 were set according to [4], and b was informed by OCT data. In the outer zone of P and A, b=0.3, while b=0.2 for the rest regions. The fiber orientation was set to circumferential in the outer zone and radial in the inner, according to earlier findings in OCT. The radius of the inner zone was measured from OCT en face images to ensure proportional inner/outer zones.

In summary, we have six material parameters E, v, b, ξ, β, and θ. The values of E, v, and ξ will be solved while the values of the rest were assigned.

4.2.7 Finite element material parameter optimization

The tissue was modeled as a fiber-incorporated composite material with compressible neo-Hookean as the ground substance and the indenter was treated as a rigid body. For FE calculations, clamped boundary conditions were placed on the outer boundary of the bottom surface of the tissue slice. Axisymmetric boundary conditions were applied on the x=0 plane of the tissue. Lastly, frictionless tension-compression contact (with tension turned off) with auto penalty was prescribed between the tissue and the indenter, with the indenter surface set as the “master” and the top surface of the tissue sample as the “slave”. Indenter-tissue friction was assumed to be negligible because the tissue was hydrated and thick [45]. Fiber directions were defined in the FE model according to OCT findings. For each indentation location, the corresponding OCT en face image was studied to find the radius of the inner zone, in which fibers were preferentially aligned in radial direction. Within that radius, fibers were defined in radial direction. Outside that radius, fibers were defined in circumferential direction (Figure 4.3CD).

To determine the material parameters for each indentation site, FE analysis was conducted for each indentation test in FEBio and a coupled optimization scheme were performed within MATLAB

(MathWorks, R2014b). The optimization scheme used a customized genetic algorithm (GA) to find the global best-fit model parameters μ=[*E, ξ, v*] that minimized the value of the objective function defined by

$$f(\mu) = \sum_{i=1}^{N}(w_F\left(F_i - \hat{F}_i(\mu)\right)^2 + w_e\left(e_{x,i} - \hat{e}_{x,i}(\mu)\right)^2 + w_e\left(e_{y,i} - \hat{e}_{y,i}(\mu)\right)^2 + w_e\left(e_{xy,i} - \hat{e}_{xy,i}(\mu)\right)^2) \quad (4.7)$$

where F_i is the equilibrium force on the indenter, e_x, e_y, γ_{xy} are axial Lagrange strains in *x* (circumferential) and *y* (radial) direction and shear Lagrange strain, respectively, *F* and *e*'s with circumflex are FE model predictions, *w*'s are weights for each measurements which equals a constant times the reciprocal of the maximum absolute value of the corresponding measurement (maximum *F* for force and first principal strain e_1 for strains) such that all measurements have the equal weight on the objective function.

The indentation location in DIC was located in by the circular center calculated from outer boundary of the indenter rod from camera image or highest first principal strain if the indenter rod was not visible. The three points for data fitting were selected from element right under the indenter (Figure 4.4C), one element on the outer side and one element on the inner side. The two side element were 1-2 mm away from the indentation location. The coordinate system conversion between FE model and DIC uses several steps. First, FE model was built according to *CIO* measurements and three elements were selected around the indenter. Second, the location of the indenter in DIC coordinates and the angle of the indenter from the inner canal were measured. Third, convert the coordinates of the three elements in FE model to DIC coordinates through indenter coordinates in both coordinate systems and the angle of the indenter in DIC coordinate system. Fourth, corresponding three locations were found and strain data were extracted from DIC. Fifth, all the strain data were rotated according to eqs. 4.2 and 4.3 and pre-processed for IFEA optimization use. The transformation (Figure 4.4AB) of strains between the coordinate systems of the FE model and DIC results were governed by

$$\epsilon_{x'} = \epsilon_x \cos^2\theta + \epsilon_y \sin^2\theta + \gamma_{xy} \sin\theta \cos\theta \quad (4.8)$$

$$\epsilon_{y'} = \epsilon_x \sin^2\theta + \epsilon_y \cos^2\theta + \gamma_{xy} \sin\theta \cos\theta \quad (4.9)$$

where θ is the rotation angle, e_x, e_y, γ_{xy} are the Lagrange strains in the original coordinate system, e_x' and e_y' are the Lagrange strains in the transformed coordinate system.

A genetic algorithm was implemented in Matlab to solve for the global optimum. The algorithm started with a population of four randomly generated in the search space. Search space is the lower and upper bounds for each parameter based on previous experimental set [4] and are given in Table 4.2. The exponential for fiber network was fixed as β=3. The concentration parameter b=0.3 for A/P quadrants for NP specimens and b=0.3 for L/R quadrants for NP and all quadrants for PG specimens. Each generation of GA had three steps [GA ref]: crossover, mutation, and selection. The process can be exhibited as below.

There are four individuals in generation i and each individual was one combination of material parameters:

$$p_1^i, p_2^i, p_3^i, p_4^i$$

$$p_j^i = (\log_{10} E\,, \log_{10} \xi\,, \nu) \tag{4.10}$$

In the crossover step, each parameter from a parent has 50% chance to be inherited to the next generation:

$$p_{j,k}^{i+1,co}{}_{l} = \begin{cases} p_{j_l}^i & 50\%\ possibility \\ p_{k_l}^i & 50\%\ possibility \end{cases} \tag{4.11}$$

In the mutation step, the parents' parameters were modified by a random value which obeys a normal distribution:

$$p_{j,k}^{i+1,mut} = p_{j,k}^{i+1,co} + w \circ \delta \circ \omega \tag{4.12}$$

where $\circ$ is the Hadamard product operator such that $(A \circ B)_{i,j} = A_{i,j}B_{i,j}$, $\omega = N(0,1^2)[1\ 1\ 1\ 1]$, $\delta = [\delta_{\log_{10} E}\ \ \delta_{\log_{10} \xi}\ \ \delta_b\ \ \delta_\nu]$, and $N(0,1^2)$ is a standard normal distribution and δ is a vector with elements representing the spreads of upper and lower bounds for all parameters, w is the mutation factor.

Among four parents, there are six children generated (all possible combinations). Ten individuals, including both parents and children, went through a tournament selection process in which individual with high fitness score (*f(μ)* in eq. 4.1) has higher chance to survive and exactly four individuals will survive and become parents for the next generation:

$$p_{1,2,3}^{i+1} = \text{tournament}(p_{j,k}^{i+1,mut}, p_1^i, p_2^i, p_3^i, p_4^i) \tag{4.13}$$

The tournament selection method is modified to fit our situation. The child with best fitness score will be chosen for the next generation. Starting from the second best child, their possibility to be chosen starts to decline and they possibility obey the following equation:

$$p_i = p \times (1-p)^{i-1} \tag{4.14}$$

A total of 40 generations was calculated. The initial mutation factor $w = 0.15$. When the fitness function does not improve for more than 5 generations, the mutation factor is divided by 1.3.

	Lower bound	Upper bound
E	0.1kPa	100kPa
ξ	0.1kPa	10MPa
v	0	0.499

Table 4.2. Search space for IFEA. Lower and upper bounds based on previous experiment set [4] and preliminary fitting results.

The GA in MATLAB was adjusted to facilitate cluster computing. One node (computer), 16 workers (cores), and 16 GB of memory were requested for each job. The population of four in each generation in GA was also selected partially because it provided best convergence performance while it would not use up memory requested from cluster computer. The for-loops in the MATLAB code were changed to parfor-loops to facilitate parallel computing on the cluster.

4.3 Results

4.3.1 Mechanical indentation test force response and bottom surface strain measurement

The indentation force response is generally higher for NP specimens comparing to PG specimens (Figure 4.7A). Force relaxation is observed during hold period and the relaxation is more significant at higher displacement levels. The average relaxation ratio ($F_{t=\infty}/F_{t=0}$) for the four levels are 58%, 45%, 28%, and 14% for NP specimens (n=24) and 58%, 46%, 31%, 17% for PG specimens (n=8). There is a non-linear relationship between force and indentation depth for both instantaneous and equilibrium states (Figure 4.7B).

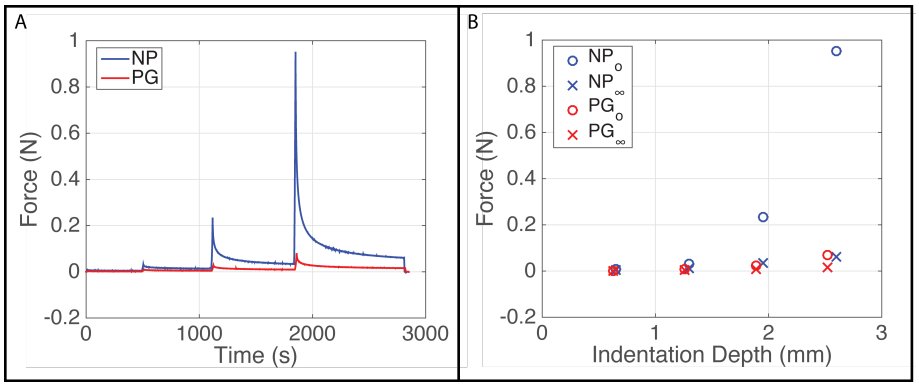

Figure 4.7. (A) Representative force-relaxation response to indentation for a NP (posterior of Cervix 1 slice 2, thickness of 5.35mm, maximum indentation depth of 2.60mm) and a PG (posterior of Cervix 5 slice 6, thickness of 4.03mm, maximum indentation depth of 2.52mm) cervical slice. (B) The instantaneous and equilibrium force plotted against four levels of indentation depths.

The 2D strain fields of the bottom of the sample show higher principal strains around the indentation spot and higher shear strains on both sides of the indentation spot (Figure 4.8). Strain relaxation is observed although the magnitude is much less compared with force relaxation. No more than 10% relaxation is observed (Figure 4.9). For some location and/or directions, the strain may increase during the hold period while the other direction relaxes (e_{yy} first level in Figure 4.9). In terms of strain magnitude, the axial strains (e_{xx} and e_{yy}) are much higher than the shear strain (γ_{xy}) on the

radius where the indentation spot was on. The shape of the contour maps for instantaneous and equilibrium strains are not different which indicates that the collagen fiber network does not re-align itself during the hold phase. There is a non-linear strain-displacement relationship between equilibrium strains and indentation depths (Figure 4.10).

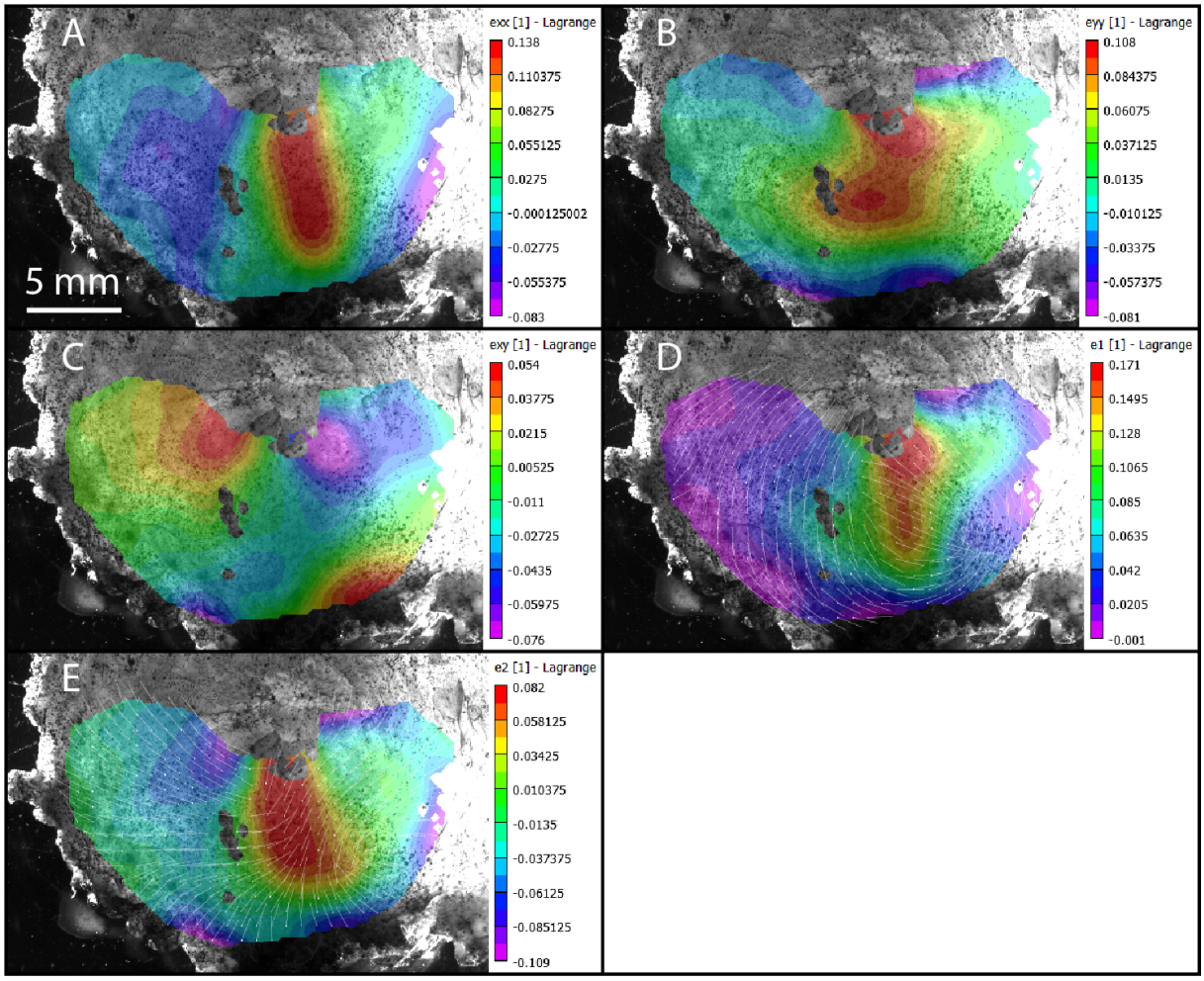

Figure 4.8. Strain color maps of the posterior region of a NP specimen which had good image correlation. (A) horizontal Lagrangian strain e_{xx} (B) vertical Lagrangian strain e_{yy} (C) shear Lagrangian strain γ_{xy} (D) first principal strain e_1 (E) second principal strain e_2

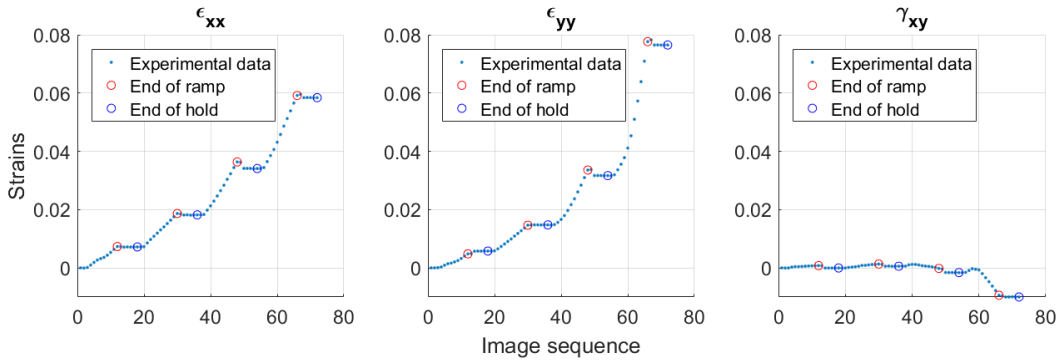

Figure 4.9. Representative strain responses to indentation for an indentation location in a NP specimen under the indenter. Images used for correlation is a subset of the original image sets to save computational time and reduce accumulative error.

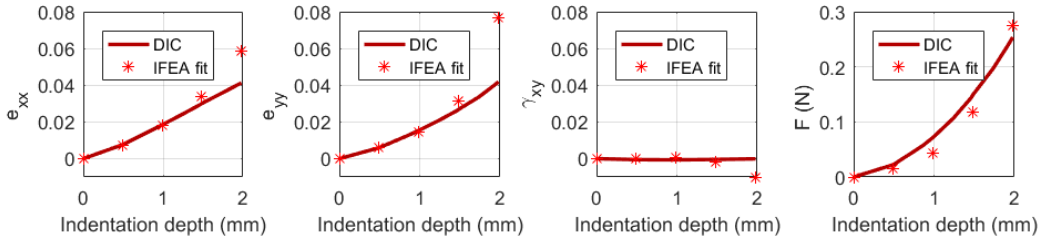

Figure 4.10. Equilibrium strains and force and IFEA fits of an indentation location in a NP specimen under the indenter. The fitted E=18.5 kPa, ξ=911 kPa, and v=0. The fitness of this example is average among all fittings.

4.3.2 Material parameter optimization

All GA optimization converged. Some fits show a very good consistency in terms of strain contour pattern (Figure 4.11).

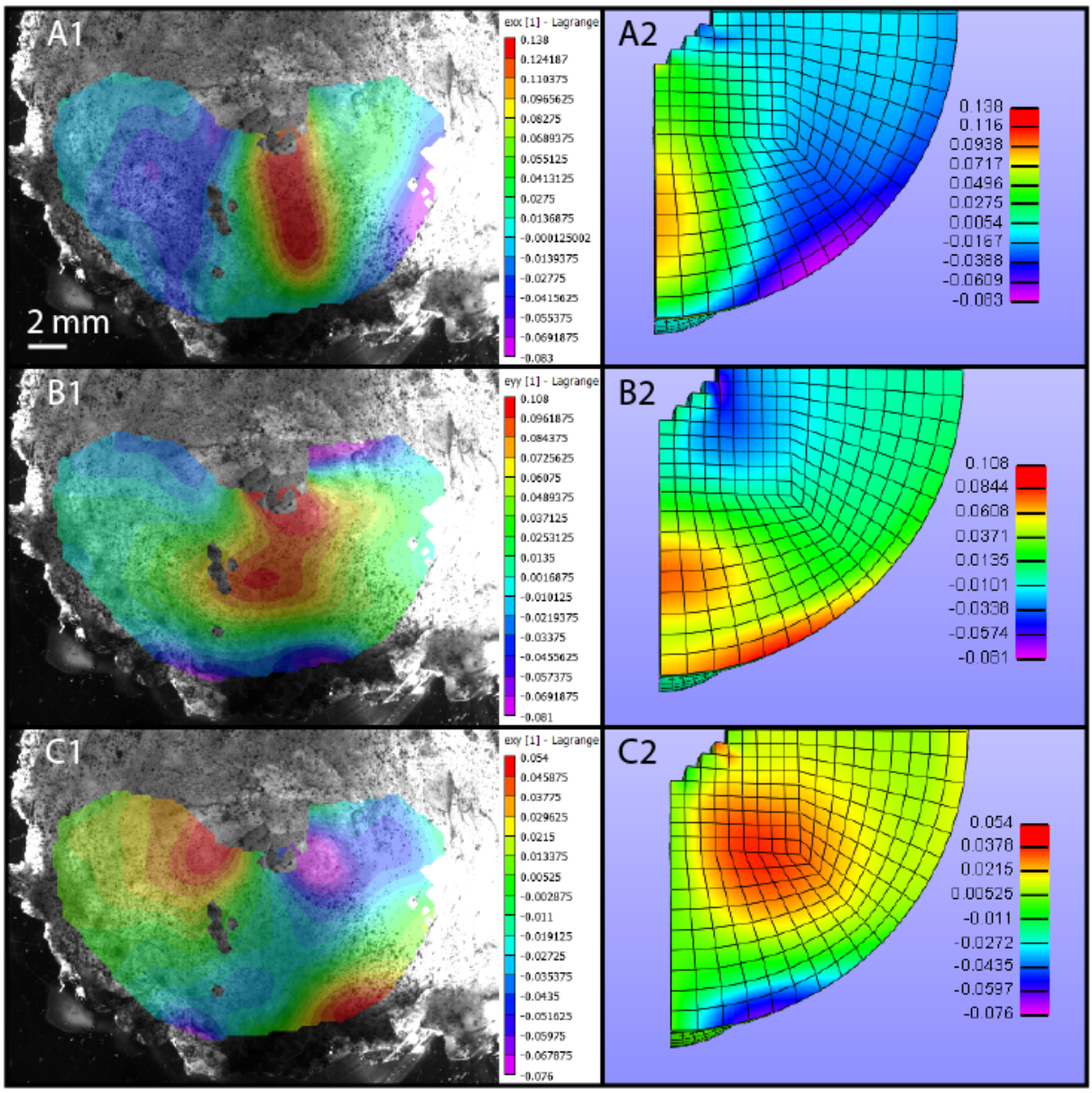

Figure 4.11. Comparisons of strain contour maps from DIC (1) and IFEA (2) optimization. (A) horizontal Lagrangian strain e_{xx} (B) vertical Lagrangian strain e_{yy} (C) shear Lagrangian strain γ_{xy}

4.3.3 Material parameters difference along axial direction

Among all slices, Cervix 2 and Cervix 4 have two slices with good IFEA fitting results so they were used for comparison in the axial direction (Figure 4.12).

Young's modulus is the only parameter that exhibited a difference between the upper slice and the lower slice. The slice that is closer to the internal os (upper) have a higher Young's modulus than the slice closer to the external os (lower). For Cervix 2, the slice 2's average Young's modulus is 4.3kPa while the number for slice 7 is 2.5kPa. The difference is marginal significant ($p=0.058$). For Cervix 4, slice 2's average Young's modulus is 10.7kPa while the number for slice 4 is 2.3kPa. The difference is significant ($p=0.026$).

Fiber modulus does not seem to change in axial direction for the two cervices. For Cervix 2, the fiber modulus for slice 2 and 7 are 260kPa and 362kPa ($p=0.73$), respectively. For Cervix 4, the fiber modulus for slice 2 and 4 are 2.4MPa and 9.7kPa, respectively. Although the average values are different by two magnitude, the difference is not significant due to high variance ($p=0.17$).

There is no difference for Poisson's ratio either. The Poisson's ratio is 0.15 and 0.24 for the two slices in Cervix 2 and the difference is not significant ($p=0.49$). The Poisson's ratio are 0.17 and 0.26 for the two slices in Cervix 4 and the difference is not significant ($p=0.89$) neither.

Three material parameters are further compared in a broader subset of the database (Figure 4.13). All NP upper slices (slice 2's) are compared with all NP lower slices (slice 4+'s). Again, Young's modulus is marginally higher in the upper slices ($p=0.063$), 5.6kPa in the upper slices opposing to 2.4kPa in the lower slices.

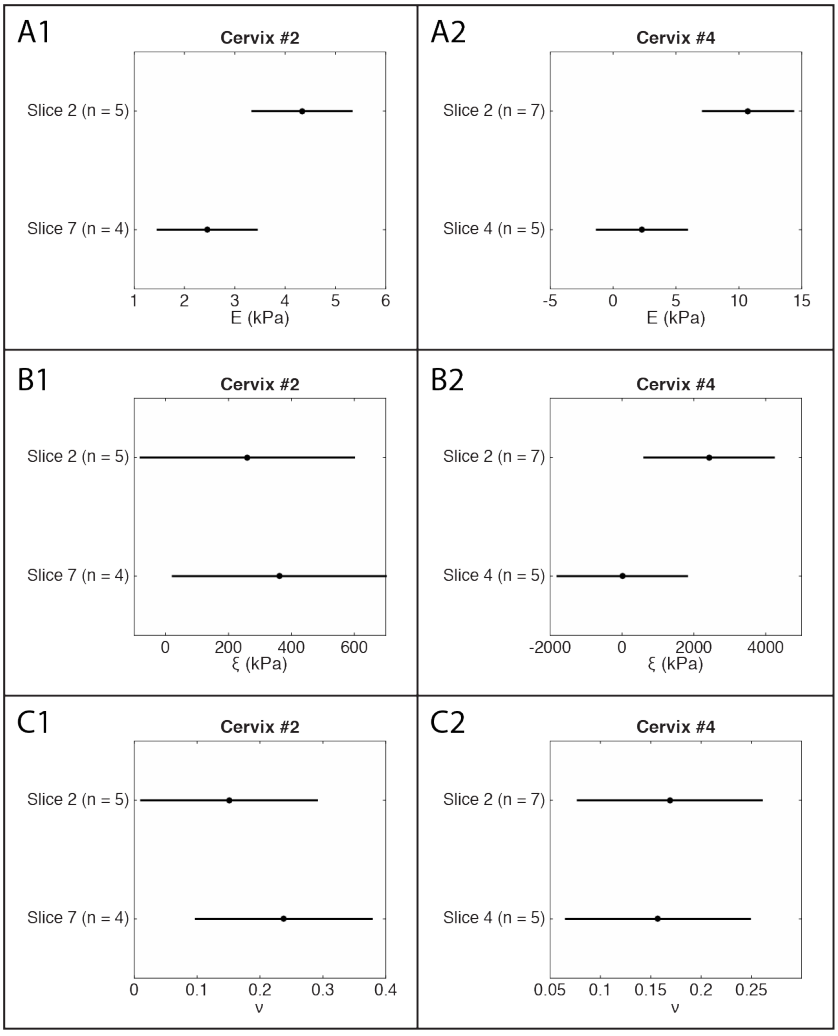

Figure 4.12. Material parameters comparison in axial direction for Cervix 2 and Cervix 4. “n” represent number of fitting locations.

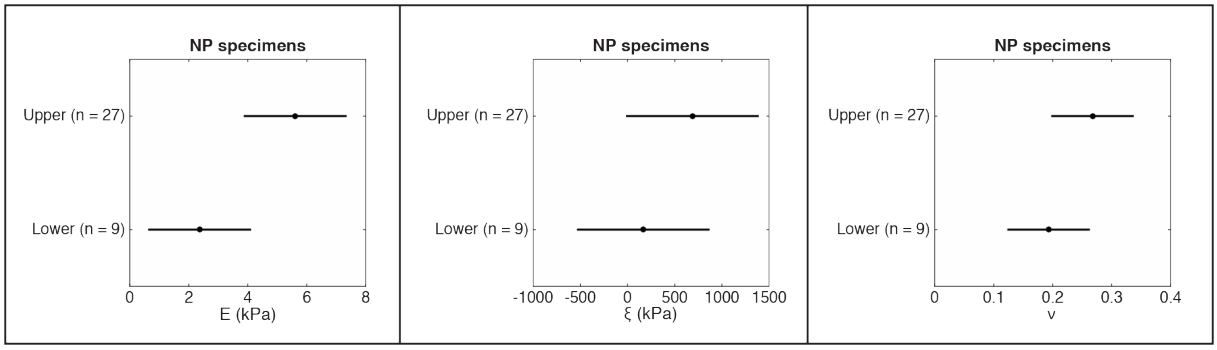

Figure 4.13. Material parameters comparison in axial direction between NP slices from the upper cervix and the lower cervix.

4.3.4 Material parameter difference among quadrants

For NP cervices, there is no indication that Young's modulus or fiber modulus was different in different quadrants, according to our database (Figure 4.14). Poisson's ratio is higher in A/P quadrants comparing with L/R. According findings in OCT, A/P are grouped together and compared with L/R combined since each group has similar fiber dispersion patterns.

The Young's modulus is similar for A/P and L/R quadrants, 4.9kPa and 4.6kPa, respectively. The fiber modulus in the A/P quadrants, 236kPa, was lower than that in L/R quadrants, which is 1,006kPa, but the difference is not significant ($p=0.20$). The Poisson's ratio in A/P quadrants is 0.30 on average, comparing to 0.18 in L/R quadrants, and the difference is significant ($p=0.032$).

Further investigation with Young's modulus found that there is a quadrant-wise difference in lower slices (Figure 4.15). In lower slices, the A/P quadrants have a weaker ($p=0.014$) ground substance, represented by Young's modulus of 1.2kPa, comparing to 3.0kPa in the L/R quadrants. However, in the upper slices, the difference is not found ($p=0.96$).

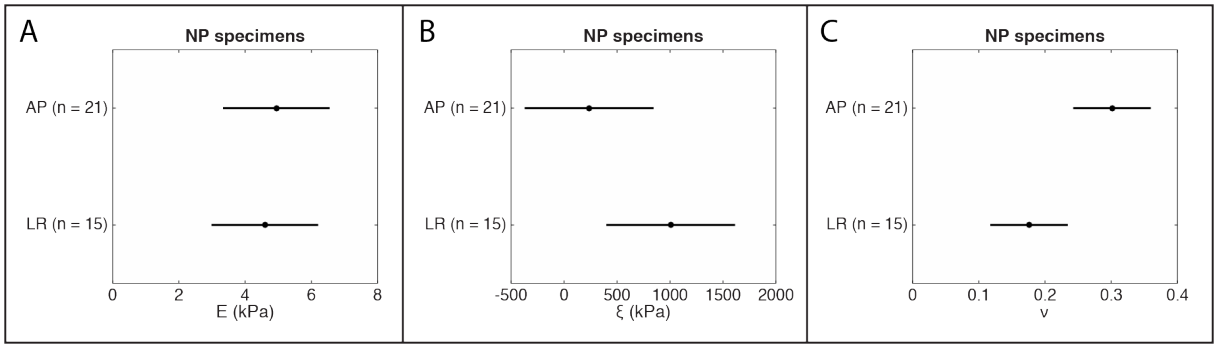

Figure 4.14. Material parameters comparison among quadrants (A/P vs. L/R) for all NP specimens.

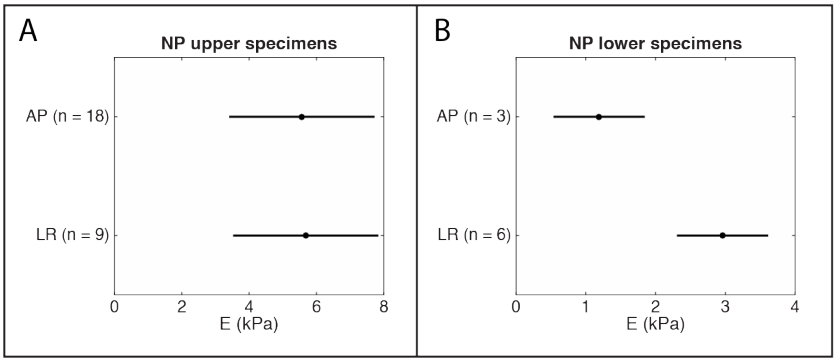

Figure 4.15. Young's modulus comparison among quadrants (A/P vs. L/R) for NP specimens in the upper cervcies and lower cervices.

4.3.5 Material parameters difference along radial direction

In radial direction, the fibers have a higher modulus in the outer point but the ground substance strength is comparable in all radial locations (Figure 4.16, $p>0.73$). For NP specimens, the outer point has a significant higher fiber modulus ($p<0.05$). The different between the outer point and the indenter location is also marginal significant ($p=0.069$). This pattern happens in AP quadrants as well as LR quadrants ($p<0.05$ between outer and inner points, $0.05<p<0.06$ between outer and indenter points). The inner point and the indenter point have no different ($p=0.96$) in fiber modulus.

The inner location has a lower Poisson's ratio comparing to the indenter and outer location for NP specimens ($p<0.05$). If we look at cervical slices in the upper cervix (slice 2's), this result still holds

(p<0.05). However, in the lower cervix, all three locations have comparable Poisson's ratio (p>0.51). The Poisson's ratio can be affected by collagen fiber network and other components in the tissue. The inner zone is known to have different fiber orientation and dispersion and it has mucosa glands around the inner canal. These can be the reasons why it has a different Poisson's ratio in upper cervix.

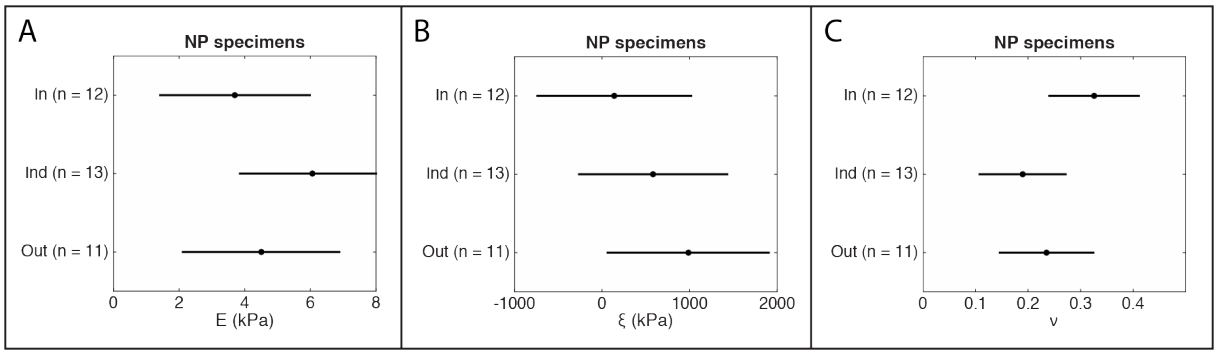

Figure 4.16. Material parameters comparison in radial direction (inner point, indenter point, and outer point) for all NP specimens.

4.3.6 Material parameters difference between NP and PG specimens

The only slice that have good IFEA fitting was Cervix 5 slice 4 so it is used to represent PG specimens. Since it was from the upper cervix, it was compared with NP slices from upper cervix and lower cervix separately. From the comparison, both Young's modulus and fiber modulus are different between NP and PG cervices (Figure 4.17). NP specimens from upper cervix have a higher Young's modulus (5.6kPa) than PG specimens (0.40kPa) and the difference is significant (p=0.020). The NP specimens from lower cervix have a higher Young's modulus (2.4kPa) but the difference is not significant (p=0.63). Both NP specimens from the upper (688kPa) and lower (166kPa) cervix have a lower fiber modulus than PG (3.7MPa) specimens and the differences are significant (p=0.023 and p=0.023, respectively). Both NP specimens from the upper (0.18) and lower (0.17) cervix have a lower Poisson's ratio than PG (0.10) specimens but neither difference is significant (p=0.67 and p=0.27, respectively).

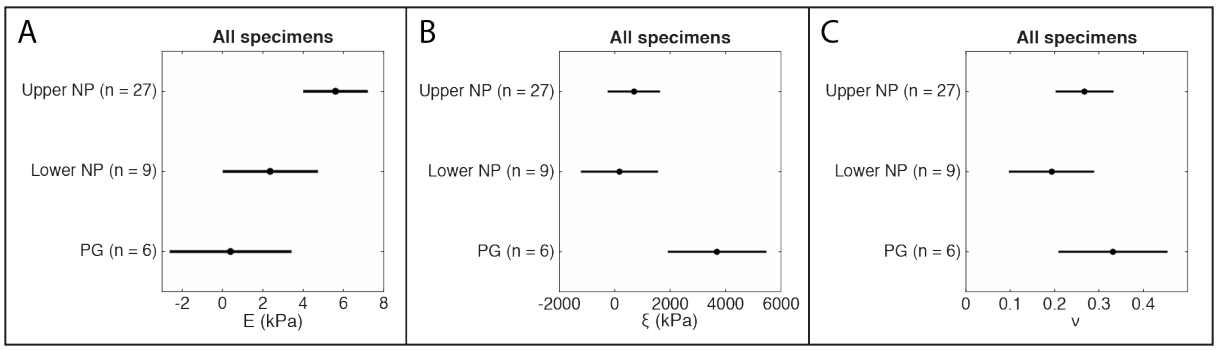

Figure 4.17. Material parameters comparison in between NP specimens (slices from upper cervix and lower cervix) and PG specimens.

4.4 Discussions

4.4.1 Verification of GA

Although there are toolboxes of GA to use in different software environments, a customized GA was coded in MATLAB to keep greater control of the process. The mutation process is a key process since it will affect whether the process is going to converge to a global optimum, and how fast it converges to global optimum. The parameter to tune the mutation process is the mutation factor. When this factor is large, there is more randomness in each generation, which indicates a better chance to fall into global optimum but at the same time slows the convergence speed. When this factor is small, convergence is quick, but it might fall into a local optimum since the variance is too small. Many values are tested and a starting mutation factor of 0.15 was selected and the factor decreases as the process moves to the final solution.

To verify that the GA is able to find global optimum, indentation at posterior quadrant of slice 2 of Cervix 1 was used to manually find the global solution.

The parameter space [E, ξ, v] was meshed into a 30x40x10 discrete space and on each dimension all possible values were selected. A total of 12,000 forward FEA's were conducted, and the results were plotted to visualize local optimums and the global optimum (Figure 4.18). We were able to

verify that our GA found the correct global optimum. The optimum GA found was [E=1.8kPa, ξ=120kPa, v=0.40]. In the validation test, best material parameters were [E=1.0kPa, ξ=129kPa, v=0.45] and the second best set of parameters were [E=1.8kPa, ξ=107kPa, v=0.40]. Since our search space was discrete, we believe the actual optimum was between the best and second best sets of parameters and the GA was able to find this region. There was no local optimum within the [E=1.0-1.8kPa, ξ=107-129kPa, v=0.40-0.45] so our GA would not have stopped at a local optimum.

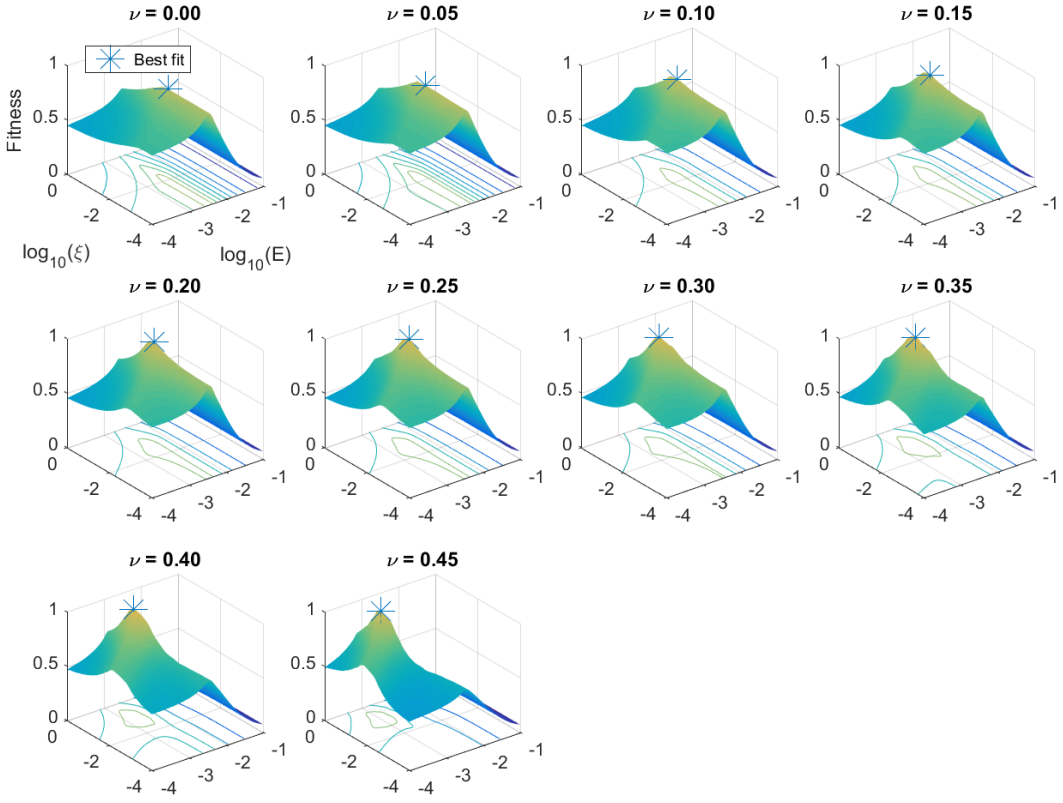

Figure 4.18. Verification of GA. Each sub-plot represents a Poisson's ratio, from 0 to 0.45, with 0.05 increments. Within each sub-plot, the x- and y-axis are the logarithm of Young's modulus and fiber modulus. The height at each (x, y) pair is the normalized fitness function where 1 means best fit and 0 means worst fit. The best fit within each Poisson's ratio value is depicted.

4.4.2 Compromising computational time and accuracy

Since optimization takes 40 generations to finish, and for each iteration there are 6 children FEA to run, the computational time is an important issue to this study. To save computational time, there are several possible solutions: (1) optimize the number of iterations and mutation factor; (2) use coarser mesh; and (3) use a lower penalty faction for FE contact.

Since GA involves randomness, a sufficient number of generations are needed to get confident results. According to experience, the mutation factor will have an important role on whether or not global solution can be reached, and on the number of generations needed to reach the global solution. A large mutation factor will guarantee that the model is flexible and random enough to reach far enough from local optimums. The disadvantage would be prolonged time needed for convergence to global solution. A small mutation factor will bring relatively stable convergence, but it might not be able to find the global optimum. Accordingly, we decided to start with a higher mutation factor and go lower if the results do not improve over certain generations. We are confident that the GA has enough generations to explore the whole space and get rough locations of the potential global optimums. When the mutation factor becomes smaller and smaller, the algorithm focuses on local searching instead, and converges to the global optimum relatively quickly.

Using coarser mesh will decrease the computational time by a significant amount while compromising the precision of the FEA. A validation is needed for the fineness of mesh needed for our model (Figure 4.19). In addition to our current model, in which the volume of each element is about 0.27mm^3, with total of 2,268 elements for a cervical slice, we also made a coarser mesh and a finer mesh for the same indentation. The coarser mesh's element is exactly twice as large in each dimension than the original one (element size of 2.16mm^3 and 281 elements in total) and the finer mesh's element is exactly half as large in each dimension than the original one (element size of 0.03mm^3, and 18,215 elements in total). The same material parameters were assigned to all three models. Strains in multiple locations at the bottom surface and force data on the indenter were examined and compared among three models. The strain at the bottom surface right under the indenter and reactive force are shown in Figure 4.20. There is a 12% difference in strains on average

and a 3.4% difference in force between the coarser mesh and the regular mesh. The difference between the regular mesh and the finer mesh is only 4% and 2.2%, respectively. We can observe the obvious improvement from the coarser mesh to the regular mesh but the improvement by further refining the mesh was not so significant. The computation times of the three models using a four-core PC were 5 seconds, 40 seconds, and 473 seconds. If we take computational time into consideration, the regular mesh would be a good balance as it allows relatively accurate results with less time.

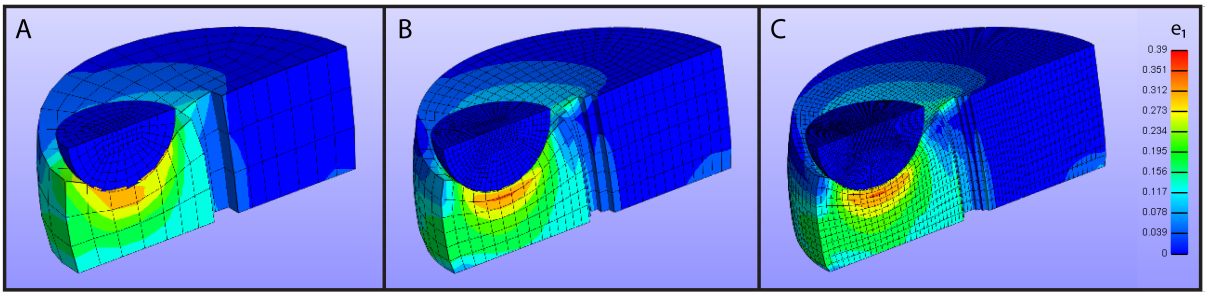

Figure 4.19. Comparison of the same geometry with different levels of mesh fineness. (A) Coarse mesh (B) Regular mesh used for IFEA (C) fine mesh

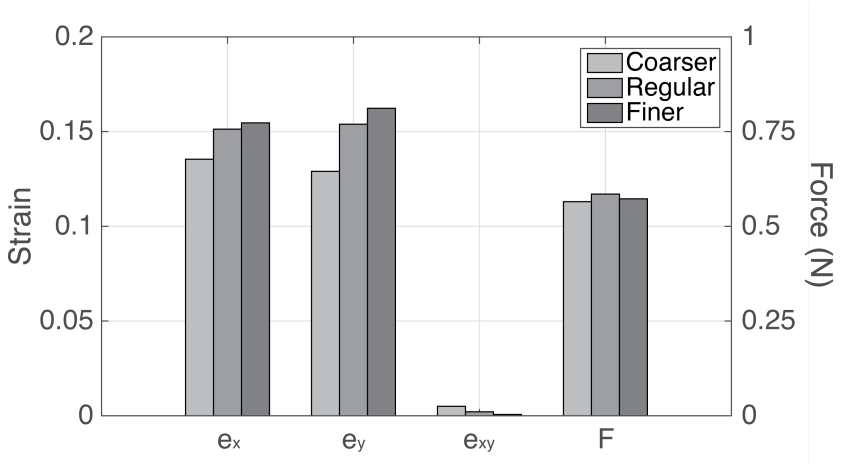

Figure 4.20. The strain and force responses of same indentation profile and material parameters from different meshes.

The penalty factor will affect the precision of the FEA as well since it penalizes the penetration between surfaces by a traction force. Although augmented Lagrangian method was used, the penalty factor still plays a similar role to scale the Lagrange multiplier increment. A high penalty factor will result in FEA results with less penetration and more precise results but it leads to longer convergence time, or even no convergence. We use a penalty factor of 2, which is a good balance between convergence and precision (penetration always less than 0.1 mm).

4.4.3 Mesh element type selection

A variety of mesh element types were tried before the 8-node hexahedron element type was selected. 4-node tetrahedron mesh was first used for preliminary IFEA because it has the advantage of easy meshing and quick convergence. Then all meshes were converted from tet4 to tet10 to add lateral integration points. 4-node tetrahedron mesh was not recommended for FEA because it has mesh lock issue when Poisson's ratio is high. 10-node tetrahedron mesh resolves that issue at the price of significantly increasing the computational time by around five times.

All tetrahedron meshes have the same issue with the current set-up of experiments and data analysis, which is the center of mass issue. In FE model, we were trying to find the same location, represented by the center of a FE element, in the FE model and in the camera image. However, the center of mass of a tetrahedron element, which is the center of mass in 3D, might not be the center of mass of its bottom surface, which is the center of mass in 2D. That means we could be pair different locations in FE and DIC and it can bring in error. Hex meshes generated in FEBio would solve this issue since the 3D center of mass is at the center of the bottom surface of the same element since each element has the same cross-sectional area in the vertical direction.

4.4.4 Difficulties in correlating DIC with FE and potential solutions that have been experimented

Displacement-strain nonlinearity and material selection

The material parameter fitting provided a general trend of the strengths of the ground substance and the fiber network as well as the compressibility of the tissue. However, for many strain

fittings, the curve shape was not fitted well. The data from the actual indentation showed a more nonlinear strain versus indentation depth curve. Although certain material models have stress-strain nonlinearity characteristics, they cannot solve the problem of displacement-strain nonlinearity. In the study, many combinations of material models for the ground substance (neo-Hookean, Mooney-Rivlin, Odgen) and the fiber network (exponential power law, neo-Hookean, toe-linear) were tested, and none of them could solve the nonlinearity issue. The possible reason for this could be friction. Friction was observed in some indentation where only a small region of the whole slice deformed while the rest stuck to the petri dish. For the remaining indentations where the whole slice deformed, friction could still be an issue to bring in error.

High friction cases and special geometries

For certain indentations, the specimens stuck to the petri dish, and the majority of the slice didn't deform during indentation (Figure 4.21A). The possible cause of high friction cases is drying the specimen for a long time after speckling, such that the bottom surface was no longer wet. Since only the region directly under the indenter was deforming, the original way to build the geometry would not work for this situation. For these cases, a circular model was built to represent a portion of the whole slice. Different from the original geometry, this is not a symmetric geometry, so the whole circular slice was modeled. The center of the bottom surface was free to move but the outer zone was fixed to represent the non-deforming surrounding tissue (Figure 4.21B).

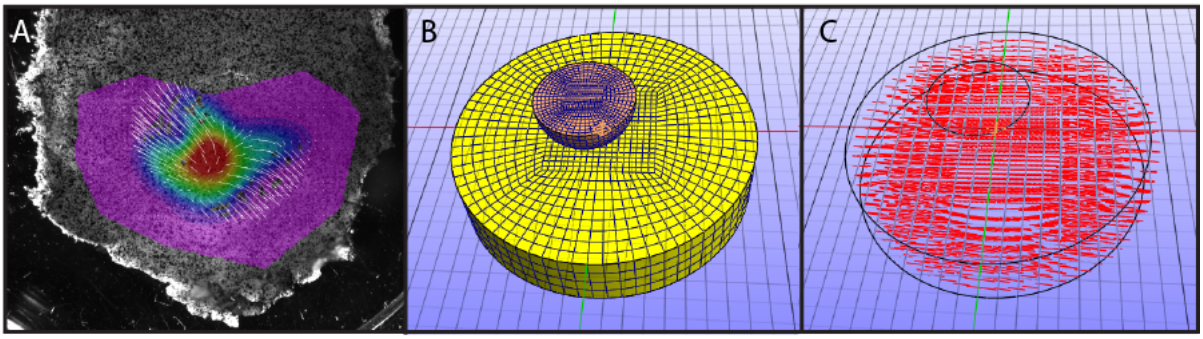

Figure 4.21. High friction case and corresponding solution. (A) high friction indentation with displacement shown in white arrows (500% magnification). Only regions around the indenter were deforming and displacement suddenly decreases to zero within a short distance. (B) A small circular model representing the deformable region and surround non-deforming region. (B) identical fiber orientation was used assuming the area is relatively small so that fiber orientation change within the region was small.

Complicated boundary condition and local tissue textures

The simplification from real geometry to uniformed FE model described in the Methods section would not suffice for all indentations. Sometimes the actual geometries were hard to be modeled by a circular slice because of the complicated physical boundary and glue boundary. Sometimes, the local tissue textures (could be fiber network or ground substance) were complicated and the ideal elliptical strain contours were not seen (Figure 4.22).

To test if the circular slice FE model can be improved by using more accurate geometry, real geometries were built for two indentations from Cervix 1 (Figure 4.23). A raster-to-vector conversion software Img2CAD (http://www.img2cad.com/) was used to vectorize camera image to actual slice boundary and to depict glue boundary from displacement contour map. The thickness was still identical for the whole slice. The tissue slice was meshed in Trelis (csimsoft, v16.1) using 2nd-order 10-node tetrahedron elements with refinement such that the area in contact with the indenter had finer meshing. The IFEA results were compared with regular circular slice but the results were not

significantly improved (fitness function improved by less than 10%). So we believe the difficulty with IFEA might be from the complicated local texture which cannot be easily addressed.

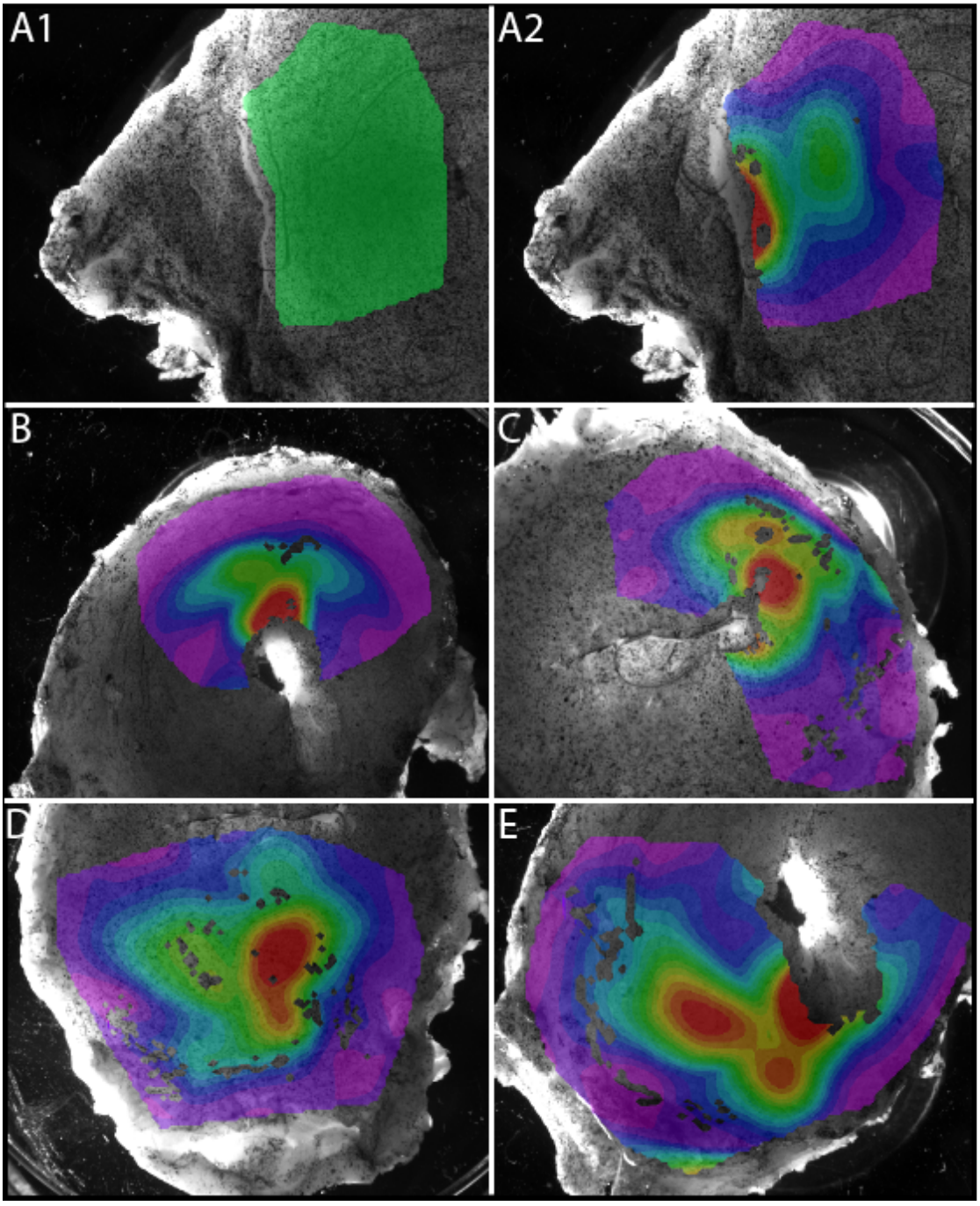

Figure 4.22. Illustration of IFEA difficulties caused by complicated boundary conditions and local tissue textures. First principal strains of five different indentation DIC results are shown. In ABC, complicated boundary conditions make the highest e_1 to happen in areas away from the indenter. In DE, local tissue textures make the contour map non-ideal showing non-elliptical contours.

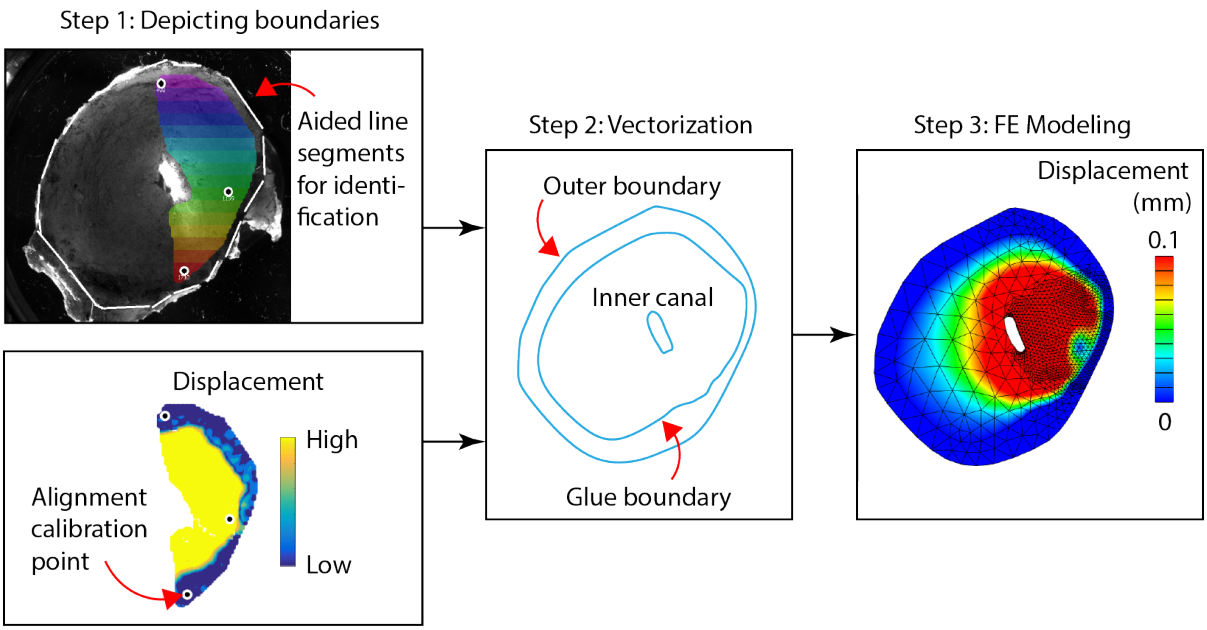

Figure 4.23. Strategy to use real geometry and glue boundary to solve complicated boundary condition issue. (A) Camera image with aided line segments for physical boundary identification. (B) Displacement contour map for glue boundary identification. (C) Overlaid physical boundary, glue boundary, and inner canal. (D) Displacement contour map of the bottom surface of FE model generated from real boundary conditions showing zero displacement between the glue boundary and the physical boundary.

4.4.5 The definition of fitting error

There are different ways to define fitting error, especially for the power term on the error of each measurement. The most common error definitions are mean squared error (MSE) and mean absolute error (MAE). The general form of these errors for a simplified one measurement fit can be expressed as:

$$Error = \sum_i |x_i - \hat{x}_i|^p \tag{4.15}$$

where x_i is the measured value and $\hat{x}_i$ is fitted value at strain level i. When p=1, the error is MAE. When p=2, the error is MSE.

The ultimate goal of fitting is to get good prediction at all strain levels. Since the strain is higher at higher displacement levels, the latter terms have higher weight by the definition. If MSE is used, the effect of the last two levels will be dominating in the error and the effect of the first two levels will not affect the fitted curve much. Since we currently have the strain-displacement nonlinearity that we cannot successfully predict, only the last point (or last two points) can be successfully fitted if MSE was used. On the other side, if we use MAE, more weights are given to the first three levels and a better balance can be achieved among four levels. We decided to use MAE since it will give our better fits at lower strain levels. We wanted to have good fits at lower strain levels first before considering modifying the material model to predict mechanical behavior at higher strains.

A comparison of the same indentation IFEA using two different error definitions is shown in Figure 4.24 and Figure 4.25. Both methods show good fit for force. For strains in *x* and *y* directions, MSE has better fits at the last strain level at the price of worse fits at lower strain levels. MAE, on the other hand, has better fits at lower strain levels but missed the highest strain level.

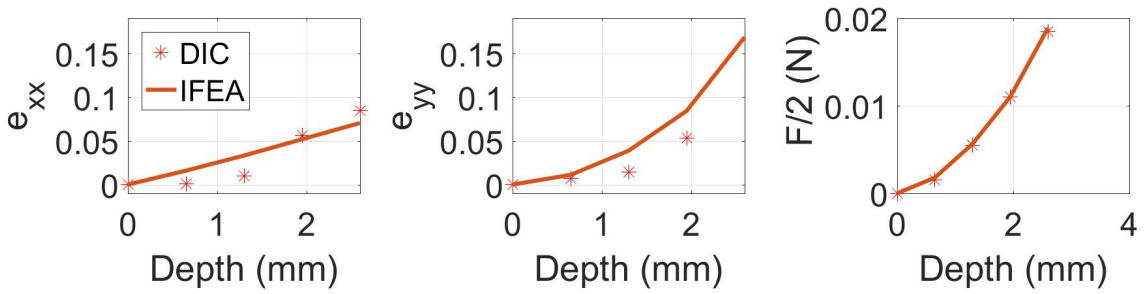

Figure 4.24. IFEA results on the indenter location in the right quadrant of Cervix 1 using MSE

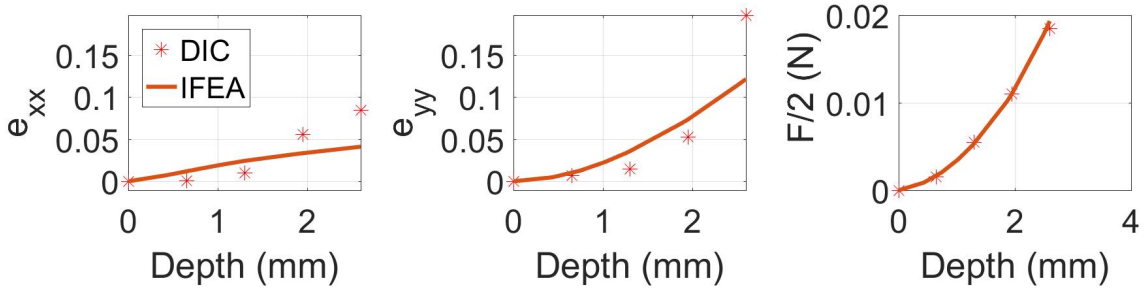

Figure 4.25. IFEA results on the indenter location in the right quadrant of Cervix 1 using MAE

4.4.6 Comparison between the 1-zone model and the 2-zone model

Since the fiber concentration parameter from OCT was not high (b=0.2 or 0.3), we want to study the difference in using the 1-zone model with only circumferential fiber and the 2-zone model with both radial and circumferential fiber. To compare the two models, the same geometry and mesh were used with different fiber orientations. The comparison shows that the 2-zone model has slight different responses when the indentation spot is on the inner zone (Figure 4.26). The 2-zone model showed slightly higher circumferential strain (e_{xx}) and slightly lower radial strain (e_{yy}) when the indentation location is at the inner zone since radial fibers would allow the specimen to deform more in the circumferential direction. When indentation location is at the outer zone, the 1-zone and 2-zone model did not behave differently. This suggests that 1-zone model suffices for preliminary study.

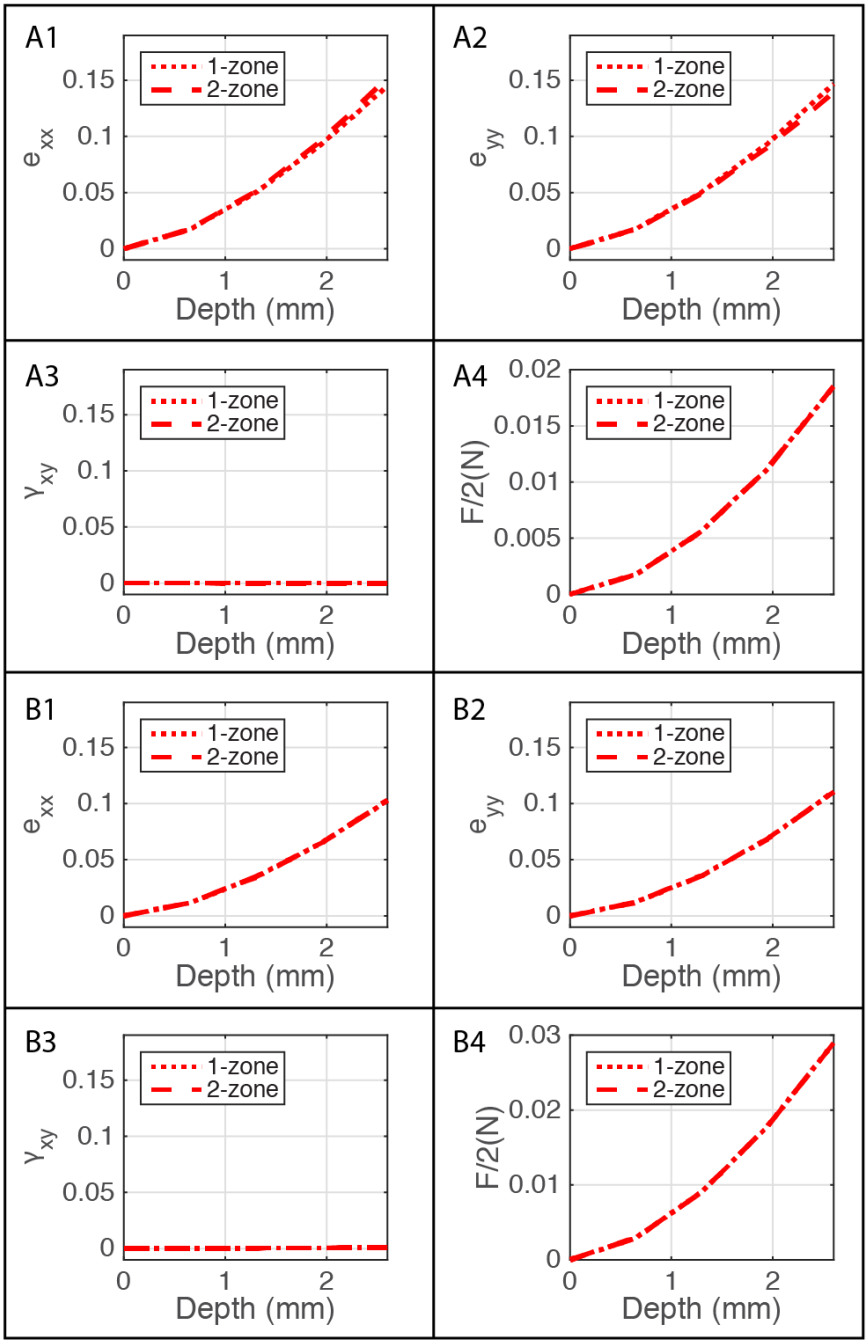

Figure 4.26. Comparison between the 1-zone and the 2-zone model. (A) and (B) shows the mechanical responses of right and posterior quadrant of slice 2 of Cervix 1 using material parameters from IFEA, respectively. For (A), the indentation location was in the inner zone with radial fibers in the 2-zone model and circumferential fibers in the 1-zone model. For (B), the indentation location was in the outer zone with circumferential fibers in both 2-zone and 1-zone models.

4.4.7 Fitting instantaneous strain and force responses

We plan to study the viscoelastic behavior of human cervical tissue in the future so a preliminary study was done to fit the peak strains and forces after each ramp instead of fitting equilibrium values. Our expectation was the tissue should be less compressible at right after the ramp since it has less time to react to the mechanical loading. We compared the strain contour map shapes as well as did the IFEA using peak values. The results show that the fitness of strain curves are comparable between instantaneous and equilibrium response but instantaneous forces were hard to fit using the current material model (Figure 4.27 and Figure 4.28). Strains, as stated earlier, did not change much during the hold phase but the force measurements were very different between equilibrium and instantaneous responses. The force was not fitted well due to high nonlinearity with strain. Material parameters comparison shows higher Young's modulus from instantaneous responses (Table 4.3).

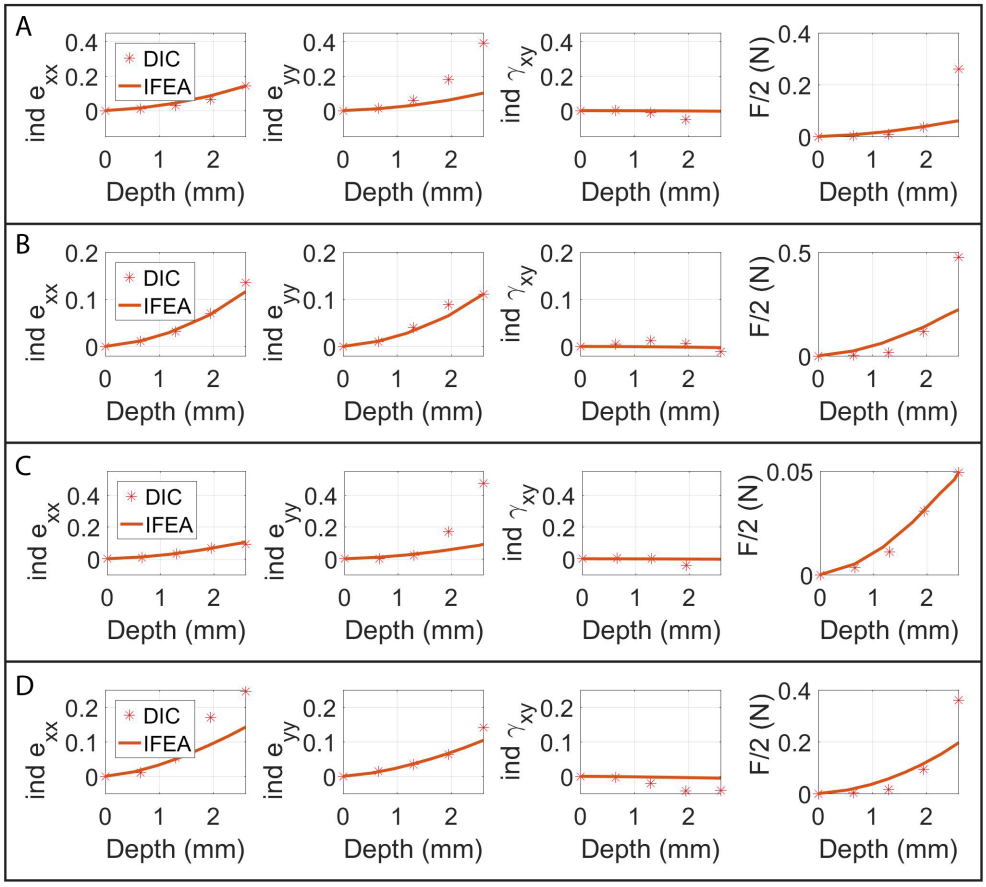

Figure 4.27. IFEA results for instantaneous mechanical responses for the indenter location for four quadrants of slice 2 of Cervix 1. (A) anterior (B) posterior (C) left (D) right.

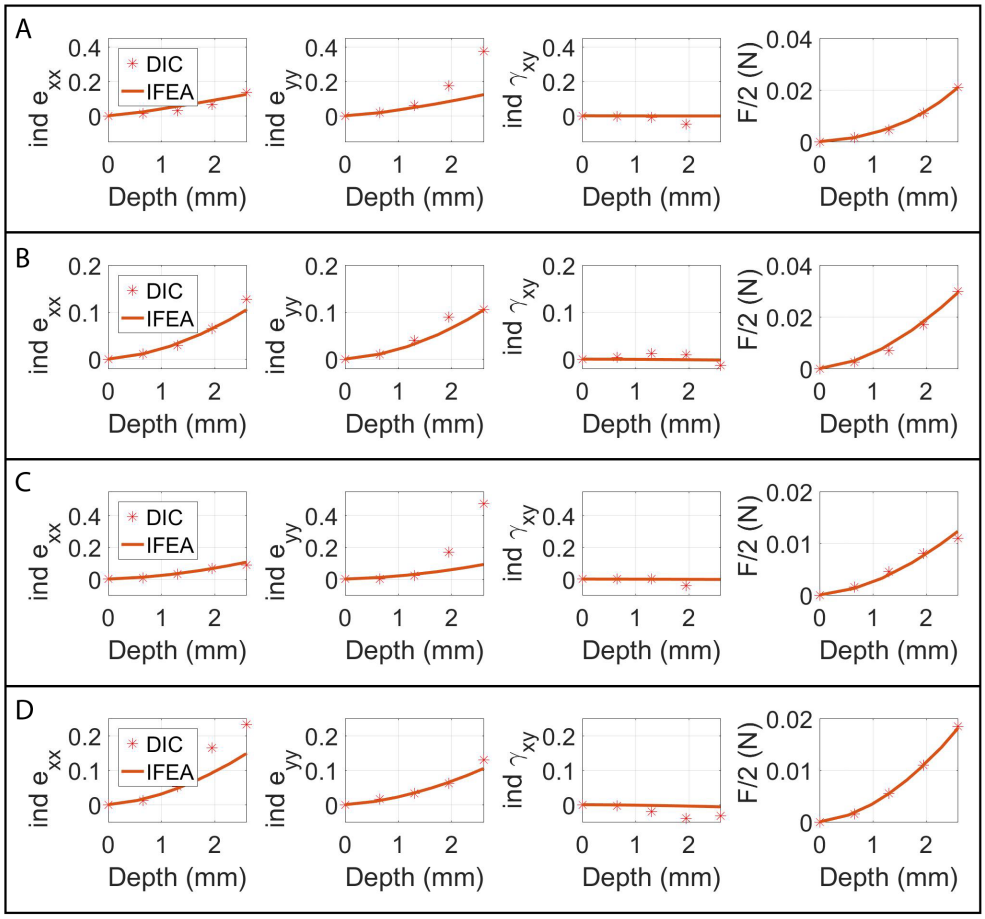

Figure 4.28. IFEA results for equilibrium mechanical responses for the indenter location for four quadrants of slice 2 of Cervix 1. (A) anterior (B) posterior (C) left (D) right.

		E (kPa)	ξ (kPa)	b	v	Error
Instantaneous	A	8.1	1.4	0.3	0.20	2.16
	P	28.3	0.1	0.3	0.11	1.11
	L	6.2	3.7	0.2	0.11	1.79
	R	21.1	57.2	0.2	0.21	1.82
Equilibrium	A	1.4	23.1	0.3	0.42	1.98
	P	3.6	2.9	0.3	0.10	1.08
	L	1.5	1.7	0.2	0.12	1.82
	R	2.1	2.4	0.2	0.16	1.66

Table 4.3. Material parameters from IFEA for the indenter location for four quadrants of slice 2 of Cervix using instantaneous and equilibrium responses.

4.4.8 Incremental digital image correlation

In Vic 2D, there is an option to use incremental correlation. With this option checked, each image is compared with the previous image. Otherwise, when incremental correlation is not in use, each image is always compared with the very first (reference) image. The advantage to use incremental correlation is easier correlation especially at high strain or when pattern breaks down since the different between adjacent two images is relatively small. Correlation results were compared for incremental and non-incremental correlation (Figure 4.29) and the incremental correlation method is obviously superior in our study since it provides much better correlation at higher stain levels. Without incremental correlation, the contour map started to break up starting from the ramp of the third level whereas, with incremental correlation, correlation was successful without many holes in the contour map until the end of the experiment.

However, there are two disadvantages associated with incremental correlation. The first disadvantage is the compounding error. The error is built up as we go from one image to the next. On the contrast, non-incremental correlation only has the one step of error for all images. The second

disadvantage is the non-reversal holes (where no correlation is achieved) since information is carried from one image to the next. In our practice, the second advantage is not a big issue since the location for curve fitting can be changed if the initial selection in the FE model falls into a hole. The compounding error can be an issue for our study so the differences between non-incremental and incremental correlations were compared. To limit compounding error, only 13 even distributed images from the ramp phase and 5 images from the end of each hold phase were used (72 images for four strain levels in total) instead the original over 400 images achieved from experiment. The maximum strains were compared between two correlation methods and the difference is always less than 10%, which is acceptable for our study.

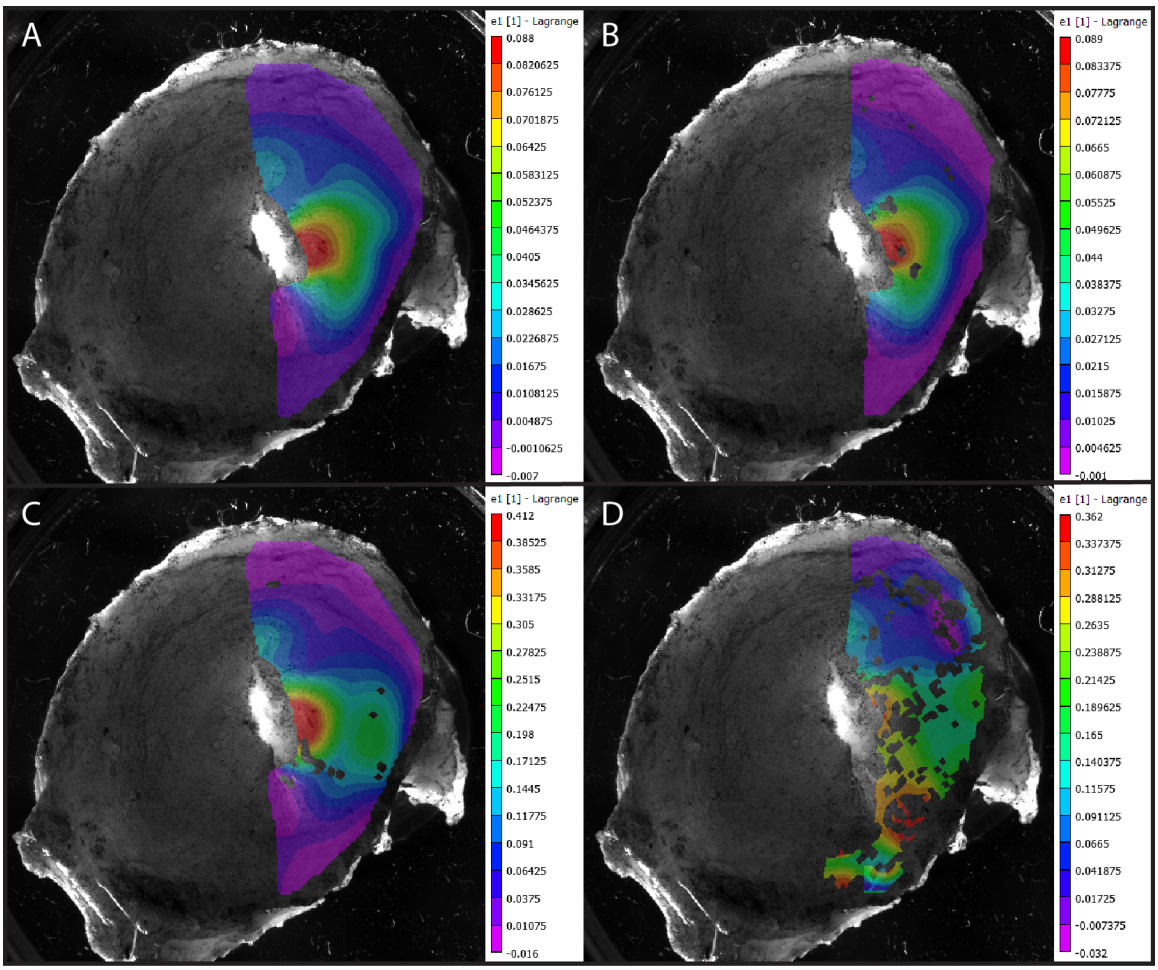

Figure 4.29. The comparison of incremental correlation and non-incremental correlation. The same deck of photos from the right quadrant of slice 2 of Cervix 1 were used for correlation and first principal strain contour map was displayed. (A)(C) show the results from incremental correlation and (B)(D) show the results from non-incremental correlation. (A)(B) are contour maps at the end of the hold phase of the second strain level while (C)(D) are contour maps at the end of the hold phase of the last strain level.

4.4.9 Workflow of experiments and specimen dissection

We proposed the workflow of optical, mechanical, and chemical experiments on the same piece of specimen with most fibers intact. OCT is followed by mechanical indentation test. After that,

the cervical slice is dissected for tensile test, second harmonic generation, and crosslink analysis (Figure 4.30). For mechanical indentation test, four locations were selected in each quadrant. Multiple indentations at different radial locations can be difficult due to the size of the cervical slice. Two tension strips were excised from one cervical slice, normally one strip from the anterior quadrant lying in circumferential direction and one strip from the posterior lying in radial direction. Anterior and posterior quadrants were chosen since they have better preferentially-aligned fibers. Having two strips with different dominant fiber orientations for tensile tests could inform us with the fiber contribution in tension. Second harmonic generation and crosslink analysis specimens were punched in the outer zone of anterior and right quadrants as well as in the inner zone of the left quadrant.

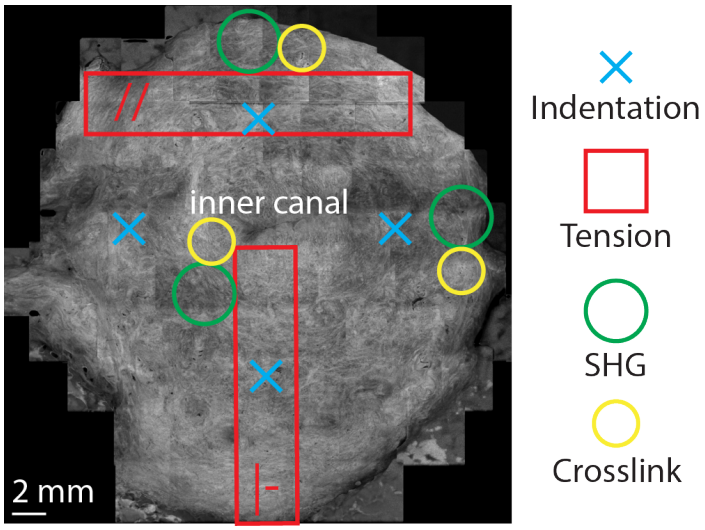

Figure 4.30. Workflow of mechanical, optical, and chemical analysis on one cervical slice.

4.4.10 Sensitivity test

Material parameter sensitivity test was performed using the FE model of the posterior quadrant of slice 2 of Cervix 1. The following material parameters were examined: concentration parameter b (Figure 4.31), Young's modulus E (Figure 4.32), fiber modulus ξ (Figure 4.33), Poisson's ratio v (Figure 4.34), and β (Figure 4.35) in power law fiber. The benchmark values were taken from IFEA results and values on both sides were experimented.

For concentration parameter *b* (Figure 4.31), in addition to 0.3 which was used in IFEA, 0, 1, 3 were used. The results show that *b* has a negligible effect on the force response but it will affect the balance between the axial strains in *x* and *y* directions. As *b* increases, there are more and more fibers in the *x* (circumferential) direction, so the strain in *x* direction decreases while the strain in *y* direction increases. So, *b* is an important factor to balance the axial strain in both circumferential and radial directions to move in the different directions (higher in one direction and lower in the other direction).

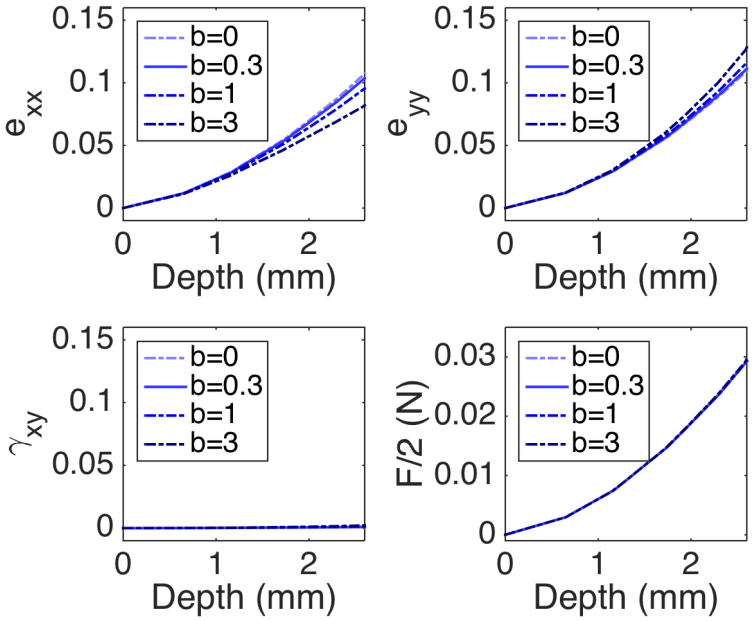

Figure 4.31. The sensitivity test for concentration parameter *b*.

For Young's modulus *E* (Figure 4.32), in addition to 3.5kPa which was the fitting result from IFEA, 0.35kPa and 35kPa were used. Young's modulus seems to have a close-to-linear effect on the force. Forces were about 10 times smaller and larger in the two cases, respectively. A higher Young's modulus will also make strains in both axial directions higher since the contribution of fiber network weakens by a stronger ground substance.

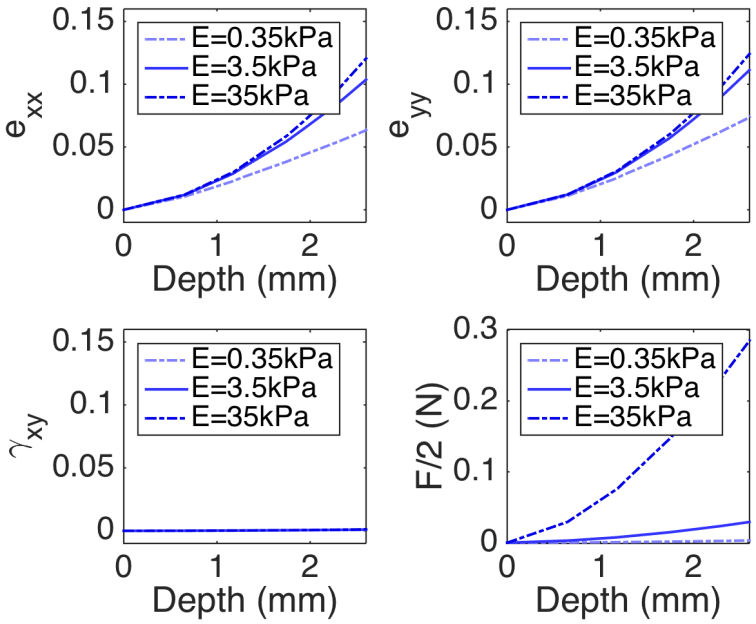

Figure 4.32. The sensitivity test for Young's modulus *E*.

For fiber modulus ξ (Figure 4.33), in addition to 4.9kPa which was the fitting result from IFEA, 0.49kPa, 49kPa, and 490kPa were used. Fiber modulus is seen to have a slight effect on the force response. For strong fiber network, it slightly contributes to the overall strength of the tissue. Fiber modulus had a big effect on the axial strains. Higher fiber modulus greatly reduced the axial strains in both directions by same proportion.

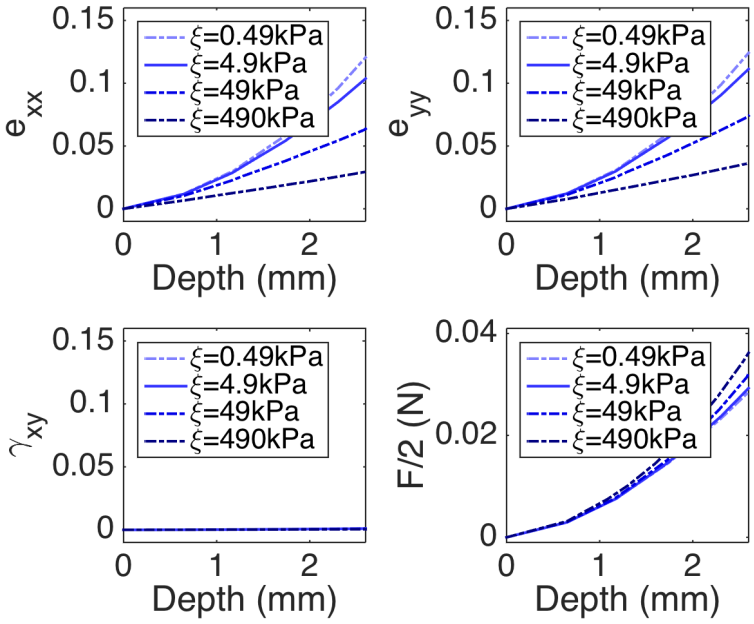

Figure 4.33. The sensitivity test for fiber modulus ξ.

For Poisson's ratio v (Figure 4.34), in addition to 0.11 which was the fitting result from IFEA, 0, 0.3, and 0.45 were used. In the compressible region (v<0.3), the Poisson's ratio does not seem to affect the force response, but when the specimen close to incompressible, the force increases as v increases. This is because, in our experiment, the fixed boundary will greatly affect the deformation of the slice and for nearly incompressible tissue does not have space to go when being squeezed in the center. The Poisson's ratio also has a great effect on the axial strains in both directions. For higher v (less compressible), the axial strain strains were much higher than those of lower v (more compressible). So v is an important factor to adjust the axial strain in both circumferential and radial directions to move in the same direction (higher or lower).

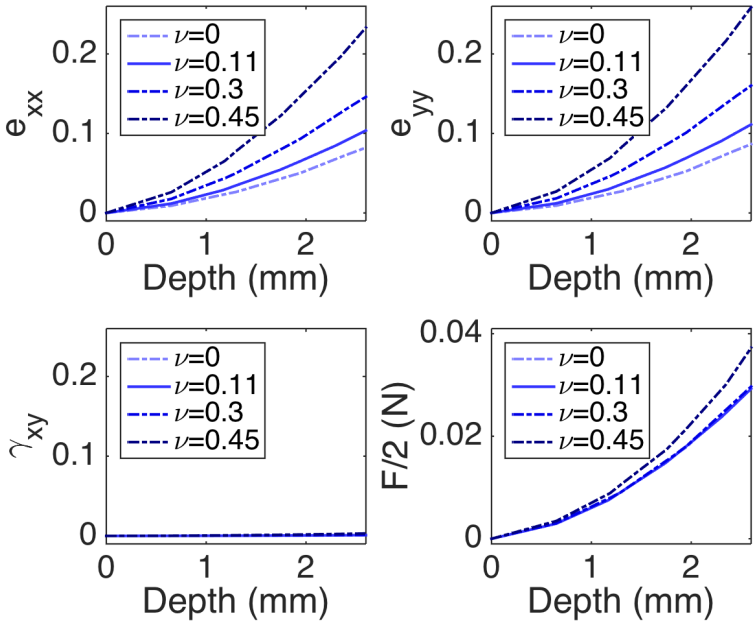

Figure 4.34. The sensitivity test for Poisson's ratio *v*.

For *β* (Figure 4.35), in addition to 3 which was the fitting result from IFEA, 2 and 5 were used. *β* is found to have slight effect on the force response and higher β actually leads to slightly lower force. *β* had a more significant effect on both axial strains. In axial strains tend to be higher with a higher *β*. The effect is more obvious at higher strain but, at low strain levels, the axial strains do not seem to be affected by *β*.

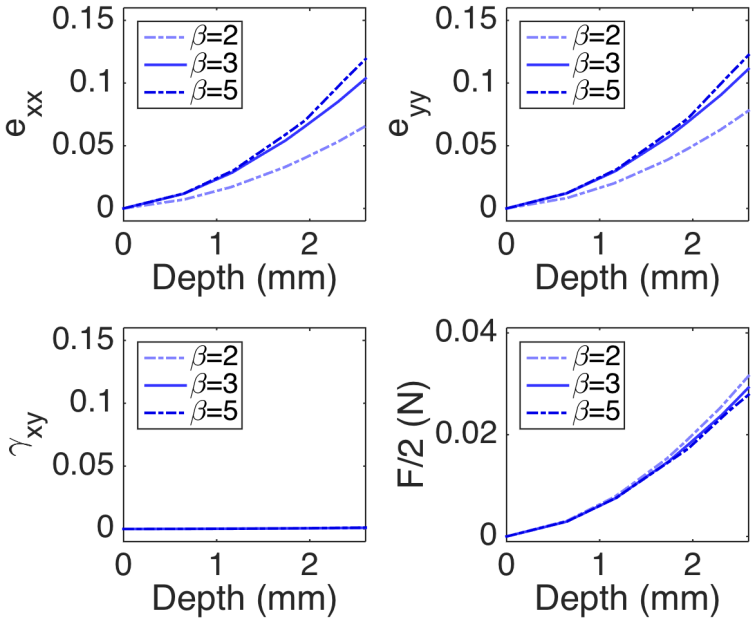

Figure 4.35. The sensitivity test for power term β.

4.5 Conclusions

In this study, eight cervical slices that had been imaged by OCT went through mechanical indentation tests. Camera images of the bottom surface of slice were captured throughout indentation and were used for DIC. Strain and force data were extracted and fitted in custom-built FE models to back up for the material parameters of human cervical tissue. Heterogeneity was found within the cervix for Young's modulus, fiber modulus, and Poisson's ratio in axial and radial directions. Because of the complexity of local fiber texture and boundary conditions, not all indentations bring good DIC and IFEA results. This calls for other mechanical tests to provide information for the tissue including fiber modulus data which can be extracted from tensile test. The currently workflow preserve the slice intact and further mechanical experiments can be performed on the same piece of tissue and at the same location.

5 Preliminary Tensile Test

5.1 Methods

Tensile tests were performed in a customized PBS bath with angled sidewalls to facilitate photography during tensile test (Figure 5.1A,B). Four cervices including three NP cervcies and one PG cervix were used in this preliminary study (Table 5.1). Cervical slices were cut into tension strips with approximate dimension of 2mm x 2mm x 10mm (width x thickness x length). According to the orientation map obtained by OCT, two tension strips were excised from each cervical slices. One tension strip had fibers aligned parallel to the axial direction and the other had fibers aligned perpendicular to the axial direction.

Specimen Number	Age	Pregnancy Status	Gravidity / Parity	Obstetric History	Total Slice Number	Slice Used	OCT Paper Reference
1	41	NP	6/4024	4 ft vd, 1 vtop, 1 sab	7	1	2
2	46	NP	4/1031	vd, vtop x3	10	2	7
3	46	NP	0	n/a	8	2	3
4	42	PG & CI	5/2022	lack information	8	2	13

Table 5.1. Patient demographics of specimens used for this study. CI = cervical insufficiency. Gravidity is equivalent to the total number of pregnancies. Parity data is presented in TPAL recording system. TPAL stands for term, preterm, aborted, and living deliveries, corresponding respectively to each of the 4 digits. vd = vaginal delivery, vtop= voluntary termination, ft = full term c/s = cesarean section, vbac = vaginal birth after cesarean. The last column relates cervices with the specimen number in [79].

The tensile test profile has one load-unload phase to 10% of the length of the strip and six ramp-hold loadings starting with 10% of the length of the strip and an incremental of 5% of the length of the strip for each ramp, all the way to 40% of the length of the strip. Cameras took one photo every half-second during ramp phase and every three minutes during hold phase. The loading/unloading rate was 1%/s and the hold phase lengths vary with strain level. From the first hold phase to the last hold phase, the lengths were 30, 75, 120, 150, 150, and 150 minutes, respectively. Equilibrium responses were used to analysis the relationships among Cauchy stress, axial stretch, and transverse stretch. Force was measured by a universal testing machine (Microtester 5948, Instron Inc., Norwood, MA) and stretch is measured using digital image correlation in Vic-3D (Correlated Solutions, v2009.1.0). Cauchy stress was calculated using the force and actual cross-sectional area.

5.2 Results

Force relaxation was observed at each hold phase (Figure 5.2). For the four cervices tested (Figure 5.3), Cervix 1 and 2 have perpendicular strip with higher Cauchy stress than the parallel strip. For Cervix 3, parallel strip showed higher Cauchy stress than the perpendicular strip did. For Cervix 4, since it was a PG specimen, the responsive Cauchy stress was very small and parallel and perpendicular strips have comparable Cauchy stresses.

As we study the transverse strain λ_2 changes with axial strain λ_1 (Figure 5.4), for Cervix 1 and 2, λ_2 decreases as λ_1 increases, giving positive Poisson's ratio. For Cervix 3 and 4, λ_2 nearly stayed as 1 as λ_1 increases, giving close to zero Poisson's ratio.

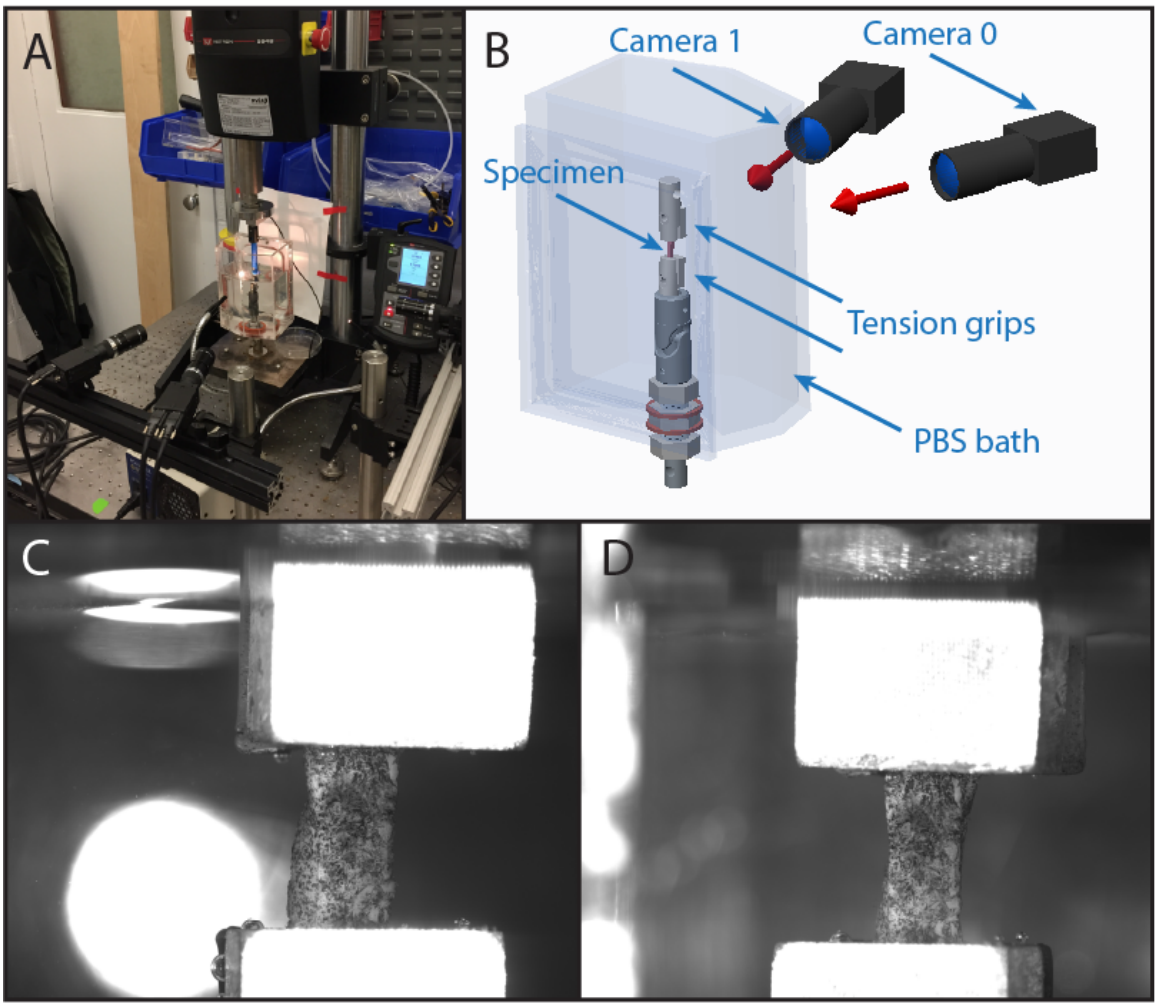

Figure 5.1. Tensile test setup and camera images. (A)(B) Tensile test with two cameras at 60-degree angle capturing specimen deformation during mechanical test. (C)(D) Camera image from camera 0 and camera in (B), respectively.

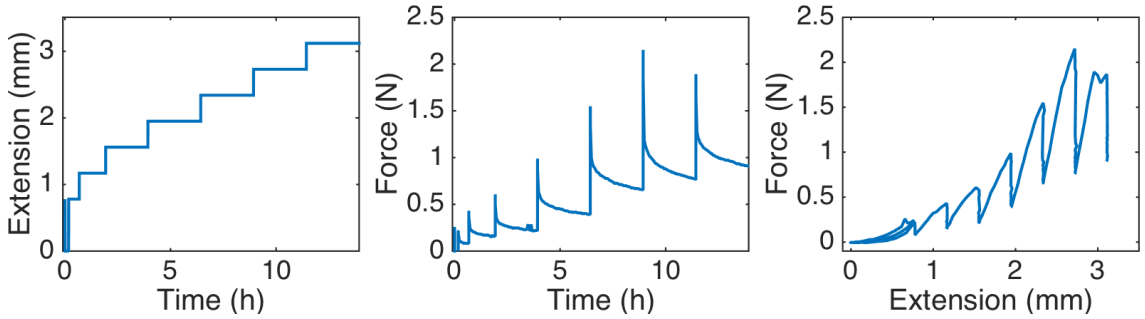

Figure 5.2. Representative tensile loading and responses. (A) Extension loading profile. (B) Force relaxation over time. (C) Force versus extension.

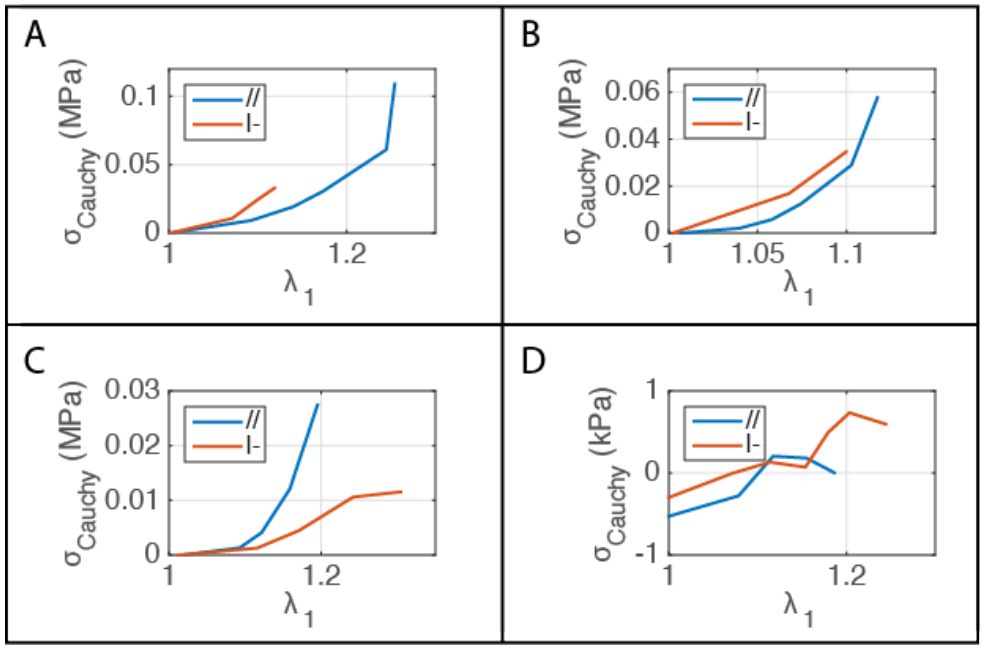

Figure 5.3. Cauchy stress versus stretch for parallel and perpendicular specimens.

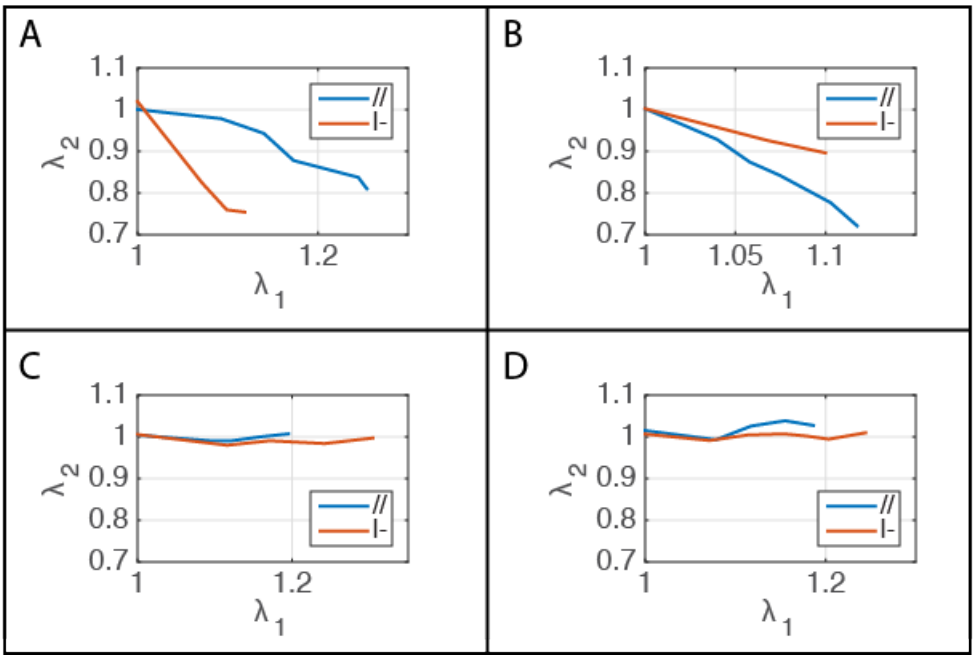

Figure 5.4. Transverse stretch changes with axial stretch for parallel and perpendicular specimens.

5.3 Discussion

We used tensile tests to study the contribution of collagen fiber network in human cervical tissue. Four cervices with two tension strips with different fiber orientations were tested. The significant different of tensile strength was found between NP and PG specimens. The expected outcome of this study was to show that collagen fiber network contribute to the tensile rigidity of human cervical tissue. The expected Cauchy stress for parallel tension strips is much higher than that of perpendicular strips from the same cervix. However, the preliminary results have a wide spread in terms of the Cauchy stress difference between parallel and perpendicular strips. The reason for this could be experimental setup or the local tissue texture. This suggests that we should start with more reliable mechanical tests first.

Bibliography

[1] M. Bauer *et al.*, "In Vivo Characterization of the Mechanics of Human Uterine Cervices," *Annals of the New York Academy of Sciences,* vol. 1101, no. 1, pp. 186-202, 2007.

[2] B. Timmons, M. Akins, and M. Mahendroo, "Cervical remodeling during pregnancy and parturition," *Trends in Endocrinology & Metabolism,* vol. 21, no. 6, pp. 353-361, 6// 2010.

[3] S. Badir, M. Bajka, and E. Mazza, "A novel procedure for the mechanical characterization of the uterine cervix during pregnancy," *Journal of the Mechanical Behavior of Biomedical Materials,* vol. 27, pp. 143-153, 11// 2013.

[4] K. M. Myers *et al.*, "A continuous fiber distribution material model for human cervical tissue," *Journal of Biomechanics,* vol. 48, no. 9, pp. 1533-1540, 2015.

[5] E. H. Bishop, "Pelvic scoring for elective induction," *Obstetrics & Gynecology,* vol. 24, no. 2, pp. 266-268, 1964.

[6] R. Newman *et al.*, "Preterm prediction study: comparison of the cervical score and Bishop score for prediction of spontaneous preterm delivery," *Obstetrics and gynecology,* vol. 112, no. 3, p. 508, 2008.

[7] H. Blencowe *et al.*, "National, regional, and worldwide estimates of preterm birth rates in the year 2010 with time trends since 1990 for selected countries: a systematic analysis and implications," *The Lancet,* vol. 379, no. 9832, pp. 2162-2172, 2012.

[8] P. Dimes Mo, "Children St, WHO," *Born too soon: the global action report on preterm birth. Geneva: World Health Organization,* pp. 1-124, 2012.

[9] F. C. Barros *et al.*, "The distribution of clinical phenotypes of preterm birth syndrome: implications for prevention," *JAMA pediatrics,* vol. 169, no. 3, pp. 220-229, 2015.

[10] M. House, H. Feltovich, T. J. Hall, T. Stack, A. Patel, and S. Socrate, "Three-dimensional, extended field-of-view ultrasound method for estimating large strain mechanical properties of the cervix during pregnancy," *Ultrasonic imaging,* vol. 34, no. 1, pp. 1-14, 2012.

[11] K. M. Myers, A. Paskaleva, M. House, and S. Socrate, "Mechanical and biochemical properties of human cervical tissue," *Acta Biomaterialia,* vol. 4, no. 1, pp. 104-116, 2008.

[12] K. M. Myers *et al.*, "The mechanical role of the cervix in pregnancy," *Journal of Biomechanics,* vol. 48, no. 9, pp. 1511-1523, 2015.

[13] N. M. Zork *et al.*, "A systematic evaluation of collagen cross-links in the human cervix," *American Journal of Obstetrics and Gynecology,* vol. 212, no. 3, pp. 321.e1-321.e8, 3// 2015.

[14] M. House, D. L. Kaplan, and S. Socrate, "Relationships Between Mechanical Properties and Extracellular Matrix Constituents of the Cervical Stroma During Pregnancy," *Seminars in Perinatology,* vol. 33, no. 5, pp. 300-307, 2009.

[15] K. Myers, S. Socrate, D. Tzeranis, and M. House, "Changes in the biochemical constituents and morphologic appearance of the human cervical stroma during pregnancy," *European Journal of Obstetrics & Gynecology and Reproductive Biology,* vol. 144, pp. S82-S89, 2009.

[16] M. Kirby, R. Aspden, and D. Hukins, "Determination of the orientation distribution function for collagen fibrils in a connective tissue site from a high-angle X-ray diffraction pattern," *Journal of Applied Crystallography,* vol. 21, no. 6, pp. 929-934, 1988.

[17] R. M. Aspden, "Collagen Organisation in the Cervix and its Relation to Mechanical Function,"

Collagen and Related Research, vol. 8, no. 2, pp. 103-112, 3// 1988.

[18] S. Weiss *et al.*, "Three-dimensional fiber architecture of the nonpregnant human uterus determined ex vivo using magnetic resonance diffusion tensor imaging," *The Anatomical Record Part A: Discoveries in Molecular, Cellular, and Evolutionary Biology,* vol. 288A, no. 1, pp. 84-90, 2006.

[19] H. Feltovich, T. Hall, and V. Berghella, "Beyond cervical length: emerging technologies for assessing the pregnant cervix.," *Am J Obstet Gynecol,* pp. 1-43, May 2012.

[20] Y. Zhang *et al.*, "A compact fiber-optic SHG scanning endomicroscope and its application to visualize cervical remodeling during pregnancy," *Proceedings of the National Academy of Sciences,* vol. 109, no. 32, pp. 12878-12883, August 7, 2012 2012.

[21] Y. Gan, W. Yao, K. M. Myers, and C. P. Hendon, "An automated 3D registration method for optical coherence tomography volumes," in *Engineering in Medicine and Biology Society (EMBC), 2014 36th Annual International Conference of the IEEE*, 2014, pp. 3873-3876.

[22] Y. Gan, W. Yao, K. M. Myers, J. Y. Vink, R. J. Wapner, and C. P. Hendon, "Analyzing three-dimensional ultrastructure of human cervical tissue using optical coherence tomography," *Biomedical Optics Express,* vol. 6, no. 4, pp. 1090-1108, 2015/04/01 2015.

[23] H. Feltovich and T. J. Hall, "Quantitative imaging of the cervix: setting the bar," *Ultrasound in Obstetrics & Gynecology,* vol. 41, no. 2, pp. 121-128, 2013.

[24] D. Danforth, A. Veis, M. Breen, H. Weinstein, J. C. Buckingham, and P. Manalo, "The effect of pregnancy and labor on the human cervix: changes in collagen, glycoproteins, and glycosaminoglycans," *American journal of obstetrics and gynecology,* vol. 120, no. 5, pp. 641-651, 1974.

[25] S. Y. Yu, C. A. Tozzi, J. Babiarz, and P. C. Leppert, "Collagen changes in rat cervix in pregnancy—polarized light microscopic and electron microscopic studies," *Experimental Biology and Medicine,* vol. 209, no. 4, pp. 360-368, 1995.

[26] W. Bryant, J. Greenwell, and P. Weeks, "Alterations in collagen organization during dilatation of the cervix uteri," *Surgery, gynecology & obstetrics,* vol. 126, no. 1, pp. 27-39, 1968.

[27] K. Myers, S. Socrate, A. Paskaleva, and M. House, "A study of the anisotropy and tension/compression behavior of human cervical tissue.," *J Biomech Eng,* vol. 132, no. 2, p. 021003, February 2010.

[28] K. M. Myers, A. P. Paskaleva, M. House, and S. Socrate, "Mechanical and biochemical properties of human cervical tissue," *Acta Biomaterialia,* vol. 4, no. 1, pp. 104-116, 1// 2008.

[29] W. Yao *et al.*, "Measuring the compressive viscoelastic mechanical properties of human cervical tissue using indentation," *Journal of the Mechanical Behavior of Biomedical Materials,* vol. 34, no. 0, pp. 18-26, 6// 2014.

[30] M. Fernandez, J. Vink, K. Yoshida, R. Wapner, and K. M. Myers, "Direct measurement of the permeability of human cervical tissue," (in eng), *Journal of biomechanical engineering,* vol. 135, no. 2, p. 021024, 2013/02// 2013.

[31] E. Mazza, A. Nava, M. Bauer, R. Winter, M. Bajka, and G. A. Holzapfel, "Mechanical properties of the human uterine cervix: an in vivo study," *Medical image analysis,* vol. 10, no. 2, pp. 125-136, April 2006.

[32] D. Liao, L. Hee, P. Sandager, N. Uldbjerg, and H. Gregersen, "Identification of biomechanical properties in vivo in human uterine cervix," *Journal of the mechanical behavior of biomedical materials,* vol. 39, pp. 27-37, 2014.

[33] L. Hee, D. Liao, P. Sandager, H. Gregersen, and N. Uldbjerg, "Cervical stiffness evaluated in vivo by endoflip in pregnant women," *PloS one,* vol. 9, no. 3, p. e91121, 2014.

[34] D. Huang *et al.*, "Optical coherence tomography," *Science (New York, NY),* vol. 254, no. 5035, p. 1178, 1991.

[35] A. M. Zysk, F. T. Nguyen, A. L. Oldenburg, D. L. Marks, and S. A. Boppart, "Optical coherence tomography: a review of clinical development from bench to bedside," *Journal of biomedical optics,* vol. 12, no. 5, pp. 051403-051403-21, 2007.

[36] J. Fujimoto and W. Drexler, "Introduction to optical coherence tomography," in *Optical coherence tomography*: Springer, 2008, pp. 1-45.

[37] T. K. A. B. Eskes, "The extracellular matrix of the uterus, cervix and fetal membranes: synthesis, degradation and hormonal regulation," *European Journal of Obstetrics and Gynecology and Reproductive Biology,* vol. 45, no. 1, p. 77.

[38] I. A. Buhimschi, L. Dussably, C. S. Buhimschi, A. Ahmed, and C. P. Weiner, "Physical and biomechanical characteristics of rat cervical ripening are not consistent with increased collagenase activity," *American journal of obstetrics and gynecology,* vol. 191, no. 5, pp. 1695-1704, 2004.

[39] B. S. Oxlund, G. Ørtoft, A. Brüel, C. C. Danielsen, H. Oxlund, and N. Uldbjerg, "Cervical collagen and biomechanical strength in non-pregnant women with a history of cervical insufficiency," *Reproductive Biology and Endocrinology,* vol. 8, no. 1, p. 92, 2010.

[40] M. L. Akins, K. Luby-Phelps, R. A. Bank, and M. Mahendroo, "Cervical softening during pregnancy: regulated changes in collagen cross-linking and composition of matricellular proteins in the mouse," *Biology of reproduction,* vol. 84, no. 5, pp. 1053-1062, 2011.

[41] M. House, D. L. Kaplan, and S. Socrate, "Relationships between mechanical properties and extracellular matrix constituents of the cervical stroma during pregnancy," in *Seminars in perinatology*, 2009, vol. 33, no. 5, pp. 300-307: Elsevier.

[42] M. House and S. Socrate, "The cervix as a biomechanical structure," *Ultrasound in obstetrics & gynecology,* vol. 28, no. 6, pp. 745-749, 2006.

[43] M. Oyen, "Analytical techniques for indentation of viscoelastic materials," *Philosophical Magazine,* vol. 86, no. 33-35, pp. 5625-5641, 2006.

[44] J. M. Mattice, A. G. Lau, M. L. Oyen, and R. W. Kent, "Spherical indentation load-relaxation of soft biological tissues," *Journal of Materials Research,* vol. 21, no. 08, pp. 2003-2010, 2006.

[45] Y.-P. Zheng, Y. Choi, K. Wong, S. Chan, and A. F. Mak, "Biomechanical assessment of plantar foot tissue in diabetic patients using an ultrasound indentation system," *Ultrasound in medicine & biology,* vol. 26, no. 3, pp. 451-456, 2000.

[46] K.-Y. Liang and S. L. Zeger, "Longitudinal data analysis using generalized linear models," *Biometrika,* pp. 13-22, 1986.

[47] R. L. Prentice and L. P. Zhao, "Estimating equations for parameters in means and covariances of multivariate discrete and continuous responses," *Biometrics,* pp. 825-839, 1991.

[48] M. L. Oyen, T. A. Shean, D. G. Strange, and M. Galli, "Size effects in indentation of hydrated biological tissues," *Journal of Materials Research,* vol. 27, no. 01, pp. 245-255, 2012.

[49] K. M. Myers, S. Socrate, A. Paskaleva, and M. House, "A study of the anisotropy and tension/compression behavior of human cervical tissue," *Journal of biomechanical engineering,* vol. 132, no. 2, p. 021003, 2010.

[50] F. Naftolin, *Dilatation of the uterine cervix: connective tissue biology and clinical management*. Raven Press (ID), 1980.

[51] G. Pharr, W. Oliver, and F. Brotzen, "On the generality of the relationship among contact stiffness, contact area, and elastic modulus during indentation," *Journal of materials research,* vol. 7, no. 03, pp. 613-617, 1992.

[52] M. Galli, K. S. Comley, T. A. Shean, and M. L. Oyen, "Viscoelastic and poroelastic mechanical characterization of hydrated gels," *Journal of Materials Research,* vol. 24, no. 03, pp. 973-979, 2009.

[53] M. L. Oyen, R. F. Cook, J. A. Emerson, and N. R. Moody, "Indentation responses of time-dependent films on stiff substrates," *Journal of materials research,* vol. 19, no. 08, pp. 2487-2497, 2004.

[54] R. Namani *et al.*, "Elastic characterization of transversely isotropic soft materials by dynamic shear and asymmetric indentation," *Journal of biomechanical engineering,* vol. 134, no. 6, p. 061004, 2012.

[55] M. Mahendroo, "Cervical remodeling in term and preterm birth: insights from an animal model," *Reproduction,* vol. 143, no. 4, pp. 429-438, April 1, 2012 2012.

[56] Y. Akgul, R. Holt, M. Mummert, A. Word, and M. Mahendroo, "Dynamic changes in cervical glycosaminoglycan composition during normal pregnancy and preterm birth," *Endocrinology,* vol. 153, no. 7, pp. 3493-3503, 2012.

[57] Y. Akgul and M. Mahendroo, "Cervical changes accompanying birth," *The Guide to Investigation of Mouse Pregnancy,* p. 391, 2013.

[58] Y. Akgul and M. Mahendroo, "Assessment of Changes in the Peripartum Cervix-64," 2014.

[59] W. Drexler and J. G. Fujimoto, *Optical Coherence Tomography: Technology and Applications*. Springer Berlin Heidelberg, 2008.

[60] A. F. Fercher, W. Drexler, C. K. Hitzenberger, and T. Lasser, "Optical coherence tomography - principles and applications," *Reports on Progress in Physics,* vol. 66, no. 2, p. 239, 2003.

[61] Z. Yaqoob, J. Wu, E. J. McDowell, X. Heng, and C. Yang, "Methods and application areas of endoscopic optical coherence tomography," *Journal of Biomedical Optics,* vol. 11, no. 6, pp. 063001-063001-19, 2006.

[62] W. Kang, X. Qi, N. J. Tresser, M. Kareta, J. L. Belinson, and A. M. Rollins, "Diagnostic efficacy of computer extracted image features in optical coherence tomography of the precancerous cervix," *Medical Physics,* vol. 38, no. 1, pp. 107-113, 2011.

[63] I. Orfanoudaki, D. Kappou, and S. Sifakis, "Recent advances in optical imaging for cervical cancer detection," (in English), *Archives of Gynecology and Obstetrics,* vol. 284, no. 5, pp. 1197-1208, 2011/11/01 2011.

[64] S.-W. Lee *et al.*, "Optical diagnosis of cervical intraepithelialneoplasm (CIN) using polarization-sensitiveoptical coherence tomography," *Optics Express,* vol. 16, no. 4, pp. 2709-2719, 2008/02/18 2008.

[65] C. P. Fleming, C. M. Ripplinger, B. Webb, I. R. Efimov, and A. M. Rollins, "Quantification of cardiac fiber orientation using optical coherence tomography," *J Biomed Opt,* vol. 13, no. 3, p. 030505, May-Jun 2008.

[66] Y. Gan and C. P. Fleming, "Extracting three-dimensional orientation and tractography of myofibers using optical coherence tomography," *Biomedical Optics Express,* vol. 4, no. 10, pp. 2150-2165, 2013/10/01 2013.

[67] K. P. Quinn and I. Georgakoudi, "Rapid quantification of pixel-wise fiber orientation data in micrographs," *Journal of Biomedical Optics,* vol. 18, no. 4, pp. 046003-046003, 2013.

[68] Z. Liu *et al.*, "Rapid three-dimensional quantification of voxel-wise collagen fiber orientation," *Biomedical Optics Express,* vol. 6, no. 7, pp. 2294-2310, 2015/07/01 2015.

[69] T. C. Gasser, R. W. Ogden, and G. A. Holzapfel, "Hyperelastic modelling of arterial layers with distributed collagen fibre orientations," *Journal of The Royal Society Interface,* vol. 3, no. 6, pp. 15-35, 2006-02-22 00:00:00 2006.

[70] W. J. Karlon, J. W. Covell, A. D. McCulloch, J. J. Hunter, and J. H. Omens, "Automated measurement of myofiber disarray in transgenic mice with ventricular expression of ras," *The Anatomical Record,* vol. 252, no. 4, pp. 612-625, 1998.

[71] M. Fernandez *et al.*, "Investigating the mechanical function of the cervix during pregnancy using finite element models derived from high-resolution 3D MRI," *Computer Methods in Biomechanics and Biomedical Engineering,* vol. 19, no. 4, pp. 404-417, 2016/03/11 2016.

[72] M. House, R. A. Bhadelia, K. Myers, and S. Socrate, "Magnetic resonance imaging of three-dimensional cervical anatomy in the second and third trimester," *European Journal of Obstetrics & Gynecology and Reproductive Biology,* vol. 144, pp. S65-S69, 2009.

[73] R. M. Williams, W. R. Zipfel, and W. W. Webb, "Interpreting Second-Harmonic Generation Images of Collagen I Fibrils," *Biophysical Journal,* vol. 88, no. 2, pp. 1377-1386, 2// 2005.

[74] M. S. Sacks, D. B. Smith, and E. D. Hiester, "A small angle light scattering device for planar connective tissue microstructural analysis," *Annals of biomedical engineering,* vol. 25, no. 4, pp. 678-689, 1997.

[75] M. S. Sacks, D. B. Smith, and E. D. Hiester, "The aortic valve microstructure: effects of transvalvular pressure," *Journal of biomedical materials research,* vol. 41, no. 1, pp. 131-141, 1998.

[76] M. S. Sacks, "Incorporation of Experimentally-Derived Fiber Orientation into a Structural Constitutive Model for Planar Collagenous Tissues," *Journal of Biomechanical Engineering,* vol. 125, no. 2, pp. 280-287, 2003.

[77] M. Wolman, "Polarized light microscopy as a tool of diagnostic pathology," *Journal of Histochemistry & Cytochemistry,* vol. 23, no. 1, pp. 21-50, January 1, 1975 1975.

[78] J. Vink and H. Feltovich, "Cervical etiology of spontaneous preterm birth," *Seminars in Fetal and Neonatal Medicine,* vol. 21, no. 2, pp. 106-112, 4// 2016.

[79] W. Yao, Y. Gan, K. M. Myers, J. Y. Vink, R. J. Wapner, and C. P. Hendon, "Collagen Fiber Orientation and Dispersion in the Upper Cervix of Non-Pregnant and Pregnant Women," *PLoS One,* vol. 11, no. 11, p. e0166709, 2016.